Low Frequency Field Prediction Applied to CISPR 25 Test Setups

A Thesis Submitted to the Faculty of Electrical Engineering and Information Technology of TU Dortmund University in Partial Fulfillment of the Requirements for the Degree of Doctor of Engineering Sciences (Dr.-Ing.)

by

M. Sc. Zongyi Chen

Dortmund, 2020

Date of Oral Examination:	24.06.2019
Supervisor:	Prof. Dr.-Ing. Stephan Frei

Acknowledgments

I would like to take the opportunity to thank all people who helped and supported me during my Ph.D. studies from 2012 to 2017 in Dortmund.

First of all, I would like to thank my doctoral advisor Prof. Dr.-Ing. Stephan Frei. He gave me the greatest opportunities to improve my personal and technical capabilities during the time in Arbeitsgebiet Bordsysteme, TU Dortmund. I sincerely thank him for providing a motivating, encouraging, and enthusiastic environment during my pursuit of doctoral research. It was his steady support and inspiring guidance, which lead me to write this dissertation. I will always reflect on the numerous discussions with our colleagues we had in his office. During the time of work in his group, I received all kinds of supports from him. I am grateful to have had the opportunity to work under his guidance.

Secondly, I would like to express my sincere thanks to Dr.-Ing. Heinz-Dietrich Brüns and his group, Institut für Theoretische Elektrotechnik, TUHH. The software CONCEPT-II from his group supports the kernel of my work. Dr. Brüns gave me full support on the implementation of the Huygens principle and the field integral based on the method of moments. I can still remember the time when I visited him in Hamburg. His rich experience proved invaluable suggestions in clarifying many details of the software CONCEPT-II, the Huygens principle, and the field integral method.

Thirdly, I thank Prof. Dr.-Ing David Pommerenke for giving me the opportunity to do the part of my research in EMC-laboratory, Missouri University S&T, USA, and also for his full support on finishing the dissertation. I thank him for all the suggestions, comments, and support.

Additionally, I would like to thank all the colleagues of the Arbeitsgebiet Bordsysteme group for those nice days we had with each other and for the extraordinarily friendly and fruitful working atmosphere at the institute, which allowed for intense experience exchange. I want to acknowledge the great efforts of Alexander Zeichner. A significant part of my work couldn’t have been done without his voluntary support.

I would like to thank all members of the examination committee.

When I write this acknowledgment, the list of those I want to acknowledge keeps increasing. For all those who helped me, although their names may not be listed explicitly, my heart goes to you in gratitude.

Dortmund, Germany, 2020 Zongyi Chen

Abstract

Modern automotive systems integrate a variety of electrical and electronic components. To estimate the radiated emissions, the standard CISPR 25 describes the absorber-lined shielded enclosure (ALSE) method, which is the most important standardized field measurement method. However, it suffers from the need for a large anechoic chamber. To reduce costs and more conveniently integrate radiated emission investigations into the product design cycle, alternative methods that predict emissions without such a chamber are necessary. These methods measure currents, voltages, or fields close to the setup's vicinity, and with the help of appropriate models, CISPR 25 quantities can be calculated. However, the known methods often fail at frequencies below 30 MHz. This dissertation introduces two new methods based on electric near-field measurements to overcome the problems. The first method uses extrapolation and interpolation of the measured data to create a Huygens' surface. The field at 1 m distance can be calculated from the Huygens' surface. The second method finds electrostatic dipoles from the measured data. The fields from the dipoles can be estimated at 1 m distance. This dissertation uses measurements and full-wave simulation to verify the accuracy of the proposed methods.

Table of Content

Nomenclature and Abbreviations

$\vec{E}$	electric field intensity
$\vec{H}$	magnetic field intensity
$\vec{J}$	electric current density
$\vec{M}$	magnetic current density
ρ	electric charge density
ρ_{m}	fictitious magnetic charge density
ρ_{l}	line charge density
ε	permittivity of the medium, in vacuum $\varepsilon = \varepsilon_0 = 8.85 \times 10^{-12}\ \mathrm{F/m}$
μ	permeability of the medium, in vacuum $\mu = \mu_0 = 4\pi \times 10^{-7}\ \mathrm{H/m}$
$\vec{n}$	normal vector (surface)
$\vec{\mathrm{A}}$	magnetic vector potential
$\vec{\mathrm{F}}$	electric vector potential
k	wave number, in vacuum $k = k_0 = \omega\sqrt{\mu_0\varepsilon_0}$
η_0	intrinsic impedance of vacuum, $\eta_0 = \sqrt{\mu_0/\varepsilon_0} \approx 377\ \Omega$
Φ	electric scalar potential
f_n	basis function
I_{J}	electric current
I_{M}	magnetic current
I_{CM}	common-mode current
r_ω	wire radius
δ	Dirac delta function
Z_A	antenna input impedance
Z_S	source impedance
Z_L	load impedance
R_{loss}	loss resistance of antenna
R_{rad}	radiation resistance of antenna
C_A	antenna self-capacitance

L_A	antenna self-inductance
C_C	mutual capacitance
M	mutual inductance
A_{eff}	effective antenna area
h_{eff}	effective height of antenna
λ	wavelength
C'	per-unit-length capacitance
L'	per-unit-length inductance
R'	per-unit-length resistance
G'	per-unit-length conductance
C_0	speed of light in vacuum
β	phase constant
Z_C	characteristic impedance
Γ_S	source reflection coefficient
Γ_L	load reflection coefficient

AF	Antenna Factor
ALSE	Absorber-Lined Shielded Enclosure
AN	Artificial Network
CSWR	Current Standing Wave Ratio
EFIE	Electric Field Integral Equation
EMC	Electromagnetic Compatibility
EUT	Equipment Under Test
FEM	Finite Element Method
FFT	Fast Fourier Transformation
MDM	Multi-Dipole Model
MoM	Method of Moment
MTL	Multiconductor Transmission Line
OATS	Open-Area Test Site
PCB	Printed Circuit Board

PEC	Perfect Electric Conductor
PMC	Perfect Magnetic Conductor
PO	Physics Optical
TWP	Twisted Wire
VNA	Vector Network Analyzer

1 Introduction

1.1 Emission of Automotive Components

Modern automotive electronic components provide much functionality with high clock and data rates, which also leads to new challenges to meet all **e**lectro**m**agnetic **c**ompatibility (EMC) demands [1]. Different levels of problems can occur due to EMC issues, from losses in infotainment data transmission to severe failures of control systems or even physical damage.

An EMC compliant electric/electronic system is supposed to meet the following criteria: the system is immune to disturbance from other systems, and its interferences/emissions do not disturb the functionalities of nearby devices [2]. This criterion requires that the electric/electronic[1] systems shall be EMC compliant with regard the electromagnetic emissions[2] they produce and their exposure to electromagnetic fields, currents, and voltages. This work mainly focuses on field emissions caused by a system.

A typical automotive system consists of electric/electronic components with an attached cable bundle. In [2], it is pointed out that the cable bundle often acts as a much more efficient radiator than the connected components, as the length of the cable bundle is much longer than the sizes of the electronic components. On-board antennas are important victims for the emissions from such structures. For example, at lower frequencies, the emission may disturb the analog or digital broadcasting services in the frequency range of 150 kHz - 2 MHz (LW/AM)[3] or up to 7.3 MHz (SW in Germany in the past). Figure 1.1 shows the initial EMC problem. Disturbing voltages from electronic systems can couple to rod antenna (dark blue). A coaxial cable connects the rod antenna to a high impedance antenna amplifier input of a radio (grey)[4]. Due to the rod

---

[1] In the following electronic systems are mostly talked about, as in most cases electronic components are involved.

[2] The “emissions” include conducted (voltages and currents) and field emissions, here only referred as field emissions.

[3] Many countries have switched off their AM broadcasting services but in some countries the AM frequency band is extensively used for analog or digital radio. I.e., the global acting car manufacturers have to take care for good radio reception also at low frequencies which is a very challenging task, due to extensive use of power electronics with functional frequencies in the range of 100 kHz and first harmonics in the AM frequency range.

[4] As for low frequencies, electrical short antennas have to be used. Rod structures or loop structures are possible. Loops are difficult to integrate in the shielding car body. Rods can be placed easily on the car body and were commonly used in the past. Today, antennas are often integrated in the windows, the basic principle remains the same.

structure and the high impedance of the antenna amplifier, capacitive coupling is dominant. Inductive coupling is weak[5].

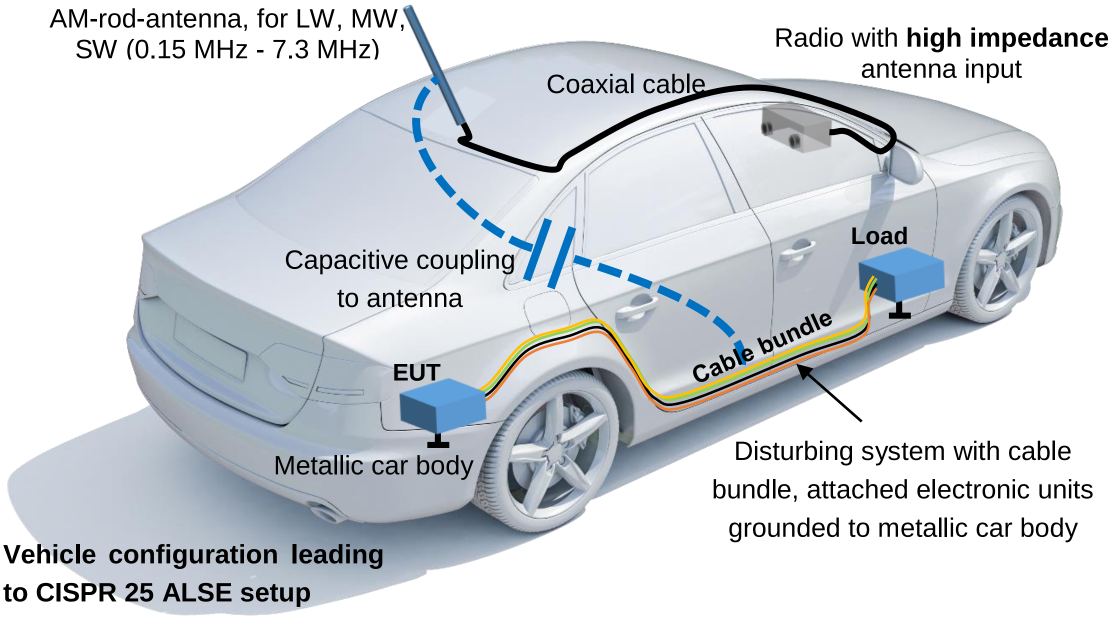

Figure 1.1: Initial problem of capacitive coupling to a short AM antenna.

Generally, to determine the emissions of automotive systems, international standards, for example, CISPR 12 [3] and CISPR 25 [4] are commonly used. These standards usually specify a particular measurement method and propose limits for emissions. For example, the CISPR 25 standard [4] defines the limits for conducted and radiated emissions of automotive systems arising in a specific setup. The goal of the limits is to allow the system integrators such as car manufacturers to combine several systems in an automobile so that emission problems are unlikely to occur.

1.2 Field Measurements According to CISPR 25

The standardized methods for automotive components are commonly used to characterize the field emissions. Radiated or near-field interferences are measured with defined setups. Field emission measurements require the use of either an **o**pen-**a**rea **t**est **s**ite (OATS) or an **a**bsorber-**l**ined **s**hielded **e**nclosure (ALSE), also often called anechoic chamber. In an anechoic chamber, high frequency absorbing material on the walls and the ceiling absorbs possible energy to reduce reflections. The shielding of the chamber isolates the ambient noise to avoid influences on the measurement result. Usually, chamber-based field measurements are preferred as the measurement environment is less noisy in comparison to an OATS.

---

[5] The role of both couplings will be investigated later in detail.

The CISPR 25 standard [4] defines ALSE-measurement setups in detail. The measurements are performed inside a semi-anechoic chamber using a specified configuration. Figure 1.2 illustrates the setup for the 150 kHz to 30 MHz frequency range. As defined in the standard, a typical measurement setup consists of the **e**quipment **u**nder **t**est (EUT) with control units, loads, **a**rtificial **n**etworks (ANs), power supplies, the cable bundle, and other peripheral equipment. The EUT with the attached cable bundle needs to be placed on a table with a metal surface, which is bonded to the chamber ground and the chamber walls. The metal surface substitutes the car chassis, which is the reference ground of the measurement setup, and shall be made from well-conducting metal, such as copper or aluminum. The table's height above the chamber floor is 0.9 m. The cable bundle has a length of 1.5 m up to 2.0 m. It is positioned 0.05 m above the metal plate by a non-conductive, low permittivity material. The distance to the edge of the metal plate is 10 cm. A rod antenna is positioned 1 m in front of the measurement setup and represents the on-board antenna. It is located adjacent to the center of the cable bundle. The measured antenna voltage multiplied with the antenna factor, given by the antenna manufacturer, gives the electric field strength[6].

Different antennas have to be used depending on the frequency range of interest. The antenna types and the related field polarization are listed in Table 1. A 1 m long rod antenna is used for the frequency range from 150 kHz to 30 MHz. For the frequency range from 30 MHz to 1 GHz, a biconical antenna and a log-periodic antenna are used. Also, compact combinations can be applied, like a BiLog antenna [5]. At higher frequencies, the emissions must be measured in both vertical and horizontal polarizations referenced to the ground plane of the test site. At lower frequencies (150 kHz to 30 MHz), only vertical polarization is required, as horizontal component is very small due to the metal surface.

TABLE 1: RECOMMENDED ANTENNA TYPES AND RELATED FIELD POLARIZATION FOR FIELD MEASUREMENTS (ACCORDING TO ALSE METHOD)

Frequency range	Antenna type	Polarization
150 kHz - 30 MHz	1-m-long vertical monopole	Vertical
30 MHz - 200 MHz	Biconical antenna	Vertical and horizontal
200 MHz - 1 GHz	Log-periodic antenna	Vertical and horizontal

A measurement receiver, which is shown in Figure 1.2, is located outside the chamber and measures the antenna voltages. If we focus on the differences in measurement setups, the first is that different antenna types and polarizations are used in the measurements. Moreover, Figure 1.2 involves a metallic plane between the table and the rod

---

[6] This approach is specified in the standard, but from technical point of view problematic. Details are discussed later.

antenna, which ensures the rod antenna (vertical monopole) has the same ground as the reference ground.

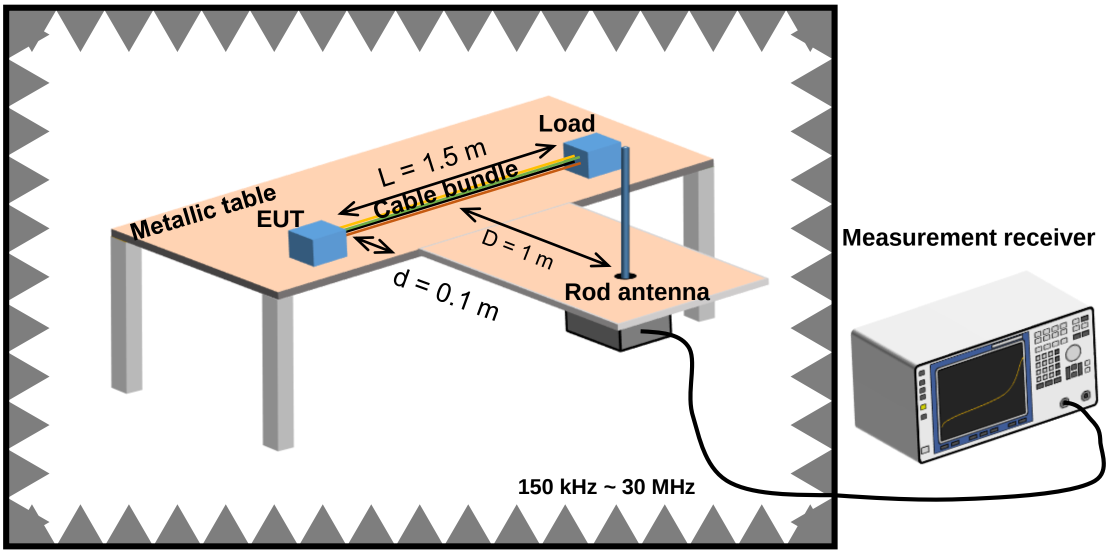

Figure 1.2: Sketch of a CISPR 25 measurement setup for frequency below 30 MHz.

1.3 Motivation and Aim

ALSE field measurements, according to the CISPR 25 standard, require much space, and the equipment is expensive to purchase and to maintain [6]; not all automotive electronics suppliers can afford it. Many suppliers cooperate with external EMC laboratories for the measurement of their products. Most EMC measurement plans ask for measuring at different prototype stages during the development process of a new product to ensure in-time EMC performance of the final product [7]. Due to strict time schedules and limited access to EMC measurement equipment, EMC engineering is challenging. New substitution methods should be less expensive and space-consuming.

The methods should provide at least estimations of the field data that a CISPR 25 compliant measurement would yield to substitute the early development stage measurements. Moreover, new methods should cover the frequency range from 150 kHz to 1 GHz. This work focuses on finding an alternative method for the low frequency range up to 30 MHz.

For frequencies above 30 MHz, common-mode current measurements combined with a **m**ulti-**d**ipole **m**odel (MDM), e.g., described in [8] for field estimation has been applied successfully in different research works. For creating the MDM, the cable bundle is often substituted as a single-wire cable carrying the common-mode currents. Below 30 MHz, the MDM method has difficulty in retrieving the electric field at the antenna location. The underlying mathematical functions that convert the measured current to the electric field at antenna location become at low frequencies very sensitive to small measurement errors.

To substitute CISPR 25 measurements a closer look on the setup is needed. The standard specifies an E-field sensitive rod antenna, that supposes to reproduce the behavior of the vehicle receiving antenna, to measure the radiated emissions. In the measurement, the antenna outputs a voltage, but the standard defines the limits of emissions in terms of electric fields. To calculate the antenna field from the measured antenna voltage, the measured antenna voltage must be converted with the help of an antenna factor.

At low frequencies, the rod antenna is placed in the near-field region of the structure. The antenna is mainly an electrical field sensor, and due to the length, it integrates the inhomogeneous E-field along the antenna. This means the full antenna characteristic, which leads to the antenna voltage, must be considered. Considering the field at a single point does not make sense. Thus, the standard approach is problematic, where the electric field distribution is approximated by an average value, when using an antenna factor. Therefore, the prediction of a single field value is problematic. Deviations should be expected. This inconsistency can be considered as a deficiency of the standard.

At low frequencies it would have been more consequent to consider the major coupling mechanism, which is capacitive coupling and is illustrated in Figure 1.3. The potential sources can be the cable bundle, the load, or the EUT. Often the coupling from the cable bundle dominates. Only when the EUT or the load is large, coupling to the antenna can be high. The antenna voltage would be much more expressive than the electric fields.

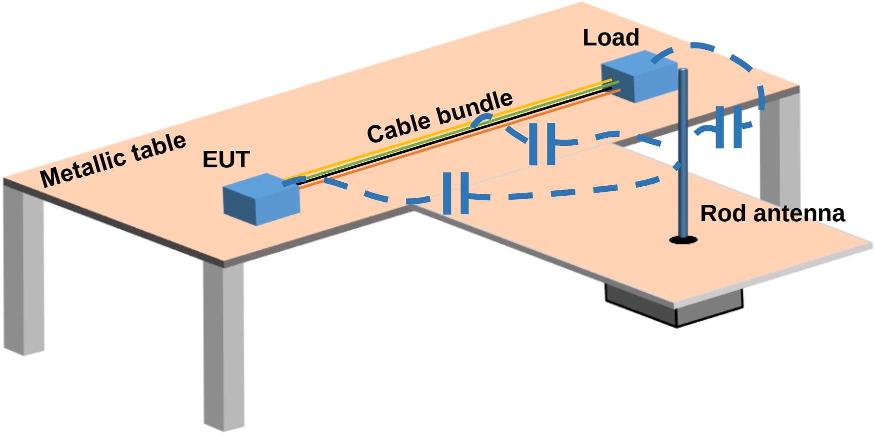

Figure 1.3: Possible coupling (capacitive) from cable bundle, EUT, and load.

If an alternative method can predict the voltage of a typical CISPR 25 low frequency antenna, it can be expected that the method works.

This thesis proposes new methods for antenna voltage prediction at frequencies below 30 MHz to overcome the mentioned problems. The antenna voltage prediction should be based on local electric field measurements. The local field measurements, very close to the EUT, can be much more robust compared to measurements at 1 m distance. Thus, the measurement complexity can be reduced significantly.

Computing the field distribution along the CISPR 25 rod antenna should be performed by using the surface equivalence theorem (Huygens principle) or static dipoles. It is expected that the new methods lead to a much more robust antenna voltage prediction, compared to common-mode current based methods [9],[10]. Moreover, by applying the field distribution with the Huygens principle, not only the emissions from the cable bundle structure are included, but also from all peripherals. Also, the cable bundle does not need to be substituted by a single wire. Thus, possible inaccuracies of wire approximations can be avoided.

The Huygens principle originates from high frequency applications and is often used for antenna analysis [11],[12]. Many publications on antenna applications consider the Huygens principle to be a synonym of the surface equivalence principle, e.g. [13]. This work uses this definition too. The surface equivalence principle can be applied by distributing equivalent current sources over a defined, so-called Huygens’ surface [11] (pp. 229-233). The equivalent currents are often calculated by using measured field data that are obtained from a near-field scan firstly. Then, the field at any point can be predicted in front of the Huygens’ surface. Chapter 3 will describe the principle in detail.

Figure 1.4 illustrates both substitution methods proposed in this work. Instead of direct measuring antenna voltage at 1 m distance (standard field measurement setup, see Figure 1.2), several electric field probes are introduced close to the structure (subfigure (a)). The measured field can be used either with the static dipole-based method or with the Huygens principle-based method to predict the fields at the antenna location.

The static dipole-based method is shown in Figure 1.4 (b). A quasi-static charge distribution [14] represents the current through the cable at very low frequencies. A subdivision of the cable into short segments with constant charge can approximate a charge distribution. A set of static dipoles representing charged segments is applied, where the charges (charge densities) can be calculated based on measured electric fields. The charges with opposite polarity represent the influence of the metallic table. This method is simple to apply for low frequencies and is described in chapter 5, section 5.3. The deficiency of this method is that the current is ignored, which can introduce a deviation in the predicted electric field at higher frequencies (here the magnetic field cannot be neglected any more). But for low frequencies this simplification should not be a problem in predicting the antenna voltage, as the CISPR 25 rod antenna is mainly sensitive to electric fields.

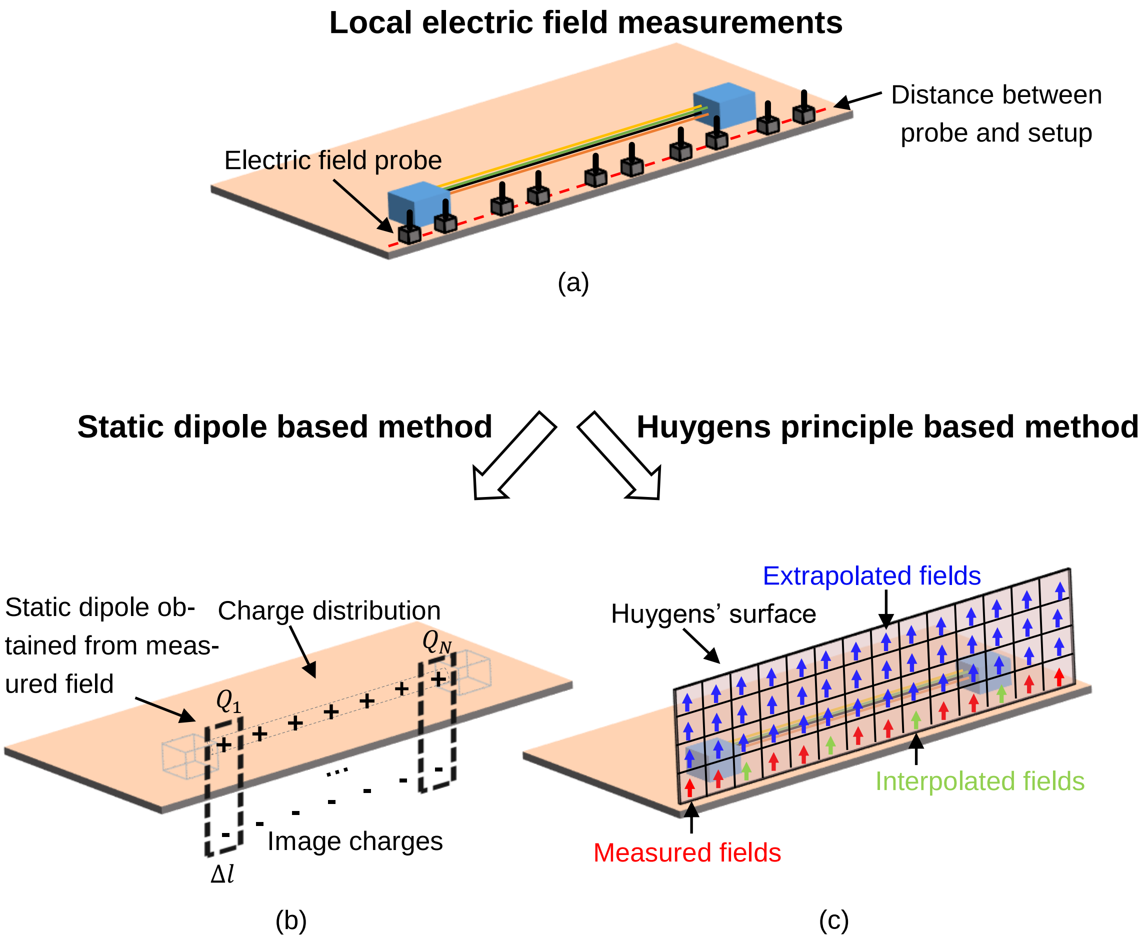

Figure 1.4: Proposed methods based on local field measurements.

Figure 1.4 (c) illustrates the concept of the proposed Huygens principle-based substitution method. The field distribution on the Huygens' surface is required here to apply the method. The near-field amplitudes are needed to be measured only at a few local positions. Interpolation and extrapolation methods can be applied to obtain an overall field distribution on a defined Huygens' surface. In the figure, the red arrows represent measured fields, the green arrows represent interpolated fields, and blue arrows represent extrapolated fields. The obtained field distribution is used to calculate the equivalent current sources, which are applied then to compute fields at the antenna location. By using this method, emissions of the whole structure (including the cable bundle, EUT, and load) are characterized by the equivalent currents on the Huygens' surface according to the surface equivalence principle.

1.4 Structure of the Work

This thesis is structured as follows:

- Chapter 1 provides an introduction to the work.

- Chapter 2 summarizes the state of the art of the topic, and proposes the two main scientific questions that should be answered in this dissertation.
- Chapter 3 describes the theoretical background of theorems used in this work, for example, the derivation of the Huygens principle, the electric field integral equation, and the numerical field integration methods.
- Chapter 4 analyzes the field measurement setups defined in CISPR 25. The standard measurement setups are analyzed analytically and numerically. The influence of terminations to the fields, the field distribution at the rod antenna location, and the possible coupling mechanisms from cable structure to the rod antenna are investigated and discussed.
- Chapter 5 describes electric field estimation methods, including the MDM method, electric field integral equation, static dipole-based method, and the Huygens principle-based method. Along with the description and discussion of the methods, the main research questions formulated in chapter 2 are answered.
- Chapter 6 explains the local electric field measurements.
- Chapter 7 validates the proposed near-field measurement-based methods with additional examples and compares the methods in the discussion.
- Chapter 8 concludes this work and gives an outlook.

2 State-of-the-Art

Over the years, many investigations had the goal of predicting field emissions of CISPR 25 ALSE setups based on simplified measurement setups. A simpler setup should substitute the complex CISPR 25 setup. Such substitution methods must consider multiple aspects: the emission sources, including the EUT and the attached cable bundle, the effects of the ALSE, and the influence of the finite metallic table. As different measurement concepts are used below 30 MHz, and above 30 MHz in the CISPR 25 ALSE method, the literature can be divided into two groups. In the low frequency range, approximately up to 30 MHz, the setup structures are electrically small. The rod antenna is sensitive mainly to electric fields and is placed in the near-field region. The antenna voltage will primarily be generated due to the voltage distribution on the cable bundle [15],[16]. At higher frequencies, the emission of the connected electric components, e.g., **p**rinted **c**ircuit **b**oards (PCBs), have to be taken into account [17].

The various concepts proposed in the literature for the substitution of the CISPR 25 ALSE method will be discussed in this chapter in detail concerning the frequency range above 30 MHz and below 30 MHz.

2.1 Field Prediction Methods for Frequencies Above 30 MHz

For frequencies above 30 MHz existing substitution methods can be roughly categorized into two groups. The first group is based on common-mode current measurements over the cable bundle. The second group is based on near-field measurements.

Several papers have discussed the first group of methods. This group is based on the dominant effects of the common-mode currents, as shown, e.g., in [18]. Common-mode currents can easily be measured. The common-mode current measurement-based methods can again be subdivided into two basic methods. The first one is based on transfer functions between the measured common-mode currents and the antenna voltage. The second one is based on creating a radiation model [8],[19],[20],[21], from the common-mode currents along the cable for the calculation of the antenna fields. Mainly a **m**ulti-**d**ipole **m**odel (MDM) was proposed. Here first, a set of Hertzian dipoles [12] must be created, and then the dipole parameters have to be determined from the measured common-mode currents. Radiation can also be calculated using the **e**lectric **f**ield **i**ntegral **e**quation (EFIE), as described in section 3.3.

A transfer function method for CISPR 25 has been discussed the first time in [22]. Here the cable bundle is segmented, and the common-mode current is measured along the cable bundle in the middle of each segment. With the measured antenna field, a transfer function for each cable segment current to antenna voltage can be found. The measurements for obtaining the transfer functions are performed inside an ALSE. Thus the effects of the chamber, such as the anechoic chamber resonances, were included in the transfer functions. However, the transfer functions only describe the correlation between the current amplitudes and the received antenna fields. The phase distribution of the current is only considered by a simple estimation method. The approach achieved an agreement between the measured field and the predicted field of +/- 5 dB for frequencies between 10 MHz and 190 MHz. More developments of the method were described, for example, in [23]-[25]. Different from [22], in [23], the phase information was extracted directly from scattering parameter measurements with a **v**ector **n**etwork **a**nalyzer (VNA). As VNA measurements are not compliant with the standards, their applicability is limited. In [24], the common-mode current amplitudes, measured with an EMI test receiver in peak mode, were used to estimate current composite waves consisting of forward and reflected waves. The current phase distribution along the cable bundle can be retrieved by analyzing the **c**urrent **s**tanding **w**ave **r**atio (CSWR). This method achieved electric fields in both horizontal and vertical polarization at higher frequencies, but an error of around 10 dB from 30 MHz to 200 MHz is still high. Also, this method fails to predict fields at resonance points (as shown in the paper, the resonance point is at $\lambda/2$). The abovementioned transfer functions based field prediction methods require that the transfer functions extracted inside an ALSE for a fixed setup and load condition. Applying the obtained transfer functions to more general measurement setups and load conditions may cause wrong results.

In the first group of methods, also the radiation-model-based methods can be found. The methods assume a simplification of the cable bundle to a single equivalent transmission line [26] that carries the common-mode currents. Here mainly, the MDM is proposed. The transmission line was segmented, and each segment substituted with a Hertzian dipole [27]. The center of the segment is the center of the dipole. Due to the metallic table, the dipoles are also placed on the image of the transmission line and oriented in reverse direction [2],[13]. The antenna fields are calculated by using the dipole model.

For the transfer function methods and the MDM methods, the common-mode currents are needed, which were measured by a current probe. However, dynamic ranges and working frequency range of current probes are limited. For example, the current accuracy for a defined CISPR 25 setup was discussed for two different current probes in [28]. It has been shown that only current probes may not reach the required sensitivity, especially for local minima of current on the transmission line. Improvements like low noise amplifiers might be necessary. In many publications, e.g. [9], common-mode current measurements were performed with a current probe (often the FCC F-65 [29] is applied) in the frequency domain. Only the current amplitude was measured. To obtain the phase, in [9] an optimization procedure is used to determine parameters of the transmission line. By fitting the transmission line parameters, excitations, and impedances to measured current amplitudes, some phase information of common-mode currents could be retrieved. In [19], the common-mode currents were measured in the time domain with an oscilloscope. An additional probe was involved at the EUT side as the phase reference. Both current amplitude and phase information can be obtained at the same time, as the phase was extracted as the difference between the current probe and the phase reference probe.

Since the MDM only considers parts of the measurement setup's geometry, additional considerations of the measurement setup are needed to improve the predicted fields. In [8] and [20], the influence from currents in the metallic table was considered, where the finite metallic table of the measurement setup was modeled by using a **p**hysical **o**ptics (PO) approach [30] with equivalent surface currents. [31] introduced additional correction functions to compensate the influence of the CISPR 25 setup for a created MDM. Here, the correction functions, obtained by a monopole or dipole antenna, in an ALSE represent the correlations between a measured antenna voltage and dipole moment in each direction and location in a Cartesian coordinate system. Furthermore, a magnetic field probe can be used to measure the magnetic near-field distribution over the cable. The equivalent current distribution can be retrieved using a dipole-moment based source reconstruction method [32]. The correction functions were applied to the retrieved current distribution to calculate the antenna voltage, including ALSE characteristics, as the antenna effects are challenging to model and can have complex behavior. In [19], an additional calibration procedure inside an ALSE is proposed. Finally, for frequencies above 30 MHz up to 1 GHz, an improved method considering many of the points mentioned above, including the calibration process and additional surface currents, was described in [8].

The second group of methods focuses on near-field measurements for field prediction. For example, in [33], the Huygens principle and the image theory are applied for near-field to near-/far-field transformation for any arbitrary near-field geometry, where the equivalent magnetic currents were calculated based on measured electric field distribution over a defined scan plane. In [34], measured electric field data were used to calculate equivalent electric currents for near-field to near-/far-field transformation. The Huygens principle and the image theory were also used for field prediction of a radiating structure over a ground plane [35]. Here only the vertical electric fields and one tangential component (parallel to the ground plane) of magnetic fields were scanned to obtain equivalent current sources over a defined Huygens' surface. The paper also suggested to scan near fields only on a small part of the Huygens' surface (four lines) and the top plane instead of the whole defined Huygens' cube in order to save scan time and cost. The application of the Huygens principle in [35] was simplified, for example, in [36] in which equivalent current sources were obtained from only measured tangential magnetic near-field data by applying the **f**inite **e**lement **m**ethod (FEM) [37]. For the

CISPR 25 setup at a frequency range from 30 MHz up to 1 GHz, the Huygens principle was applied but only validated with the help of simulated field data, for example, in [38]. No measured near-field data was used. [39] extended the application of [38] by adding S-parameter measurements for obtaining EUT-to-antenna couplings in CISPR 25 setups, but still, it was only verified using simulation data.

2.2 Field Prediction Methods for Frequencies Below 30 MHz

For frequencies below 30 MHz, dimensions of the cable bundle length, antenna distance to EUT, and antenna length are in the range of 1-2 m. Even the other dimensions, like the ALSE walls, are shorter than 5 m. In free space, the wavelength at 30 MHz is 10 m, i.e., the dimensions are shorter or even much shorter than the wavelength. Methods focusing at frequencies below 10 MHz can well assume for most coupling effects quasi-static conditions. Such an assumption might fail for higher frequencies. Furthermore, the requested CISPR 25 rod antenna is terminated with a high input impedance amplifier for frequencies below 30 MHz. I.e., the antenna is mainly sensitive to electric fields and not sensitive to the magnetic field. These special conditions lead to different field prediction approaches. There are many fewer publications on low frequencies compared to the high frequencies. The literature can be divided into two groups.

The first group is based on an equivalent circuit model, mainly considering the capacitive coupling between EUT and rod antenna, e.g., [15],[40],[41]. As for very low frequencies, quasi-static approaches are valid, and circuit theory can be a powerful tool for finding the antenna voltage for the lower frequency range [42]. For characterizing the EUT, the common-mode voltage distribution can be measured, as performed in [15],[16]. Possible electric couplings between the EUT and the rod antenna for the low frequency range were analyzed in a simplified CISPR 25 measurement setup, in which a cable has been excited by an ideal current source and has been terminated with an ohmic load. For the simplified configurations, which do not represent the full properties of a real setup, the results were acceptable. In [43], a hybrid circuit model is proposed, which includes a combination of measured S-parameters and equivalent circuits. Here, load and IC models were included in the model. The measured S-parameters consider the ALSE setup. As S-parameter measurements can be very complex for cable bundles, this method is very difficult to apply for bundles with a variety of wires. In [44], a method of measuring the common-mode voltage distribution is described, similar to [15],[16] with the same problems. In [45], the cable bundle was substituted by a charged straight wire. The fields caused by the wire were calculated by multiplying a measured common-mode voltage spectrum with a constant transmission factor. The method showed a low accuracy. At about 250 kHz 20 dB deviation between the predicted field value and an ALSE measurement has been found. Also above 10 MHz, the method failed.

The second group is based, similar to the high frequency approaches, on measured common-mode currents. For example, in [10], an application of a single transfer function method for an electric drive system below 30 MHz was presented. It gave a maximal 9 dB deviation between the predicted fields and the standard field measurement result. However, the method is limited to setups of the same termination impedances. This is not valid in real applications. Transfer function or impedance measurement is complex and time-consuming and would not simplify ALSE in this case. The dissertation [21] tries to apply the MDM method to frequencies below 30 MHz. Since the currents in the MDM were based only on common-mode current measurements with limited accuracy, this method had to fail. The reasons will be discussed later in this work.

Common to all proposed methods is that the cable structure was not a complex bundle. But complex cable bundles have to be expected in real applications. Here shielding effects of surrounding cable can significantly influence the results. Furthermore, the fields from the terminating devices were not considered. As long as there is no contribution to the antenna voltage, e.g., the devices are small or shielded, the results were satisfying. In real applications, the devices can even dominate the antenna voltage, e.g., when a large unshielded PCB is involved. In such cases, a purely single wire-based antenna voltage prediction will fail.

2.3 Research Questions

As described above, the CISPR 25 ALSE method should be substituted at least for pre-compliance measurements also for low frequencies. From the above analysis, it can be seen that radiation model-based techniques (e.g. [9],[20]) and transfer functions based methods (e.g. [22],[24]) provide good accuracy for frequencies above 30 MHz. It can be seen that radiation model-based methods have the advantage that they are not limited to fixed load conditions. Complex load impedance measurements are not required. However, the radiation model-based methods fail below 30 MHz. Therefore, the first major question is why the radiation model-based method fails.

Another important aspect is the consideration of complex bundles and the field emitting termination devices. The common-mode voltage methods give satisfying results for simple configurations but fail with complex cable bundles and emitting terminations. Here near-field scan methods are much more promising.

The advantage of near-field scan methods is that a complex geometry of an original emission sources does not need to be considered, which could be any arbitrary structure since only near-field data is relevant for field calculation. Many publications assume simplified geometries with simple dominating field emitting structures. Real CISPR 25 measurement setups can be very complex. Terminating devices can be large, and cable bundles can consist of 20 or more cables. As described above, a near-field scan

can obtain electric field data, e.g. [33],[34], or both electric and magnetic data, e.g. [35], or only magnetic field data, e.g. [36]. From a measured spatial field distribution, equivalent sources can be calculated and used for field prediction based on the Huygens principle and the image theory. In literature, until now, near-field scan methods were only applied mainly to the frequency range above 30 MHz. In this work, near-field scanning, in combination with the Huygens principle, should be investigated. Are such methods applicable for frequencies below 30 MHz and how methods can be applied? This is the second major question to be answered in this work.

3 Theoretical Background

This dissertation focuses on alternative field prediction methods for low frequencies. As described in the previous chapter, the motivation of the work is to find a proper method capable of connecting low frequency and high frequency prediction for CISPR 25 standard field measurements. The Huygens principle is therefore introduced, which will be described in this chapter. In high frequencies applications, such as in antenna analysis, the Huygens principle is often applied. As the principle has no frequency limitations, it can also be applied to low frequencies. This will be figured out in this chapter from a theoretical point of view. Furthermore, the theory will be prepared for the application of the Huygens principle to predict the CISPR 25 field values.

Before summarizing the content of the surface equivalence theorem based on [13] (pp. 328-331), Maxwell's equations will be repeated in a less commonly used form. The magnetic current density and magnetic charge density are used in the Maxwell's equations according to the duality theorem [13] (p. 311). Although the magnetic current density and magnetic charge density do not have a physical representation, both terms are necessary for the explanation of the surface equivalence theorem. An equivalent surface (so-called Huygens' surface [11] (pp. 229-231)) should be defined to apply the surface equivalence theorem for field prediction in a real application. Furthermore, an integral over the sources distributed over the Huygens' surface is required to find the external fields [11] (pp. 229-231). Therefore, after the introduction of the surface equivalence theorem, a derivation of a general EFIE will be presented, in which both electric and magnetic sources contribute to the field at an observation point.

Based on the fact that magnetic sources are not physical, this work further applies the more commonly used EFIE for metal structures, which considers only electric sources. The widely used EFIE is very helpful to analyze dominant emission sources (charges or currents) for the CISPR 25 structure (see chapter 4). In the end, the numerical treatment of the EFIE will be discussed, as it is required to compute the electric field at the observation point based on the equivalent current sources on the Huygens' surface.

3.1 Maxwell's Equations

Compared to the commonly used Maxwell's equations, in this work, magnetic charge density and magnetic current density are considered in Maxwell's equations by applying the duality theorem [13] (p. 311). The magnetic charges and magnetic currents have no physical nature. Here, the differential form for harmonic excitation is given:

$$\nabla \times \vec{H} = j\omega\varepsilon\vec{E} + \vec{J}, \tag{3.1}$$

$$\nabla \times \vec{E} = -j\omega\mu\vec{H} - \vec{M}, \tag{3.2}$$

$$\nabla \cdot \vec{E} = \frac{\rho}{\varepsilon}, \tag{3.3}$$

$$\nabla \cdot \vec{H} = \frac{\rho_{\mathrm{m}}}{\mu}, \tag{3.4}$$

where:

$\vec{E}$	electric field intensity,
$\vec{H}$	magnetic field intensity,
$\vec{J}$	electric current density,
$\vec{M}$	fictitious magnetic current density,
ρ	electric charge density,
ρ_{m}	fictitious magnetic charge density,
ε	permittivity of the medium, in vacuum $\varepsilon = \varepsilon_0 = 8.85 \times 10^{-12}\ \mathrm{F/m}$,
μ	permeability of the medium, in vacuum $\mu = \mu_0 = 4\pi \times 10^{-7}\ \mathrm{H/m}$.

Furthermore, currents and charges of both types are related by the continuity equations, which can be expressed by:

$$\nabla \cdot \vec{J} = -j\omega\rho, \tag{3.5}$$

$$\nabla \cdot \vec{M} = -j\omega\rho_{\mathrm{m}}. \tag{3.6}$$

It has to be noted again that both the magnetic current density $\vec{M}$ in (3.2) and the magnetic charge density ρ_{m} in (3.4) are imaginary sources; they do not represent physical sources. The introduction of the imaginary sources is required for the derivation of the surface equivalence theorem, which will be presented in the following section.

3.2 Surface Equivalence Theorem (Huygens Principle)

The Huygens principle, named after the Dutch physicist Christiaan Huygens, initially introduced in physical optics to predict the propagation of light. It states that each point on a primary wavefront can be considered to be a new source of a secondary spherical wave and that a secondary wavefront can be constructed as the envelope of these secondary spherical waves [46] (p. 465). Figure 3.1 shows the fundamental principle applied to physical optics.

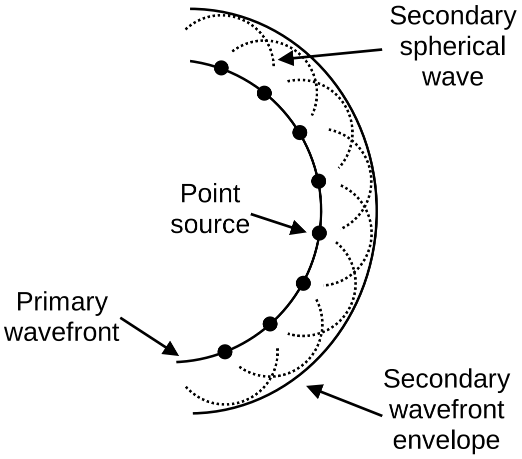

Figure 3.1: Huygens principle.

Initially, the principle was applied to predict the propagation of light, respectively, electromagnetic waves that satisfy the electromagnetic wave equations in source-free regions. This means that source currents and charges were not included. Consequently, the effects of the reactive fields close to the radiating sources were not considered.

Rigorous formulations of the Huygens principle, i.e., for the fields in terms of equivalent surface current sources, can be found in [13],[46],[47] and [48]. The surface equivalence theorem is consequently a more general formulation. In the literature, different “surface equivalence theorems” have been formulated, often subsumed as “Huygens principle”. A good introduction is given, for example, in [13] (pp. 328-331). Further explanations are mostly taken from this textbook. In this dissertation, the more rigorous formulation of the Huygens principle is applied, as it was introduced first by Love [49], and then further extended by Schelkunoff [50] (Schelkunoff [50] cited Love [49] and proposed other forms of equivalence theorems). In later chapters of this work, the expression “Huygens principle” is used as a synonym for the “surface equivalence theorem”, because “Huygens principle” seems to be more illustrative.

“Huygens principle” or “surface equivalence theorem” have been applied in many publications. For example, the theorem was applied for the analysis of antenna radiation characteristics of wire antennas as well as aperture antennas, e.g. [51]. The major advantage of the theorem in practical applications is its ability to compute fields in an arbitrary point in space (far-field as well as near-field) without knowledge of the current distribution on the antenna structure itself. Only the fields close to the antenna structure that can be obtained from near-field measurements are required, e.g., [33]-[36].

Using the Huygens principle requires complete knowledge of the tangential electric and/or magnetic fields over a closed surface enclosing a radiating structure. As it is intuitive to compute fields from current sources, a set of equivalent electric and magnetic currents distributed over the closed surface is applied. A more detailed explanation of the main idea is given below.

The idea to use equivalent surface currents is based on Love's equivalence principle [49], which states that the distribution of electric and magnetic currents on a given surface S can be found such that outside of S, which produces the same field as that produced by given sources inside S. And equally the field inside S can be produced by a distribution of currents on S that can be the same as that derived from the fields outside S. A detailed proof from physical point of view can be found, e.g., in [50]. An example of interpreting the principle is shown in Figure 3.2.

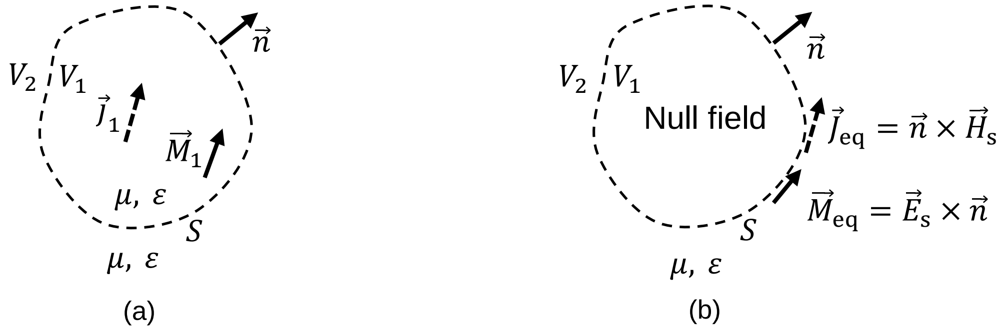

Figure 3.2: Original problem (a) with radiating source densities $\vec{J}_1$ and $\vec{M}_1$. According to Love's equivalence principle, (b) the original sources can be replaced by equivalent sources $\vec{J}_{\mathrm{eq}}$ and $\vec{M}_{\mathrm{eq}}$ on a closed surface with a null field inside.

The fields generated by actual sources can be characterized by the use of a set of equivalent current sources distributed on a closed fictitious surface (often-called Huygens' surface [11]), which encloses the original (actual) sources. Figure 3.2 (a) gives the original current source densities $\vec{J}_1$ and $\vec{M}_1$. S is the defined Huygens' surface. V_1 and V_2 are the two field regions divided by S. The original sources are inside V_1, and V_2 is a source free region. Figure 3.2 (b) illustrates a case for Love's equivalence principle, where the equivalent surface current sources $\vec{J}_{\mathrm{eq}}$ and $\vec{M}_{\mathrm{eq}}$ on the Huygens' surface can replace the original sources, producing the same fields as the original sources in the region V_2. A consequence of Love's equivalence principle is that the equivalent sources produce a null field in region V_1.

The equivalent surface current sources can be obtained from the original electric and magnetic fields on S and are expressed by:

$$\vec{J}_{\mathrm{eq}} = \vec{n} \times \vec{H}_{\mathrm{s}}, \tag{3.7}$$

$$\vec{M}_{\mathrm{eq}} = \vec{E}_{\mathrm{s}} \times \vec{n}, \tag{3.8}$$

where the electric fields ($\vec{E}_{\mathrm{s}}$) and magnetic fields ($\vec{H}_{\mathrm{s}}$) are fields over the defined Huygens' surface S generated by the original sources in the region V_1. $\vec{n}$ is the normal vector of Huygens' surface pointing to the outer side in the case that the original sources are located inside of the surface S. Since the region V_1 is a null field region (this region is not of interest), the medium can be considered the same as that in region V_2. Consequently, the equivalent current sources radiate into an unbounded homogeneous medium, which means the equations (3.7)-(3.8) together with (3.12)-(3.13) and (9.32)-(9.33) can be applied to find fields everywhere [51] (pp. 653-657)[7].

Auxiliary vector potentials are often applied to calculate the radiated fields based on (equivalent) current sources (in this case, the sources are equivalent electric and magnetic current sources over the defined Huygens' surface). Later, a solution with the help of auxiliary vector potentials will be described, and a general formulation of field integral will be derived based on both electric and magnetic current sources. However, before that, to provide a complete description of the principle, two further variants will be introduced as they can simplify the calculation in some practical cases.

For the sake of reducing the required equivalent sources on the Huygens' surface and consequently the required fields (less effort in the application of the method), two different variations of the equivalence principle can be derived, where only $\vec{M}_{\mathrm{eq}}$ or only $\vec{J}_{\mathrm{eq}}$ over the Huygens' surface is needed [13]. As the Love's principle states that fields within the imaginary surface are zero, these fields do not interact with the material inside and therefore cannot be disturbed, if the properties of V_1 are changed. Fields in V_2 are also not affected, since the boundary conditions on S are still satisfied. Filling V_1 with a **p**erfect **e**lectric **c**onductor (PEC, see Figure 3.3 (a)) or **p**erfect **m**agnetic **c**onductor (PMC, see Figure 3.3 (b)) does not change the conditions inside V_1. However, the introduction of a PEC in V_1 will short-circuit the equivalent electric current sources $\vec{J}_{\mathrm{eq}}$. Hence, they will not radiate but according to the uniqueness theorem [13] only magnetic surface current density $\vec{M}_{\mathrm{eq}}$ is necessary over S to reconstruct the field in V_2 in the presence of a PEC inside V_1. In case of a PMC inside V_1 the equivalent magnetic current is short-circuited and again according to the uniqueness theorem, only electric surface current density $\vec{J}_{\mathrm{eq}}$ is necessary to reconstruct the field in V_2.

---

[7] The equations (3.12) and (3.13) are solutions of the inhomogeneous vector potential wave equations (3.9) and (3.10). The derivation of the inhomogeneous vector potential wave equations can be found in appendix A. $\vec{E}$ and $\vec{H}$ fields can be obtained by applying the solutions (3.12) and (3.13) to (9.32) and (9.33).

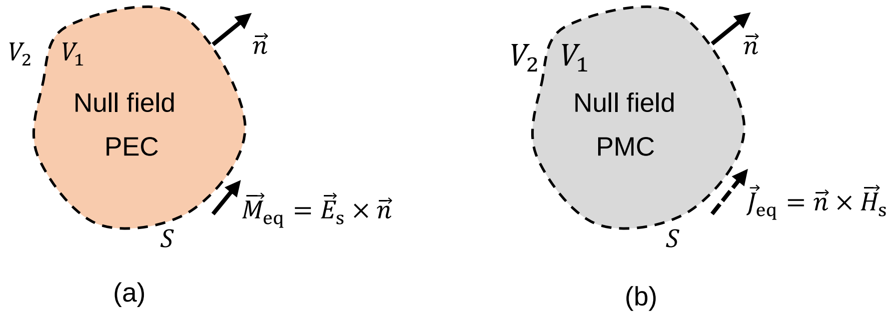

Figure 3.3: Equivalence principle models with radiating equivalent magnetic current sources due to PEC (a), and radiating equivalent current sources due to PMC (b) [51] (p. 657).

The involvement of PEC or PMC causes the equivalent source densities $\vec{M}_{\mathrm{eq}}$ or $\vec{J}_{\mathrm{eq}}$ to radiate into a bounded field region respectively. Consequently, additional techniques are required to consider the boundary condition to find the fields.

In many practical applications, the Huygens' surface is assumed to be an infinite large plane (closed in the infinite), whereby the field calculation can be simplified [51] (pp. 657-658). The idea is also described in [13] (pp. 329-331). Supposing a PEC or PMC within V_1, the boundary between V_1 and V_2 can be considered by applying the image theory (described later in section 3.8). To explain how the simplification works, Figure 3.4 gives an infinite large planar Huygens' surface and equivalent current sources $\vec{J}_{\mathrm{eq}}$ and $\vec{M}_{\mathrm{eq}}$ on the surface which are related to original sources inside V_1 [51] (p. 658). By filling the volume V_1 with PEC and by applying the image theory, it can be seen that the images of $\vec{M}_{\mathrm{eq}}$ and $\vec{J}_{\mathrm{eq}}$ are parallel to the plane. The image of the $\vec{M}_{\mathrm{eq}}$ is pointing to the same direction as the direction of the $\vec{M}_{\mathrm{eq}}$, whereas the image of the $\vec{J}_{\mathrm{eq}}$ is pointing to the opposite direction compared with the direction of the $\vec{J}_{\mathrm{eq}}$. By superimposing $\vec{M}_{\mathrm{eq}}$, $\vec{J}_{\mathrm{eq}}$ and their images, the resulting $\vec{J}_{\mathrm{eq}}$ is zero, but $\vec{M}_{\mathrm{eq}}$ doubles. As a result, $2\vec{M}_{\mathrm{eq}}$ can be considered as the equivalent current source. Therefore, there is no need to use $\vec{J}_{\mathrm{eq}}$. More important is that by applying the image theory, the equivalent current source $2\vec{M}_{\mathrm{eq}}$ radiates again into an unbounded medium. The equations (3.7)-(3.8) together with (3.12)-(3.13) and (9.32)-(9.33) can be used to calculate the fields on the right side of the plane. In a similar way, by applying PMC and the image theory, the $\vec{M}_{\mathrm{eq}}$ will be zero, and the $\vec{J}_{\mathrm{eq}}$ doubles (which will not be applied in the work, and is not shown in the figure).

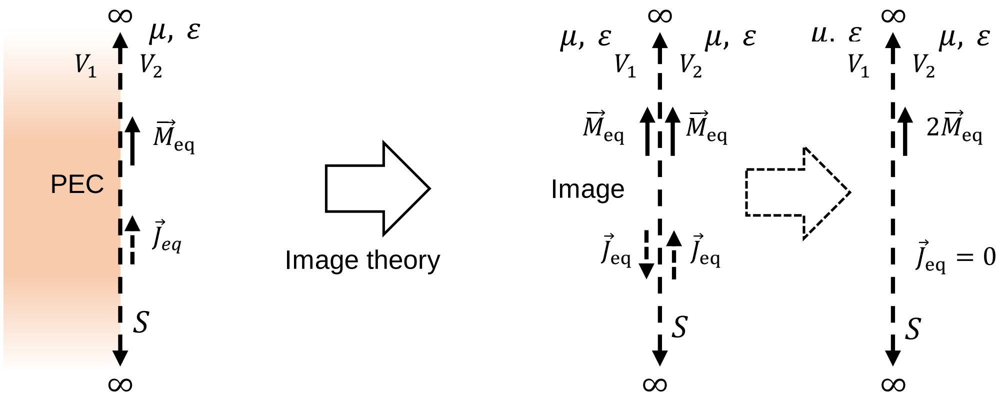

Figure 3.4: Application of the image theory to radiating equivalent source on an infinite large planar Huygens' surface with assuming PEC within V_1 [51] (p. 658).

This work will apply the idea of the simplification shown in the Figure 3.4, which requires only $2\vec{M}_\mathrm{eq}$ as the equivalent current source for predicting electric fields of CISPR 25 measurement setups. $\vec{M}_\mathrm{eq}$ will be determined by the equation (3.8) and local E-field measurements (see chapter 6). In chapter 5, section 5.4, the method will be described in detail.

3.3 Formulation of the Electric Field Integral Equation

The electric or magnetic fields from known electric and magnetic source densities (either actual or equivalent) can be calculated using the **e**lectric **f**ield **i**ntegral **e**quation (EFIE) that can be found, for example in [13] (pp. 679-688). In this dissertation, a derivation using auxiliary vector potentials is presented [51] (pp. 133-142). Auxiliary vector potential functions are often introduced to compute fields, as they can simplify the solution. The vector potentials do not represent any physically measurable quantities and are used only as a mathematical aid. The resulting electrical field integral equation serves as a basis in this dissertation to calculate the fields in an arbitrary point from the equivalent surface current sources described in the previous chapter.

The most common vector potentials are the magnetic vector potential $\vec{\mathrm{A}}$ and the electric vector potential $\vec{\mathrm{F}}$. A detailed derivation of the auxiliary vector potentials and the resulting field equations can be found in appendix A. The following explanations are related to finding the electric field resulting from an electric current source density $\vec{J}$ and magnetic current source density $\vec{M}$. This requires in a first step to find auxiliary vector potentials $\vec{\mathrm{A}}$ and $\vec{\mathrm{F}}$, which satisfy the inhomogeneous vector potential wave equations (see appendix A)

where $\beta^2 = \omega^2\mu\varepsilon$. Once the auxiliary vector potentials are found, the resulting field from the source densities $\vec{J}$ and $\vec{M}$ can be calculated in general with

$$\vec{E} = -j\omega\vec{A} - j\frac{1}{\omega\mu\varepsilon}\nabla\left(\nabla\cdot\vec{A}\right) - \frac{1}{\varepsilon}\nabla\times\vec{\mathrm{F}}, \tag{3.11}$$

$$\nabla^2\vec{\mathrm{A}} + \beta^2\vec{\mathrm{A}} = -\mu\vec{J}, \tag{3.9}$$

$$\nabla^2\vec{\mathrm{F}} + \beta^2\vec{\mathrm{F}} = -\varepsilon\vec{M}, \tag{3.10}$$

Here only a surface current density is required. Thus, solutions for the inhomogeneous vector potential wave equations (3.9) and (3.10) in case of surface current source densities are [13] (pp. 133-142):

$$\vec{\mathrm{A}} = \frac{\mu}{4\pi}\iint\limits_S \vec{J}_{\mathrm{s}}(x',y',z')\,\mathrm{G}(\vec{r},\vec{r}')ds', \tag{3.12}$$

$$\vec{\mathrm{F}} = \frac{\varepsilon}{4\pi}\iint\limits_S \vec{M}_{\mathrm{s}}(x',y',z')\,\mathrm{G}(\vec{r},\vec{r}')ds', \tag{3.13}$$

where $\vec{J}_s(x',y',z')$ and $\vec{M}_s(x',y',z')$ represent electric and magnetic surface current densities in the Cartesian coordinate system. $\mathrm{G}(\vec{r},\vec{r}')$ is the Green's function in free space, written as:

$$\mathrm{G}(\vec{r},\vec{r}') \ = \frac{\mathrm{e}^{-jkR}}{R}, \tag{3.14}$$

The parameter k is the wavenumber, which can be expressed as:

$$k \ = \omega\sqrt{\mu\varepsilon}, \tag{3.15}$$

R is the distance between the current source point to the observation point, which can be calculated by:

$$R = |\vec{r} - \vec{r}'| = \sqrt{(x-x')^2 + (y-y')^2 + (z-z')^2}, \tag{3.16}$$

where $\vec{r}$ is a vector from the origin of the coordinate system to the observation point. $\vec{r}'$ is a vector from the origin of the coordinate system to the current source densities.

Substituting the solutions (3.12) and (3.13) of the inhomogeneous vector potential wave equations into (3.11) leads to

$$\vec{E}(\vec{r}) = -\frac{1}{4\pi}\iint\limits_S \left[j\omega\mu\vec{J}_{\mathrm{s}}(\vec{r}')\mathrm{G}(\vec{r},\vec{r}') + j\frac{1}{\omega\varepsilon}\nabla\left(\nabla\cdot\left(\vec{J}_{\mathrm{s}}(\vec{r}')\mathrm{G}(\vec{r},\vec{r}')\right)\right) + \nabla \times\left(\vec{M}_{\mathrm{s}}(\vec{r}')\mathrm{G}(\vec{r},\vec{r}')\right)\right] ds'. \tag{3.17}$$

For a better presentation of the formulas the variables $\vec{r}$ and $\vec{r}'$ will be omitted in the following. The next steps are performed according to [52] (pp. 33-36) to reduce the equation mentioned above. The third term in (3.17) can be converted by applying the vector identity

$$\nabla \times \left(f\vec{\mathrm{A}}\right) = \nabla f \times \vec{\mathrm{A}} + f\left(\nabla \times \vec{\mathrm{A}}\right) \tag{3.18}$$

and considering that $\vec{M}_s$ is constant, related to the operator ∇. The second term can be converted by using the vector identities

$$\nabla \cdot \left(f\vec{A}\right) = \nabla f \cdot \vec{\mathrm{A}} + f\nabla \cdot \vec{\mathrm{A}} \tag{3.19}$$

and

$$\nabla \cdot \left(\vec{\mathrm{A}} \cdot \vec{\mathrm{B}}\right) = \left(\vec{\mathrm{A}} \cdot \nabla\right)\vec{\mathrm{B}} + \left(\vec{\mathrm{B}} \cdot \nabla\right)\vec{\mathrm{A}} + \vec{\mathrm{A}} \times \left(\nabla \times \vec{\mathrm{B}}\right) + \vec{\mathrm{B}} \times \left(\nabla \times \vec{\mathrm{A}}\right) \tag{3.20}$$

which leads to the reduced form of (3.17),

$$\vec{E} = -\frac{1}{4\pi}\iint\limits_{S}\left[j\omega\mu\vec{J}_{\mathrm{s}}\mathrm{G} + j\frac{1}{\omega\varepsilon}\nabla\left(\vec{J}_{\mathrm{s}} \cdot \nabla\right)\nabla\mathrm{G} + \nabla\mathrm{G} \times \vec{M}_{\mathrm{s}}\right]ds'. \tag{3.21}$$

Considering the symmetry of Green's function, the following relations are valid [52] (p. 34):

$$\nabla\mathrm{G} = -\nabla'\mathrm{G}, \tag{3.22}$$

$$\left(\vec{J}_{\mathrm{s}} \cdot \nabla\right)\nabla\mathrm{G} = \left(\vec{J}_{\mathrm{s}} \cdot \nabla'\right)\nabla'\mathrm{G}, \tag{3.23}$$

where the prime indicates the relation to the coordinate system of the sources. The order of the divergence operation of $\vec{J}_{\mathrm{s}}$ in (3.21) can be interchanged ($\vec{J}_{\mathrm{s}} \cdot \nabla' = \nabla' \cdot \vec{J}_{\mathrm{s}}$). The resulting electric field integral equation can then be written as

$$\vec{E} = -\frac{1}{4\pi}\iint\limits_{S}\left[j\omega\mu\vec{J}_{\mathrm{s}}\mathrm{G} + j\frac{1}{\omega\varepsilon}\left(\nabla \cdot \vec{J}_{\mathrm{s}}\right)\nabla'\mathrm{G} - \nabla'\mathrm{G} \times \vec{M}_{\mathrm{s}}\right]ds'. \tag{3.24}$$

The equation (3.24) is a general electric field integral equation formulation, which represents a sum of the electric field contributed from both electric and magnetic current source densities on a surface. This formulation is also the basis of this work for calculating the electric field. The equivalent electric and magnetic current source densities are retrieved from near-fields by applying the surface equivalence theorem described in section 3.2. As the surface equivalence theorem states that the equivalent currents on a closed surface include all information about the enclosed sources, the electric field integral equation (3.24) considers both near and far-field effects from the original sources.

The integral equation for the magnetic field $\vec{H}$ can be also derived by performing similar steps like (3.11)-(3.24) to the equation (9.33) in Appendix A. Since the work focuses mainly on $\vec{E}$, the detailed derivation for $\vec{H}$ will not be given here. A detailed derivation can be found in e.g. [11] (pp. 229-233) or [48] (pp. 464-468).

The general electric field integral equation (3.24) can also be applied to electromagnetic radiation/scattering problems of metallic structures. In this work, it will be used to analyze the emissions of CISPR 25 structures. In this case, boundary conditions of the structure (conductivity) have to be considered. The derivation is shown in the next section.

3.4 Electric Field Integral Equation for Metallic Structures

We start with the derivation of the electric field integral equation for scattering problems based on the boundary condition of a scatter (metallic surface or wire), which is assumed to be a **p**erfect **e**lectric **c**onductor (PEC). This is described, e.g., [13]. Although in this work, the scattering solution is not needed, the derivation is very helpful in understanding the contribution of the possible field sources. By illuminating a metallic structure (PEC) with an incident electric field, a total field can be expressed by

$$\vec{E} = \vec{E}^{\mathrm{i}} + \vec{E}^{\mathrm{s}}, \tag{3.25}$$

where $\vec{E}$ is the total field, $\vec{E}^{\mathrm{i}}$ is the incident field and $\vec{E}^{\mathrm{s}}$ is the scattered field. The tangential component of the electric field on the surface of the PEC has to be zero, which means (3.26) has to satisfy the boundary condition, for example, described in [13] (p. 704) or [53] (p. 17)

$$\vec{E}^{\tan} = \left(\vec{E}^{\mathrm{i}} + \vec{E}^{\mathrm{s}}\right)^{\tan} = 0. \tag{3.26}$$

The incident field $\vec{E}^{\mathrm{i}}$ induces an electric current density $\vec{J}_{\mathrm{s}}$ on the conducting surface of the scatter, which in turn emits the scattered field $\vec{E}^{\mathrm{s}}$. For the surface current density and the fields on the surface

$$\vec{n} \times \vec{H}^{\tan} = \vec{J}_{\mathrm{s}}, \tag{3.27}$$

$$\vec{E}^{\tan} \times \vec{n} = 0, \tag{3.28}$$

can be written [52] (p. 62). The auxiliary vector potential based general field equation (3.11) can then be written as

$$\vec{E} = -j\omega\vec{\mathrm{A}} - j\frac{1}{\omega\mu\varepsilon}\nabla\left(\nabla\cdot\vec{\mathrm{A}}\right). \tag{3.29}$$

Inserting the solution for the auxiliary vector potential wave equation (3.12) to (3.29) and applying vector identities (3.19), (3.20) and (3.23), the EFIE for a PEC-structure can be written to

$$\vec{E}^{\mathrm{s}} = -\frac{1}{4\pi}\iint\limits_{S}\left[j\omega\mu\vec{J}_{\mathrm{s}}\mathrm{G} + j\frac{1}{\omega\varepsilon}\left(\nabla'\cdot\vec{J}_{\mathrm{s}}\right)\nabla\mathrm{G}\right]ds'. \tag{3.30}$$

When applying the continuity equation for the electric surface charge density (3.5),

$$\rho_s = -\frac{1}{j\omega}\,\nabla\cdot\vec{J}_s, \tag{3.31}$$

and inserting (3.31) into (3.30), $\vec{E}^s$ can be expressed as

$$\vec{E}^s = -\frac{1}{4\pi}\iint_S \left[\underbrace{j\omega\mu\vec{J}_s\mathrm{G}}_{Contribution\,of\,currents} - \underbrace{\frac{1}{\varepsilon}\rho_s\nabla'\mathrm{G}}_{Contribution\,of\,charges}\right] ds'. \tag{3.32}$$

It can be seen that both electric current density distribution and electric surface charge density distribution over the surface contribute to the scattered field. If we consider wire structures, the surface integral in (3.30) and (3.32) can be reduced to a line integral.

Comparing (3.24) with (3.30), one can see that (3.30) can be transformed to (3.24) when $\vec{J}_s$ is known and $\vec{M}_s = 0$. The formulation (3.30) therefore can be applied to the surface filled with PMC according to the equivalence principle described in the section 3.2 (see Figure 3.3 (b)). In this case, the related formulation (3.32) gives an explanation for the contribution of the charge distribution, when the equivalence principle is applied. This proves that the Huygens principle (the surface equivalence theorem) is applicable for the near-field region, as the contribution of charges is included.

Usually, for a closed surface filled with PMC where $\vec{J}_s$ is known, $\vec{M}_s$ must be retrieved, e.g., by applying FEM [36]. However, if the defined surface is an infinite large plane which is closed in the infinite and is filled with PEC (see Figure 3.4), the known $\vec{J}_s$ should be doubled, and there is no need to retrieve $\vec{M}_s$. But still, the charge distribution is already considered. It is just not so obvious to be seen. A similar derivation is also applicable for a surface filled with PEC, where $\vec{M}_s$ is known and $\vec{J}_s = 0$. Here, it should be noted that the rule described in Figure 3.4 gives an example for the usage of $\vec{M}_s$. The rule is also applicable for $\vec{J}_s$, when the infinite large plane is closed in the infinite and is filled with PMC.

The formulation (3.32) is often introduced for metallic structures but expressed by a sum of the contribution of a vector potential and a scalar potential, which can be obtained by introducing the so-called Lorenz condition

$$\nabla\cdot\vec{\mathrm{A}} = -j\omega\mu\varepsilon\Phi. \tag{3.33}$$

By inserting (3.33) into (3.29), one obtains:

$$\vec{E}^s = -j\omega\vec{\mathrm{A}} - \nabla\Phi. \tag{3.34}$$

Φ is the electric scalar potential, which can be expressed by [53] (p. 16), or [54] (p. 31)

$$\Phi = \frac{1}{4\pi\varepsilon} \iint\limits_{S} \rho_{\mathrm{s}} \mathrm{G} ds'. \tag{3.35}$$

If using the solution for the inhomogeneous vector potential wave equation (3.12)-(3.13) and the electric scalar potential (3.35), one can obtain that the formulation (3.34) equals (3.32).

As in this dissertation, in most cases, “thin-wire” structures were used. The surface integral in (3.32) is reduced to a line integral [53] (p. 16). Here, the definition of the “thin-wire” approximation for the wire structures requires: (1) the wire length l >> wire radius r_{w}; (2) r_{w} << λ (the related wave length). The “thin-wire” approximation restricts the current flow along the wire structure concentrated in the axis. In this work, the “thin-wire” approximation was applied to all considered wire structures. Supposing a *z*-aligned straight “thin-wire” has the length l, $\vec{E}^{s}$ is then a line integral over the wire length l. The integral (3.32) can be written as [53] (p. 18)

$$\vec{E}^{\mathrm{s}} = -\frac{j\omega\mu}{4\pi} \int\limits_{l} I(z')\mathrm{G}(\vec{r},\vec{r}')\, dz' - \frac{j}{4\pi\omega\varepsilon} \int\limits_{l} \frac{dI(z')}{dz'} \nabla' \mathrm{G}(\vec{r},\vec{r}')\, dz'. \tag{3.36}$$

The related line charge density ρ_{l} can be expressed as

$$\rho_{\mathrm{l}}(z') = -\frac{1}{j\omega} \frac{dI(z')}{dz'}. \tag{3.37}$$

Inserting (3.37) into (3.36) gives:

$$\vec{E}^{\mathrm{s}} = -\frac{j\omega\mu}{4\pi} \int\limits_{l} I(z')\mathrm{G}(\vec{r},\vec{r}')dz' - \frac{1}{4\pi\varepsilon} \int\limits_{l} \rho_{\mathrm{l}}(z') \nabla' \mathrm{G}(\vec{r},\vec{r}')dz'. \tag{3.38}$$

From (3.32), it can be found that the electric field can be expressed by the contribution of currents and line charge densities over the involved metallic structure. Equation (3.32) can be used for calculating the electric field if field sources (currents and charges) are known. It should be noted that the scattered fields/incident fields are introduced only for the derivation of EFIE. In later sections/chapters of this work, the electric field, generated from equivalent current sources (by applying surface equivalence theorem) or wire currents (common-mode currents from CISPR 25 structures), will be discussed.

3.5 Numerical Treatment of Electric Field Integral Equation (EFIE)

In this work, the fields have to be calculated from a given current distribution. This can be done with the EFIE. In this equation, a function for the current distribution is needed. As for complex structures, an analytic representation for this function cannot be found, numerical techniques are needed. For the treatment of an arbitrary current distribution, methods from the numerical technique - **m**ethod **o**f **m**oments (MoM) (e.g. described in [55],[56],[57]) can be used. Here an unknown current distribution can be found based on given boundary conditions using the EFIE. The unknown current distribution in MoM is represented by a set of so-called basis functions that must be defined prior. The task of an unknown current distribution calculation is then reduced to finding weights of the known basis functions. For MoM also different techniques for field computation in space from arbitrary current distributions were developed. In this work, especially these techniques will be used intensively.

Commonly used techniques apply subdomain-basis functions that are valid only for a part of the current carrying structure. This work mainly considers wire and surface structures; therefore, the basis functions for these structures will be introduced. Surface structures are required for the defined Huygens' surface. Here, the "roof-top" basis functions [58],[59], will be applied. For a wire structure, triangular basis functions [53] (p. 29) will be used. Both kinds of basis functions for current distribution will be discussed in the next sections. It will be shown how fields can be computed from the currents.

3.5.1 Numerical Treatment of Surface Structures

A Huygens' surface can be defined by a set of discrete points, sufficiently close to each other. The electric and magnetic fields over the surface can be found, e.g., with field probes. From the fields the equivalent electric and magnetic sources $\vec{J}_{\mathrm{eq}}$ and $\vec{M}_{\mathrm{eq}}$ can be calculated. Equivalent currents and surface geometry can be used in integral (3.24). The integral must be treated numerically. In this section, the integration process is explained by defining a closed Huygens' surface that is composed of six plane surfaces, as it is a general integral process. Later, the integral of one large surface will be used. This closed surface is also called Huygens' box [60] and is located in the Cartesian coordinates system, as shown in Figure 3.5. Flat rectangular patches are applied to discretize all six sides of the surfaces of the box. As an example, rectangular patches on plane 2 and plane 3 are illustrated in the figure. At the observation point $P(x, y, z)$ the field outside of the Huygens' box should be calculated. In the figure, the equivalent current sources $\vec{J}_{\mathrm{eq}}$ and $\vec{M}_{\mathrm{eq}}$ at one source point over one patch are shown by different colors. R represents the distance between the field observation point and the source point on Huygens' box whereas $\vec{Q}$ is an arbitrary inner point inside the Huygens' box, which can be used to determine the normal direction ($\vec{n}$) of the surface.

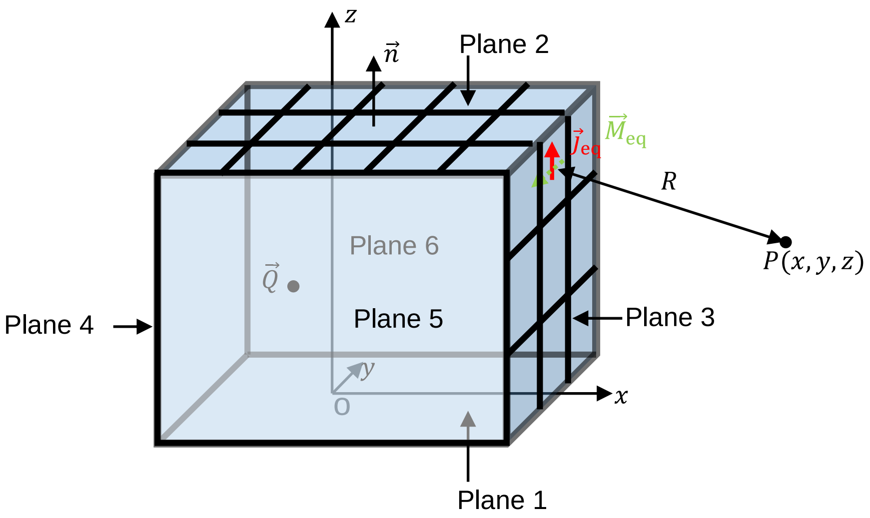

Figure 3.5: A closed Huygens' box with six sides and rectangular discretization.

In this subsection, the numerical treatment of the EFIE for a surface structure will be described with the following steps:

Step 1: The "roof-top" basis functions are defined, and the surface current densities/charge densities will be expressed with the help of these basis functions and surface currents.

Step 2: From known electric and magnetic fields, equivalent surface currents can be found. The way how to handle the currents over each surface patch is described.

Step1:

The "roof-top'' basis function has already been described for example, in [61] or [62]. It is illustrated in Figure 3.6. To express one basis function, the subfigure (a) shows two adjacent rectangular patches (patch 1 and 2) with a common edge. An electric current I (in case of surface equivalence theorem I is an equivalent electric current) flows from patch 1 to patch 2 (parallel to the *x*-axis). The basis function for the common edge of patch 1 is given by, e.g., [62] (pp. 41-43):

$$\vec{J}_{\mathrm{sb}} = \frac{I}{\Delta y} \frac{x}{x_1} \vec{e}_x = \frac{I}{\Delta S_1} x \, \vec{e}_x, \tag{3.39}$$

where $\Delta S_1 (= \Delta y \cdot x_1)$ is the area of patch 1. From the figure, when x reaches x_1, $\vec{J}_{\mathrm{sb}}$ has the maximal value of $\frac{I}{\Delta y}$. Typically, the unit of I is [A], and the unit of $\vec{J}_{\mathrm{sb}}$ is [A/m]. Hence, the physical meaning of $\vec{J}_{\mathrm{sb}}$ is the electric current density of the surface patches. $\vec{M}_{\mathrm{sb}}$ can be similarly defined, which gives the magnetic current density of surface patches based on the magnetic current across the common edge.

According to the continuity equation given in (3.5), the divergence of the surface electric current density $\vec{J}_{\mathrm{sb}}$ gives the surface charge density written as:

$$\nabla \cdot \vec{J}_{\mathrm{sb}} = \frac{I}{\Delta S_1}. \tag{3.40}$$

The charge density is a constant over a part of the basis function, as illustrated in figure (b). The sign of the charge depends on the direction of the current flow.

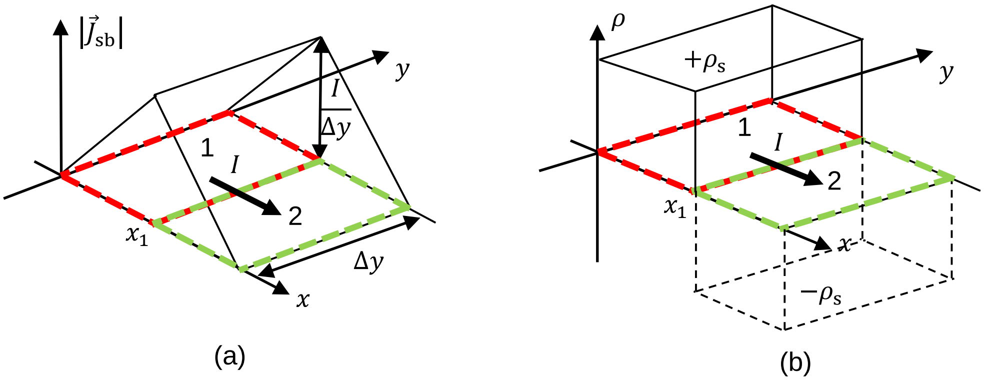

Figure 3.6: Current basis function and charge distribution for rectangular patches, (a) roof-top function straddling two square cells [62], where the vector direction by an arrow indicates the current direction, (b) charge density, represented as constant blocks.

Figure 3.7 (a) illustrates one surface patch with four vertexes, denoted as $\vec{V}_1, \vec{V}_2, \vec{V}_3$, and $\vec{V}_4$. The four formed edges from the vertexes are denoted as $\vec{v}_1, \vec{v}_2, \vec{v}_3$, and $\vec{v}_4$. The centroid of the patch ($\vec{S}$) can be calculated by:

$$\vec{S} = \frac{1}{4}(\vec{V}_1 + \vec{V}_2 + \vec{V}_3 + \vec{V}_4). \tag{3.41}$$

Figure 3.7 (b) illustrates four electric currents (I_1, I_2, I_3, I_4) flowing out of the patch given in Figure 3.6 (a). In this case, the electric surface current density $\vec{J}_s$ and surface charge density ($\nabla \cdot \vec{J}_s$) can be expressed respectively as:

$$\vec{J}_s = \frac{I_1}{\Delta S}(x - x_1)\vec{e}_x + \frac{I_2}{\Delta S}(y - y_1)\vec{e}_y + \frac{I_3}{\Delta S}(x_2 - x)\vec{e}_x + \frac{I_4}{\Delta S}(y_2 - y)\vec{e}_y, \tag{3.42}$$

$$\nabla \cdot \vec{J}_s = \frac{1}{\Delta S}(I_1 + I_2 + I_3 + I_4), \tag{3.43}$$

where $\Delta S = (y_2 - y_1)(x_2 - x_1)$ is the area of the patch.

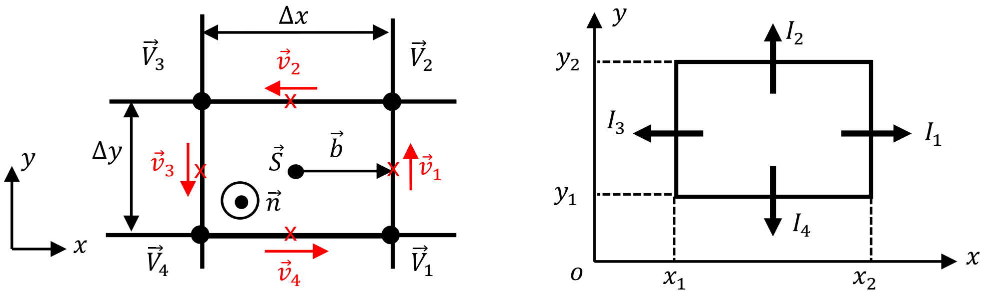

(a) (b)

Figure 3.7: Definition of the rectangular patch and the surface current densities. (a) description of the patch, (b) four currents are flowing out of the patch.

Step 2:

According to Huygens principle, both electric current (I_J) and magnetic current (I_M) exist at the same time. In general, the magnitude of currents flowing into/out of one edge can be determined by [61] (pp. 98-99):

$$I_\mathrm{J} = \left|\vec{v} \cdot \vec{H}\right|, \tag{3.44}$$

$$I_\mathrm{M} = \left|\vec{v} \cdot \vec{E}\right|, \tag{3.45}$$

where $\vec{H}$ and $\vec{E}$ are the fields at the center of the corresponding edge. The fields will be considered as known parameters, which can be captured with field probes in a measurement. For the patch in the Figure 3.7 (a), the positions of the edge centers are marked by the red cross and $\vec{v}$ represents the edge vector.

By inserting (3.44) for each edge of the patch defined in Figure 3.7 (b) to the expressions (3.42), (3.43) respectively, the surface electric current density $\vec{J}_\mathrm{s}$ and surface charge density $(\nabla \cdot \vec{J}_\mathrm{s})$ can be expressed:

$$\vec{J}_\mathrm{s} = \frac{I_{J_1}}{\Delta S}(x - x_1)\vec{e}_x + \frac{I_{J_2}}{\Delta S}(y - y_1)\vec{e}_y + \frac{I_{J_3}}{\Delta S}(x_2 - x)\vec{e}_x + \frac{I_{J_4}}{\Delta S}(y_2 - y)\vec{e}_y, \tag{3.46}$$

$$\nabla \cdot \vec{J}_s = \frac{1}{\Delta S}\left(I_{J_1} + I_{J_2} + I_{J_3} + I_{J_4}\right). \tag{3.47}$$

If inserting (3.45) to a defined magnetic current density $\vec{M}_\mathrm{s}$, surface current density $\vec{J}_\mathrm{s}$ and surface charge density $(\nabla \cdot \vec{J}_\mathrm{s})$ for a patch can be expressed generally as:

$$\vec{M}_\mathrm{s} = \frac{I_{M_1}}{\Delta S}(x - x_1)\vec{e}_x + \frac{I_{M_2}}{\Delta S}(y - y_1)\vec{e}_y + \frac{I_{M_3}}{\Delta S}(x_2 - x)\vec{e}_x + \frac{I_{M_4}}{\Delta S}(y_2 - y)\vec{e}_y, \tag{3.48}$$

$$\nabla \cdot \vec{M}_\mathrm{s} = \frac{1}{\Delta S}\left(I_{M_1} + I_{M_2} + I_{M_3} + I_{M_4}\right). \tag{3.49}$$

In equations (3.46)-(3.49), it is important to determine the current directions correctly. Figure 3.8 demonstrates an example of current flow over patch 1 (as described in [62]

(p. 42)). The currents I_1, I_2 flow out of the patch in positive direction, whereas the currents I_3, I_4 flow into the patch in negative direction. For patch 2, I_1 is negative, as the current flows into the patch.

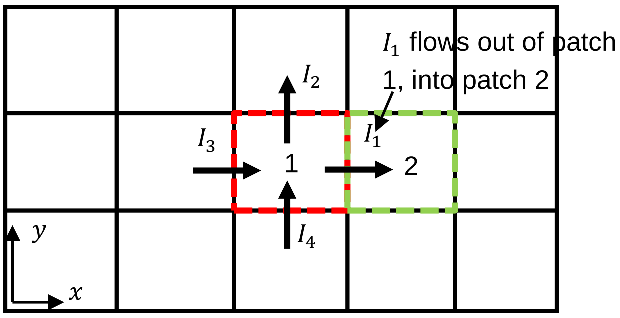

Figure 3.8: Superposition of four current basis functions for patch 1 [62] (p. 42).

The method to determine the current direction is described in [61] and [62]. Here, it is shortly presented in Appendix B.

The “roof-top” basis function $\vec{J}_{\mathrm{sb}}$ (see (3.40)) introduced in section 3.5.1 describes only the electric current flowing out of one common edge along the x-axis. For all four edges of the patch in the xy-plane, $\vec{J}_{\mathrm{s}}$ (see (3.42)) gives the electric current density consisting of overlapping basis functions that include both for x- and y- directions. Usually, for a surface structure, two basis functions are required ($\vec{J}_{\mathrm{sx}}$ for x- and $\vec{J}_{\mathrm{sy}}$ for y-direction respectively). In this work, $\vec{J}_{\mathrm{s_n}}(\vec{r}\,')$ is defined as the electric surface current basis function of the n-th patch and can be obtained by the expression (3.46). Similarly, $\vec{M}_{\mathrm{s_n}}(\vec{r}\,')$ is defined as the magnetic surface current basis function of the n-th patch of total N patches.

Using the defined basis functions $\vec{J}_{\mathrm{s_n}}(\vec{r}\,')$ and $\vec{M}_{\mathrm{s_n}}(\vec{r}\,')$, the electric field in the expression (3.24) for equivalent current sources over the Huygens’ surface can be numerically calculated. The surface integration over the patches must be numerically performed, i.e., by a 2D Gaussian integration described in Appendix C.

3.5.2 Numerical Treatment for Thin-Wire Structures

Wire structures are subdivided into a number of segments. Triangular basis function can be used to describe the current distribution along the wire structure.

Figure 3.9 (a) illustrates a triangular basis function $f_n(z')$, that is defined over two z-oriented segments limited by their z-coordinates: one between z_{n-1} and z_n, and the other between z_n and z_{n+1}. Figure 3.9 (b) gives the current at z_n represented by the current basis function, where I_n is the current at z_n.

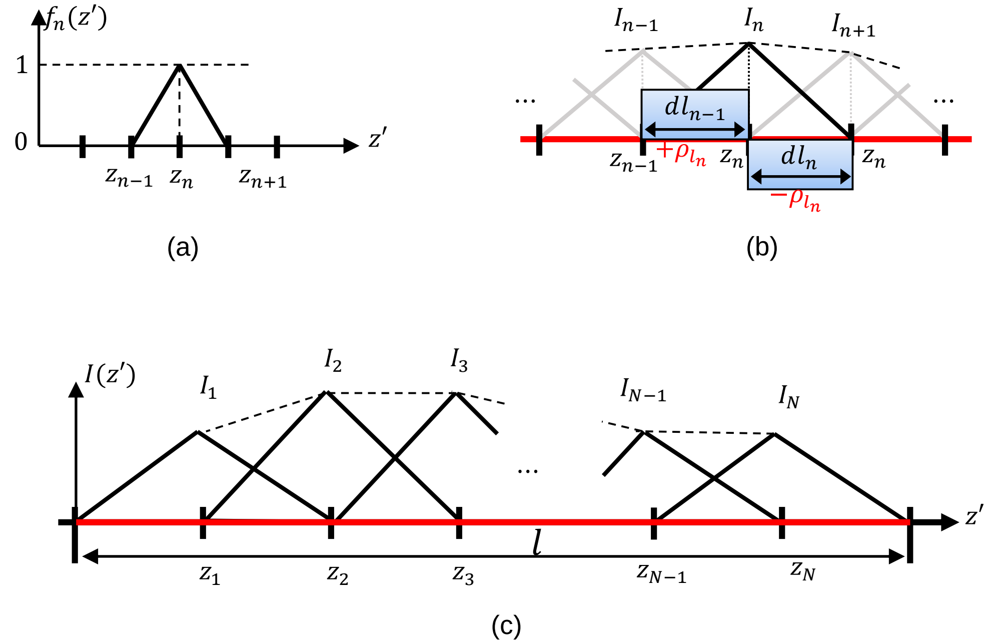

Figure 3.9: Triangular basis functions. (a) one basis function, (b) the current at I_n, (c) N basis functions, with the current distributions over the wire.

The given triangular basis function $f_n(z')$ is only defined inside the two segments, which can be written as [63] (p. 28):

$$f_n(z') = \begin{cases} \dfrac{z' - z_{n-1}}{z_n - z_{n-1}} & \text{for the region:} \quad z_{n-1} \le z' \le z_n, \\[2ex] \dfrac{z_{n+1} - z'}{z_{n+1} - z_n} & \text{for the region:} \quad z_n \le z' \le z_{n+1}, \\[2ex] 0 & \text{other.} \end{cases} \tag{3.50}$$

Based on the defined basis function, the current can be expressed by (e.g., described in [53] (p. 29)):

$$I_n(z') = \begin{cases} I_n \dfrac{z' - z_{n-1}}{z_n - z_{n-1}} & \text{for the region:} \quad z_{n-1} \le z' \le z_n, \\[2ex] I_n \dfrac{z_{n+1} - z'}{z_{n+1} - z_n} & \text{for the region:} \quad z_n \le z' \le z_{n+1}, \\[2ex] 0 & \text{other.} \end{cases} \tag{3.51}$$

The charge density over the wire segment between z_{n-1} and z_n and the segment between z_n and z_{n+1} can be obtained by inserting (3.51) into (3.37), as written in [53], as:

$$\rho_{l_n} = \begin{cases} \dfrac{j}{\omega} \dfrac{I_n}{dl_{n-1}} & \text{for the rising edge from } z_{n-1} \text{ to } z_n, \\[2ex] -\dfrac{j}{\omega} \dfrac{I_n}{dl_n} & \text{for the falling edge from } z_n \text{ to } z_{n+1}, \end{cases} \tag{3.52}$$

where $dl_{n-1} = z_n - z_{n-1}$ and $dl_n = z_{n+1} - z_n$. A constant charge block exists for a given frequency ω. Figure 3.9 (c) gives the total number N of triangular basis functions for a wire of length l, where $I_1, I_2, I_3, \cdots, I_{N-1,} I_N$ are the current weights for the triangular basis function. The current function for the wire can be written as a sum:

$$I(z') = \sum_{n=1}^{N} I_n f_n(z'). \tag{3.53}$$

Note, here the current is zero at both ends; therefore, no additional basis functions are needed for the beginning and the end of the wire. Depending on the physical configuration of a structure, the basis function may need correction at the ends of a wire, as discussed in [53]. For a wire connection, an additional triangular basis function with current I_{com} must be introduced to keep a continuous current flow. This will be described in chapter 5, section 5.1.2.3.

The expression (3.53) describes the current distribution along a thin-wire of length l, by the sum of all N current basis functions (see Figure 3.9 (c)). By inserting (3.53) into (3.36), the electric field is obtained:

$$\vec{E} = -\frac{1}{4\pi} \sum_{n=1}^{N} I_n \int_{\Delta l} j\omega\mu f_n(z') \mathrm{G}(\vec{r}, \vec{r}') dz' - \frac{j}{4\pi\omega\varepsilon} \sum_{n=1}^{N} I_n \int_{\Delta l} \frac{df_n(z')}{dz'} \frac{\partial \mathrm{G}(\vec{r}, \vec{r}')}{\partial z} dz'. \tag{3.54}$$

Δl is the length of the segment n. The integral in (3.54) is a 1D integral, which can be numerically integrated. This can be done, e.g., by Gaussian integration, which is shown in Appendix C.

3.6 Electric Field of a Hertzian Dipole

In the previous section, the EFIE was discussed as a method for the calculation of the electric field in free space generated from a current carrying structure. Another method for calculating the field from a known current distribution along a wire is the MDM method. This method is used in this work too. The MDM is based on the theory of a Hertzian dipole (e.g., described in [2], (pp. 422-426) or [12], (pp. 215-226)). The theory is shortly summarized in this section.

In MDM, the basic electric radiating element is an infinitesimally short electric dipole. The emission of wire structures can be calculated by subdividing the wire into very short segments and treating the radiation of each segment by a Hertzian dipole with the length of the segment. This method can be applied to a cable bundle structure in CISPR 25 measurement setups. The total electric field is the sum of electric fields generated from all dipoles.

For an accurate calculation three conditions must be fulfilled: (1) the length dl must satisfy the condition $dl \ll \lambda$; (2) $r_{\mathrm{w}} \ll \lambda$, where r_{w} is the radius of the wire and λ is the wavelength; (3) the distance from dipole to the point of observation should be much larger than dl.

An infinitesimal dipole in free space of length dl carrying a phasor current $I = I_0\vec{e}_z$ is shown in Figure 3.10. The dipole is located at the origin of the Cartesian coordinate system and orientated along the z-axis. The arrow indicates the positive direction of the current flow and the orientation of the dipole. The current density of the dipole at the location $\vec{r}_O$ can be described by introducing the Dirac delta function, which can be written as [12]:

$$\vec{J}_s(\vec{r}') = I_0 dl \delta(\vec{r}' - \vec{r}_O)\vec{e}_z, \tag{3.55}$$

where δ is the Dirac delta function, expressed as:

$$\delta(\vec{r}' - \vec{r}_O) = \begin{cases} 0, & \vec{r}' \neq \vec{r}_O \\ \to \infty, & \vec{r}' = \vec{r}_O \end{cases}. \tag{3.56}$$

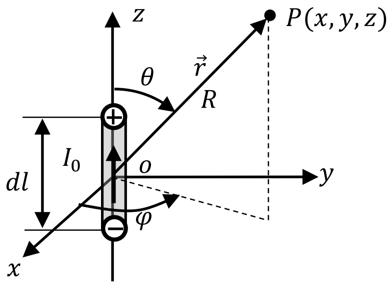

Figure 3.10: An infinitesimal dipole having length dl in the origin of the Cartesian coordinates.

Recalling the expression (3.12) related to the infinitesimal dipole, the magnetic vector potential $\vec{A}$ can be written as:

$$\vec{\mathrm{A}} = \frac{\mu_0 I_0 dl}{4\pi}\frac{\mathrm{e}^{-jk_0R}}{R}\vec{e}_z. \tag{3.57}$$

The radiated fields at an observation point P are usually given in spherical coordinates [2], using the orthogonal unit vectors $\vec{e}_r$, $\vec{e}_\theta$, and $\vec{e}_\varphi$. Applying transformation rules the components of the magnetic and electric fields can be written as [2] (pp. 422-423):

$$\vec{H}_r = \vec{H}_\theta = 0, \tag{3.58}$$

$$\vec{H}_\varphi = \frac{jk_0 I_0 dl}{4\pi R}\sin\theta\left(1 + \frac{1}{jk_0R}\right)\mathrm{e}^{-jk_0R}\vec{e}_\varphi, \tag{3.59}$$

$$\vec{E}_\theta = j\eta_0 \frac{k_0 I_0 dl}{4\pi R}\sin\theta\left(1+\frac{1}{jk_0R}-\frac{1}{(k_0R)^2}\right)\mathrm{e}^{-jk_0R}\vec{e}_\theta, \tag{3.60}$$

$$\vec{E}_r = \eta_0 \frac{I_0 dl}{2\pi R^2}\cos\theta\left(1+\frac{1}{jk_0R}\right)\mathrm{e}^{-jk_0R}\vec{e}_r, \tag{3.61}$$

$$\vec{E}_\varphi = 0. \tag{3.62}$$

where:

R the distance between the dipole center and the observation point P;

η_0 the intrinsic impedance of vacuum, $\eta_0 = \sqrt{\mu_0/\varepsilon_0} \approx 377\ \Omega$;

k_0 the wave number in vacuum, $k_0 = \omega\sqrt{\mu_0\varepsilon_0}$.

Now, some characteristics of the field regions will be discussed by analyzing the expressions (3.59)-(3.61).

Looking at electric fields for a large distance R ($R \gg \lambda$), the point of observation can be considered to be in the far-field region. The reason is that $\vec{E}_r$ is inversely proportional to R^2, whereas $\vec{E}_\theta$ is inversely proportional to R. $\vec{E}_r$ is much smaller than $\vec{E}_\theta$. By neglecting $\vec{E}_r$, the far fields can be obtained by considering only the first term of (3.59) and (3.60) respectively [51] (p.159):

$$\vec{H}_{\varphi_{ff}} = jk_0 \frac{I_0 dl}{4\pi}\frac{\mathrm{e}^{-jkR}}{R}\sin\theta\vec{e}_\varphi, \tag{3.63}$$

$$\vec{E}_{\theta_{ff}} = \eta_0 jk_0 \frac{I_0 dl}{4\pi}\frac{\mathrm{e}^{-jk_0R}}{R}\sin\theta = j\omega\mu_0 \frac{I_0 dl}{4\pi}\frac{\mathrm{e}^{-jk_0R}}{R}\sin\theta\vec{e}_\theta. \tag{3.64}$$

$\vec{E}_{\theta_{ff}}$ and $\vec{H}_{\varphi_{ff}}$ are orthogonal, and the ratio of $\vec{E}_{\theta_{ff}}/\vec{H}_{\varphi_{ff}}$ is $\eta_0 \approx$ (377 Ω for free-space). (3.64) contains (3.57) and can be expressed in terms of the vector potential. In the far-field region the vertical component of the electric field ($\vec{E}_z$) can be obtained when $\theta = 90°$ by:

$$\vec{E}_z = -j\omega\vec{\mathrm{A}}\sin\theta|_{\theta=90°} = -j\omega\vec{\mathrm{A}}. \tag{3.65}$$

Therefore, in the far-field, the vertical electric field depends on the magnetic vector potential $\vec{A}$.

The near-field region is defined by $R \ll \lambda$. The magnetic field is dominated by the second term of (3.59), which can be expressed by [51] (p.158):

$$\vec{H}_{\varphi_{nf}} = \frac{I_0 dl}{4\pi R^2} \mathrm{e}^{-jk_0 R} \sin\theta \vec{e}_{\varphi}. \tag{3.66}$$

The electric fields from (3.60) and (3.61) can be approximated by firstly neglecting the first term as:

$$\vec{E}_{\theta_{nf}} = j\eta_0 \frac{I_0 dl}{4\pi R} \left(\frac{1}{jk_0 R} - \frac{1}{(k_0 R)^2} \right) \mathrm{e}^{-jk_0 R} \sin\theta \vec{e}_{\theta.} \tag{3.67}$$

$$\vec{E}_{r_{nf}} = \eta_0 \frac{I_0 dl}{2\pi R^2} \left(1 + \frac{1}{jk_0 R} \right) \mathrm{e}^{-jk_0 R} \cos\theta \vec{e}_r. \tag{3.68}$$

For a very small distance R, the term with $1/R^3$ dominates, (3.67) and (3.68) can be again simplified to have only the term with $1/R^3$, as:

$$\vec{E}_{\theta_{nf}} = \frac{1}{j\omega} \frac{I_0 dl}{4\pi \varepsilon_0 R^3} \mathrm{e}^{-jk_0 R} \sin\theta \vec{e}_{\theta}, \tag{3.69}$$

$$\vec{E}_{r_{nf}} = \frac{1}{j\omega} \frac{I_0 dl}{2\pi \varepsilon_0 R^3} \mathrm{e}^{-jk_0 R} \cos\theta \vec{e}_r. \tag{3.70}$$

In the near-field region, electric and magnetic fields are independent. This is important when analyzing later (in chapter 4) near-field coupling mechanisms in the CISPR 25 measurement setup.

3.7 Electric Field of a Static Dipole

The expressions (3.69) and (3.70) describe the electric field in the near-field region, where a frequency-dependent factor $\frac{1}{j\omega}$ is contained. Especially for low frequencies this them tends to become very large. Therefore, in measurement-based methods the dipole moment I_0 needs to be measured very precisely. In this section, we discuss the static dipole to overcome this issue, which has a length of $2h$ and charge Q, as shown in Figure 3.11. The electric field can be calculated with:

$$\vec{E}_{\theta} = \frac{2hQ}{4\pi \varepsilon_0 R^3} \sin\theta \vec{e}_{\theta}, \tag{3.71}$$

$$\vec{E}_r = \frac{2hQ}{2\pi \varepsilon_0 R^3} \cos\theta \vec{e}_r, \tag{3.72}$$

where R is the distance between the center of the dipole and the field observation point. The calculation in the Cartesian coordinates can also be found in [14].

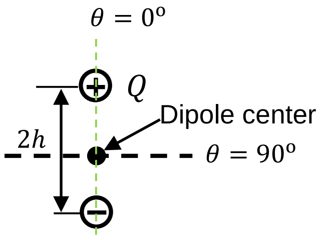

Figure 3.11: Static dipole above ground, where a negative image charge considers the ground influence.

The expressions (3.71) and (3.72) of the static dipole can be compared with (3.69) and (3.70). Without considering the time dependency e^{-jk_0R}, the difference between the expressions is only the factor $\frac{1}{j\omega}$. The factor $\frac{1}{j\omega}$ results from the time integral of the current I:

$$\int I dt = Q \quad \rightarrow \quad I = j\omega Q. \tag{3.73}$$

3.8 Image Theory

The image theory is often applied for electric/magnetic sources placed close to an infinite conducting plane, for example, in [2],[13], and can be a good approximation also for parts of CISPR setups. In those setups, a large metal plate is used (see Figure 1.2), which can be considered approximately as PEC. In this work, electric and magnetic sources close to a PEC are applied, as illustrated in Figure 3.12. The Subfigure (a) shows an electric source with black color (e.g., electric dipole or electric current) in the horizontal and vertical direction, respectively. The gray image sources consider the influence of PEC. Similarly, subfigure (b) shows the images of a magnetic source (e.g., magnetic current) in horizontal and vertical directions.

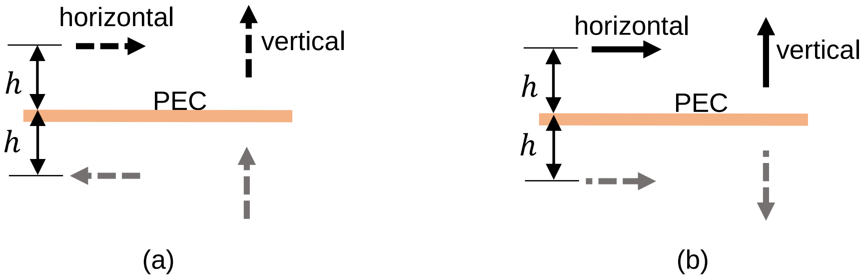

(a)

(b)

Figure 3.12: Electric and magnetic sources and their images close to a PEC. (a) electric sources, (b) magnetic sources.

4 Analysis of the Standard CISPR 25 Measurement Setup

Before introducing the proposed new methods, one should understand the characteristics of the standard measurement setup. For example, the typical field sources, the dominant coupling mechanisms, and the rod antenna characteristics.

Most important in the considered setup is the field coupling between the cable bundle and rod antenna. Therefore, in this chapter, the cable structure will be analyzed with the help of the transmission line theory. The voltage and current distribution, as the root cause for the fields, caused by different load impedance conditions will be analyzed. Since the rod antenna is in the near-field region of the cable structure for the relevant frequencies, the near-field couplings and feedback effects between the rod antenna and cable structure, as well as the rod antenna characteristics, will be described and analyzed in detail. Furthermore, the influence of the metallic table, the metallic chamber floor, and the connections between the metallic table and the chamber floor will be discussed. Possible resonances will be investigated with the help of numerical MoM simulations.

First, the applied field analysis methods are depicted. Second, the CISPR 25 measurement setup is analyzed regarding the critical points mentioned above.

4.1 Calculation Methods for Setup Analysis

Both analytical and numerical methods can be applied separately or combined to calculate the electric field from CISPR 25 measurement setups. Here, analytical and numerical methods were combined, as illustrated in Figure 4.1. The analytical method (top of the left path) provides the currents and voltages over a cable bundle. The cable bundle can be handled by using the **m**ulticonductor **t**ransmission **l**ine (MTL) theory, e.g., [26]. As the application of MTL theory is complex and results can be less intuitive, here it is assumed that the cable bundle can be substituted by a single-wire cable carrying the common-mode currents. Such simplifications are commonly used, e.g., in [15],[21],[64], to reduce the computational efforts. The common-mode current distribution can be used in the EFIE for the numerical computation of the near- and far-fields. Alternatively, an MDM model with a sufficient number of dipoles can be parameterized with the common-mode currents for near- and far-field calculation.

As the cable is often the dominant but not the only structure responsible for field generation, more powerful and flexible analysis methods can be useful for validation of the methods given in the left path in Figure 4.1. Field simulation programs (the right path in Figure 4.1) provides computational methods for even complex geometries and materials. As powerful programs are very expensive for commercial applications and thus often not available in the industry, such programs cannot substitute the approach shown in the left path in Figure 4.1.

Several programs for time and frequency domain are available such as CST Microwave Studio [65], FEKO [66], or CONCEPT-II [67]. In this work, the frequency domain program CONCEPT-II [67] has been used. CONCEPT-II is based on the EFIE that is formulated for wires, surfaces, and voluminous structures. The discretized EFIE is solved with the help of the MoM, e.g., [55]. One might wonder why a full-wave field simulation program is involved since this work focuses on low frequency problems. This will be explained in section 4.1.2.

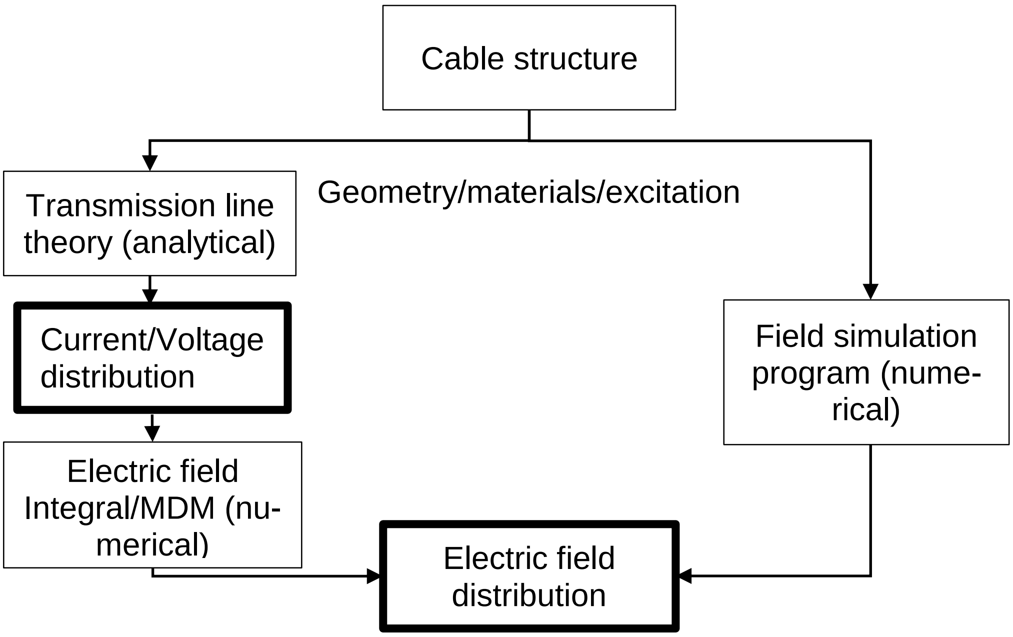

Figure 4.1: Field calculation methods for cable structures.

4.1.1 Analytical Methods

Analytical methods can be helpful for simple structures. In this work, the electric currents and voltages along a single-wire cable are calculated using the transmission line theory (described in section 4.2.3). The needed per-unit length parameters are obtained analytically as a homogeneous cable structure can be assumed. The influence of different terminations is analyzed. The calculated current distribution along the cable can be used in the EFIE or the MDM method for field calculation. As the EFIE becomes quite complex and the superposition of a large number of dipole fields is necessary, the fields have to calculated with numerical methods.

4.1.2 Numerical Methods - CONCEPT-II

Most commercial computer simulation programs for electromagnetic field analysis have many important features to analyze large and complex geometries with more or less arbitrary excitations. For many field problems, the computational time is not the main issue. Often, most time consuming is the modeling process. Here, most commercial programs contain powerful functions for a fast model generation with the help of an easy to use graphical user interface. Such user interfaces require much programming time, and development costs are very high. Solver programming can be challenging, but in general, it is not a time-consuming process. Therefore, it might be the reason why most field simulation programs have no solver limitations and can handle the full set of Maxwell’s equations. As only electrical large structures (which means the physical size of the structure is much larger compared with related wavelength) require the solution of the full set of Maxwell’s equations, so-called full-wave solvers are not needed here. In this work, the considered frequency range is below 30 MHz. The standard CISPR 25 setups can be regarded as electrically small. Quasi-static or static solvers should be sufficient for the needs of this thesis. The underlying equations could be simpler.

There are some quasi-static or static solvers available. However, the known programs are very basic and not very user-friendly. The modeling process can become extremely time-consuming or even fail for complex geometries. Solvers for resulting equations systems are often not optimized and cannot handle modern multi-core processor architectures. The underlying potentials due to the simple mathematical formulations regarding a faster calculation are not used. For example, FastHenry2 [68] or FastCap [69] are static solvers, which are capable of computing the self- and mutual-inductances, capacitances, and resistances of a 3D structure. The simulation model geometry has to be defined by text files, and there are many limitations in this process. The main core of the programs was written in the 80th. There were no significant optimizations since release. From the calculated capacitances, inductances, and resistances, an equivalent circuit has to be generated that might be ambiguous and error-prone. Most full-wave field computation programs provide reliable solutions with powerful user interfaces for pre- and post-processing not only for high frequencies but also for low frequencies, and highly optimized computational cores. There are no alternatives to such programs regarding modeling and computation speed.

Here, the used commercial full-wave field simulation program CONCEPT-II is based on the solution of EFIE. The numerical MoM-approach requires a discretization of the sources of the electromagnetic fields. The scalar potential term is predominant at very low frequencies and must be calculated from the current gradient (3.37), which is difficult to obtain at low frequencies. A wire structure is discretized into current segments. At very low frequencies, the calculated currents show only tiny differences, and the precision of the calculation limits the accuracy. In CONCEPT-II, the low frequency problem has been investigated intensively, and solutions were found. In [62] (pp. 86-89), it is described how the impedance matrix is created to give stable and accurate solutions. The developers of CONCEPT-II in [70] pointed out that for the classical MoM, this low frequency limit depends on the geometrical size of the structure and is somewhere in the range of 50 Hz to 1 kHz.

4.2 Characterization of the Test Cable Structure

4.2.1 A Simplified Substitution Model for a Cable Bundle

The cable bundle in the CISPR 25 setup can be calculated using the MTL theory [26]. As parameterization can be complex and all sources and terminations are often not known or very difficult to be found. In this work, common-mode voltages/currents and charges are considered as the root cause of emission problems. This approach is in line with other investigations regarding the cable bundle in EMC [16]. A simplified substitution model consisting of a single-wire cable is therefore introduced to replace the cable bundle under investigation. The single substitution cable used here carries only the common-mode currents.

The configuration of the single-wire cable structure is shown in Figure 4.2. The cable is above the conducting table (simplified as an infinite PEC ground plane) at height h, and the table forms the signal return path. The cable length is l, and it is parallel to the *x*-axis. The disturbance source is represented by a Thevenin's source [56] consisting V_S and Z_S. The cable is terminated by a load impedance Z_L. In the next section, the transmission line theory will be shortly summarized to calculate voltages and currents along the cable structure.

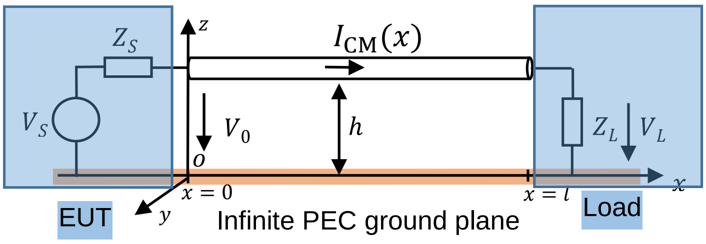

Figure 4.2: A single-wire cable above an infinite PEC ground plane as a common-mode substitution model for a cable bundle.

4.2.2 Transmission Line Theory

When the length of the two-conductor structure is not much shorter than the wavelength of the propagating signals along the conductor structure, the transmission line theory is required for the calculation of spatial and temporal voltage and current distribution. A two-conductor structure can be represented by a circuit model given in Figure 4.3. Here the conductors are subdivided into segments. Each segment has a length of Δl. R', L', G', C' are distributed parameters, defined by per-unit-length values. Specifically, $L'$and C' are distributed inductance and distributed capacitances; R' represents the conductor loss and G' represents losses in the dielectric material separating the conductors.

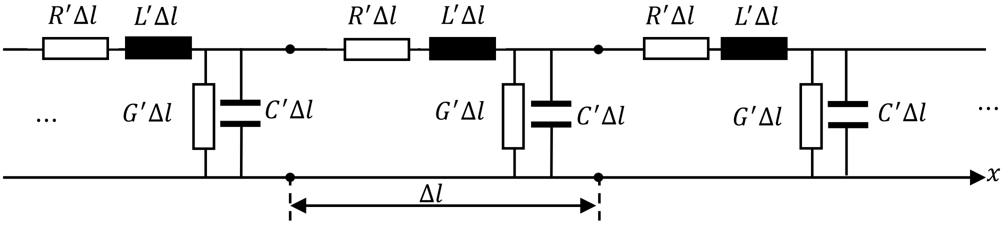

Figure 4.3: Representation of distributed lumped-circuit model of a transmission line.

Transmission line theory can be used to describe a segment circuit of infinitesimal length Δl. The relation between voltage and current along the segment can be expressed by Telegrapher's equations [2], which are given, e.g., in [26] as:

$$\begin{cases} \frac{d}{dx}V(x) = -(R' + j\omega L')I(x) \\ \frac{d}{dx}I(x) = -(G' + j\omega C')V(x) \end{cases}. \tag{4.1}$$

In many cases, especially in short structures, the losses represented by R' and G' can be neglected. The CISPR 25 setup cable structure is short, and losses can be neglected.

L' and C' can easily be calculated for the case of a single circular wire above ground, by [2]:

$$L' = \frac{\mu_0}{2\pi}\cosh^{-1}(h/r_\mathrm{w}), \tag{4.2}$$

$$C' = \frac{2\pi\varepsilon_0}{\cosh^{-1}(h/r_\mathrm{w})}, \tag{4.3}$$

in which $\cosh^{-1}(h/r_\mathrm{w}) = \ln\left[\frac{h}{r_\mathrm{w}} + \sqrt{\left(\frac{h}{r_\mathrm{w}}\right)^2 - 1}\right]$ (r_w is the wire radius). The voltage $V(x)$ and current $I(x)$ along the transmission line are respectively given by [2]:

$$V(x) = \frac{1 + \Gamma_L \mathrm{e}^{-j2\beta L}\mathrm{e}^{j2\beta x}}{1 - \Gamma_S\Gamma_\mathrm{L}\mathrm{e}^{-j2\beta L}} \frac{Z_C}{Z_C + Z_S} V_S \mathrm{e}^{-j\beta x}, \tag{4.4}$$

$$I(x) = \frac{1 - \Gamma_L \mathrm{e}^{-j2\beta L}\mathrm{e}^{j2\beta x}}{1 - \Gamma_S\Gamma_L\mathrm{e}^{-j2\beta L}} \frac{Z_C}{Z_C + Z_S} V_S \mathrm{e}^{-j\beta x}, \tag{4.5}$$

where:

$\beta = \frac{2\pi}{\lambda}$ is the phase constant;

Z_{C} is the characteristic impedance of the homogeneous wire, which can be obtained by

$$Z_C = \sqrt{\frac{L'}{C'}}, \tag{4.6}$$

Γ_{S} is the source reflection coefficient, which can be expressed as

$$\Gamma_S = \frac{Z_S - Z_C}{Z_S + Z_C}, \tag{4.7}$$

and Γ_{L} is the load reflection coefficient, which can be written as

$$\Gamma_L = \frac{Z_L - Z_C}{Z_L + Z_C}. \tag{4.8}$$

4.2.3 Analysis of the Voltage and Current Distribution

Based on transmission line theory, voltage and current distribution over a cable structure can be calculated through the equations (4.4) and (4.5) when the source impedance and load impedance are known. However, impedances within a CISPR 25 measurement setup usually is not a fixed value depending on the kind of equipment. In general, the values are unknown. For the following investigations, a fixed source impedance Z_S (= 50 Ω) is used in order to quantitative investigate the changes in voltage and current distribution caused by varying load impedances. The reason is that a fixed source impedance Z_S is given when an artificial network is involved. In this case, the impedance value of 50 Ω is a good approximation. The characteristic impedance Z_C of the CISPR 25 cable bundle substitution single-wire cable is about 270 Ω.

For the CISPR 25 cable geometry the voltage and current distribution over the cable are calculated now for load impedances of 5 Ω, 50 Ω, 500 Ω, and 5 kΩ. Figure 4.4 depicts the voltage and current distribution at 1 MHz and 10 MHz respectively. The voltages and currents are normalized to the voltage and the current at the beginning of the cable. The figure shows that with the increased frequency (from 1 MHz to 10 MHz), both voltage and current vary significantly along the cable, especially for the mismatched cases.

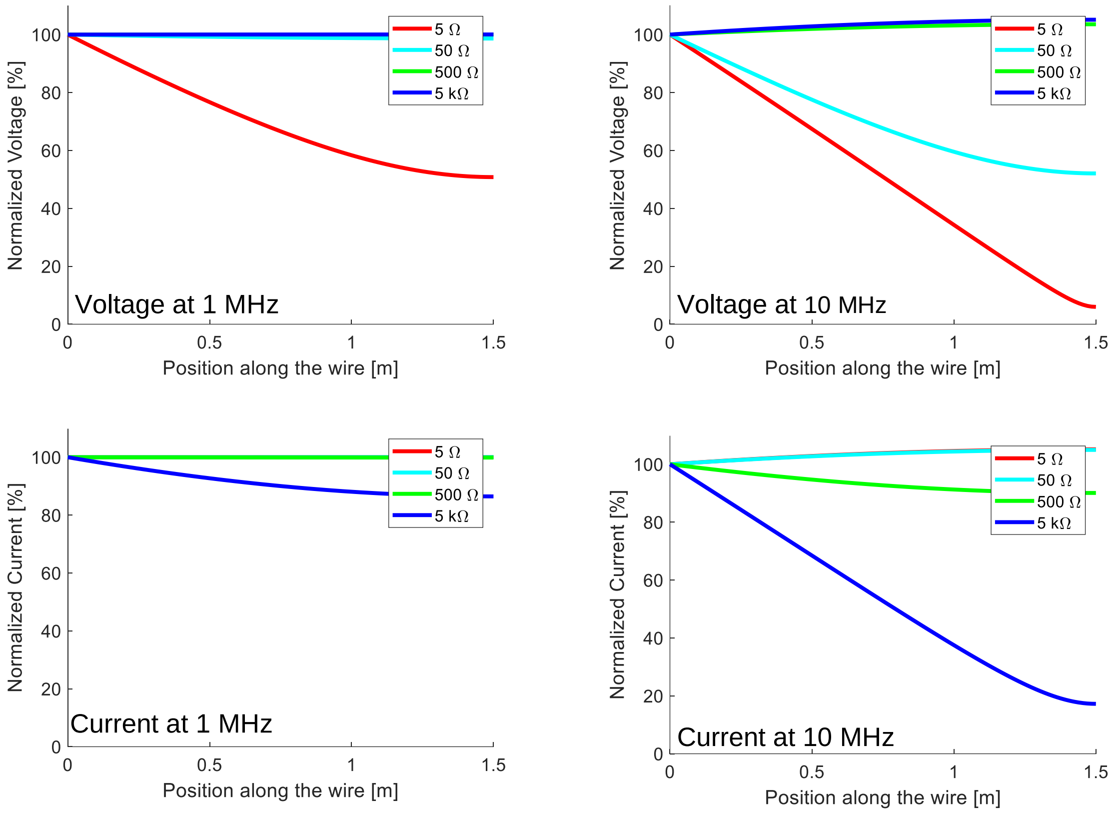

Figure 4.4: Variation of voltage and current distribution for different loads at 1 MHz and 10 MHz.

4.2.4 Dominant Electric Field Sources

Charges are the sources for the electric near-field and can be calculated from a current or voltage distribution along a cable structure. Equation (3.34) contains two terms, in which the vector potential $\vec{\mathrm{A}}$ is linked to the current, and the scalar potential Φ is related to the charge distribution. To analyze the contribution of each term, the setup in Figure 4.2 was used. The analysis was done for a frequency range from 1 kHz up to 200 MHz, as such a large frequency range considers both quasi-static near-field sources that cause non-radiating near fields, and radiating sources at higher frequencies. The parameters of the setup are (Figure 4.2) $h = 5\ \mathrm{cm}$, $V_S = 1\ \mathrm{V}$, $Z_S = 50\ \Omega$, and $Z_L = 50\ \Omega$. The observation point for field calculation is located 1 m away from the cable center, and 10 cm above the conducting plane.

The calculated horizontal component $E_{\mathrm{horizontal}}$ ($= E_x$ in Figure 4.2) (upper figure) and vertical component E_{vertical} $= (E_z$ in Figure 4.2) (bottom figure) of the electric field are given in Figure 4.5. The red curve is directly taken from the MoM simulation as a reference. The blue curve was numerically calculated using the “thin-wire” approximation (3.54) of the electric field integral equation (3.34), where the triangular basis functions from (3.50) are used. For the electric field calculation, one can either use currents calculated by the transmission line theory or exported from CONCEPT-II. Here the currents from CONCEPT-II are used. These currents provide a reference to validate the numerical calculation of the EFIE (3.54). It can be observed that the blue curve matches the red curve from both subfigures, i.e., the calculation is correct.

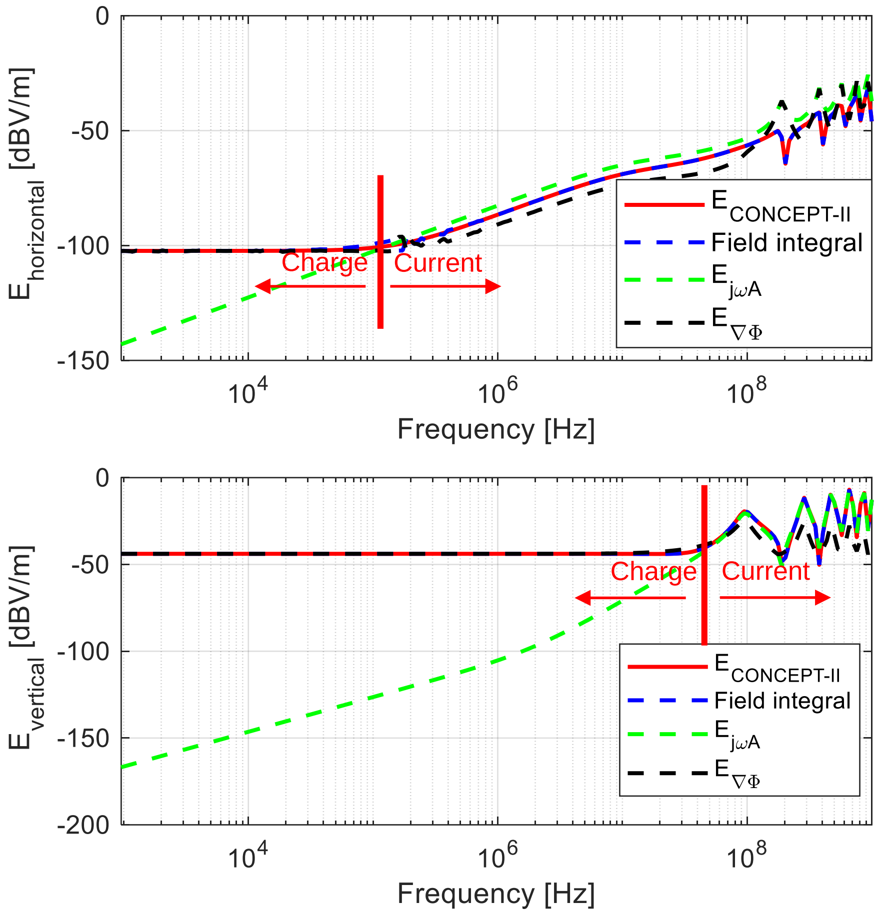

Figure 4.5: Electric field contributions from currents and charges.

Furthermore, the total electric fields from the two terms of (3.38) were separated to show the effect of the currents and charges. Since the formula (3.54) is only a numerical treatment, here, the original integral (3.38) is introduced for a clear explanation. The term depending on ∇Φ ($\vec{E}_{\nabla\Phi} = -\frac{1}{4\pi\varepsilon}\int_l \rho_l(z')\nabla'\mathrm{G}(\vec{r},\vec{r}')\,dz'$) represents the contribution from the charges, and the term depending on $j\omega A$ ($\vec{E}_{\mathrm{j}\omega A} = -\frac{j\omega\mu}{4\pi}\int_l I(z')\mathrm{G}(\vec{r},\vec{r}')\,dz'$) represents contribution from the currents. One can see that the charges are dominant for the horizontal electric field (the upper subfigure) from 1 kHz up to around 100 kHz. With increasing frequency, the currents become the dominant electric field sources. Similar results were also observed for the vertical electric field (the lower subfigure), where the charges dominate up to about 30 MHz.

4.2.5 Load Impedances

From the analysis shown in Figure 4.5, one can see that at the low frequencies for both horizontal and vertical electric field components, the charge-dependent term of the

EFIE is dominant. The charge distribution can be found based on the continuity equation (3.37). The voltage and current distribution along a cable structure are related to the load impedance. In this section, the variation of $E_{vertical}$ depending on the load impedance will be analyzed.

Firstly, it is assumed that load impedances are purely resistive. Figure 4.6 shows the variation of $E_{vertical}$ over the load resistance from 10 Ω to 10 MΩ for a $\frac{1}{4}\lambda$-long transmission line. The markers indicate the points where the field was calculated. The blue curve shows a linear interpolation. A change of about 15 dB can be observed.

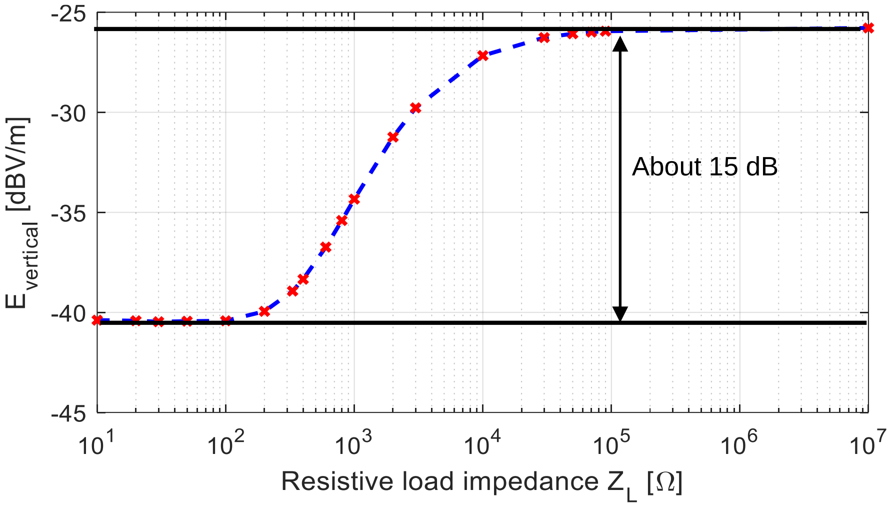

Figure 4.6: Electric fields related to resistive loads.

Loads may also have capacitive or inductive impedance characteristics. Therefore, an R-L-C series circuit was investigated, as shown in Figure 4.7. Z_L is a frequency-dependent complex function. Here, the influence of Z_L is investigated by changing only the phase of Z_L. The absolute value was constant, i.e., the $|Z_L| = 100$ Ω was chosen. The cable length was $\frac{1}{4}\lambda$ (= 1.5 m), and a frequency of 50 MHz was considered. E_{vertical} was calculated for different phase angles. Figure 4.8 shows changes of around 5.5 dB in E_{vertical} caused by phase shifts of the load from -90^o to $+90^o$.

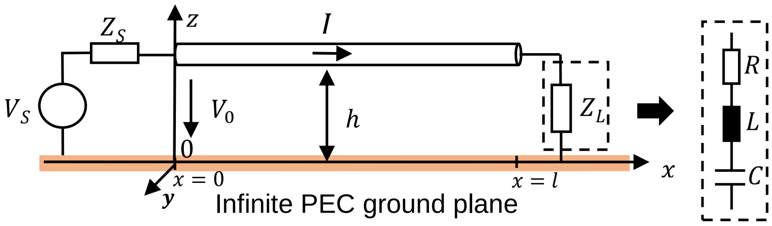

Figure 4.7: Cable configuration with RLC load impedance for Z_L.

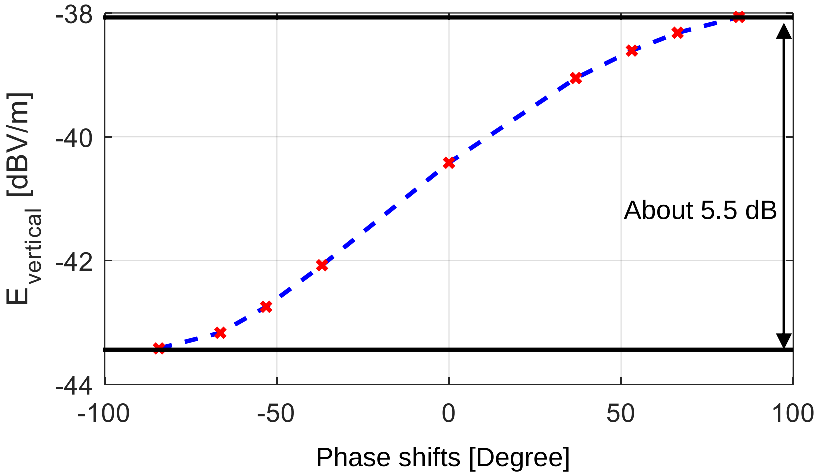

Figure 4.8: Electric field over the phase for a load impedance with constant absolute value.

Figure 4.9 shows the result for the frequencies 1 MHz, 10 MHz, and 30 MHz to illustrate the behavior of cable lengths that are shorter than $\frac{1}{4}\lambda$. It is obvious that the phase of the load impedance affects the emissions and near-field coupling also for lower frequencies. The influence increases with increasing frequency; for example, at 30 MHz, a 180° phase difference produces about 6 dB field difference. For higher frequencies, the field difference caused by the phase shift should be more significant. As an example, Figure 4.10 shows a maximum deviation of about 8 dB caused by phase changes of the load impedance for a frequency of 100 MHz.

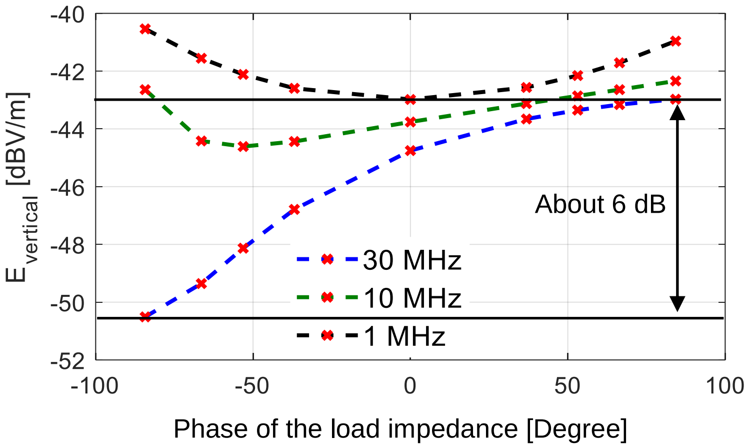

Figure 4.9: Electric field over the phase of the load impedance for different frequencies.

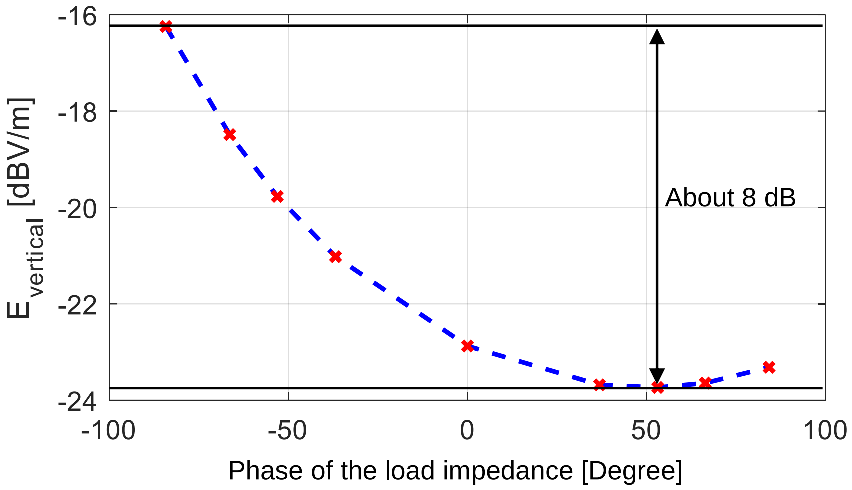

Figure 4.10: Electric field over the phase of the load impedance for 100 MHz.

4.3 Characterization of the Rod Antenna

The rod antenna specified in the standard is a one-meter long vertical monopole antenna. This antenna is used to capture the antenna voltage. The voltage multiplied with the antenna factor given by the antenna manufacturer gives the electric field in vertical polarization (perpendicular to the metallic table/chamber floor). Due to the low frequency and the metallic table, there are no significant other field components. In the following sections, the characteristics of the rod antenna will be discussed.

4.3.1 Position of the Rod Antenna - Field Regions

In general, field regions are fundamental parameters of the antenna. The boundary between near-field and far-field for antennas can be vaguely defined depending on the dimension of the antenna and the longest dominant wavelength of the system [51] (pp. 34-36). It should be noted that the boundary formulas are rules of thumb, and there are no precise cutoffs between regions. Mathematically, the boundaries can be defined, e.g., for a Hertzian dipole from formulas given in chapter 3, section 3.6, or described in [51] (pp. 154-160). When frequency approaches zero, formula (3.60) for $\vec{E}_\theta$ becomes (3.69) and finally (3.71). The formula (3.69) and (3.71) are special cases of (3.60), and valid in the near-field region. On the other hand, (3.64) is a special case of (3.60) for $\vec{E}_\theta$ in the far-field region. By comparing the contributions of the terms in parenthesis of formula (3.60) for $\vec{E}_\theta$, the near- and far-field regions can be defined.

In detail, for the Hertzian dipole, the field regions can be found by looking at the term $k_0 R$ in the formula (3.60) [51] (pp. 156-160). When $k_0 R \gg 1$ far-field conditions can be assumed. With $k_0 = 2\pi/\lambda$ it can be found that for the far-field region, $R \gg \frac{\lambda}{2\pi}$ should be valid. Vice versa the near-field region can be defined by $R \ll \frac{\lambda}{2\pi}$. For many engineering purposes the relation $\gg$ is often defined as a factor of 10, the accuracy is then sufficient for most purposes, which means a distance R of more than 2λ from the Hertzian dipole can be considered well as in the far-field region.

In the far-field region, some far-field characteristics are shown, such as electric and magnetic fields are coupled (see formula (3.63) and (3.64)); in free space, electric and magnetic fields are in phase with each other, and the intrinsic impedance η_0 (defined as the ratio of the electric and magnetic field strengths) is about 377 Ω; the field amplitudes drop with $1/R$.

In the near-field region where $R \ll \frac{\lambda}{2\pi}$, electric fields $\vec{E}_{\theta_{nf}}$ (in (3.69)) and $\vec{E}_{r_{nf}}$ (in (3.70)) are in time-phase, but they are in time-phase quadrature with the magnetic field $\vec{H}_{\varphi_{nf}}$ (in (3.66)) [51] (p. 157).

The used rod antenna in this work can be considered as electrically short, as its geometrical length (= 1 m) is much shorter than the dominant wavelength λ (= 10 m) at 30 MHz. The boundaries found for the Hertzian dipole can be assumed to be valid.

4.3.2 Antenna Factor

The authors of the CISPR 25 standard wanted to provide a simple to use instruction for quantifying the emissions from automotive electronic systems. Even when the expression of antenna factor might not be used properly, it is helpful to use the wording for the measurement specifications at high frequencies also for low frequencies. Therefore, an antenna factor is defined to calculate an electric field from a measured voltage. More accurate, it would have been to talk about a “sensor factor” as the antenna is more an electric field sensor [71]. In this work, the rod antenna Schwarzbeck, VAMP 9243 [72], is used. It is constructed according to the standard and consists of a vertical rod of one-meter length with a diameter of 16 mm and an amplifier with very high input impedance. The antenna factor of about +10 dB is given in the antenna manual, which was measured by a substitution method described in the CISPR standard16-1-4 [73]. Using the antenna voltage V_{Ant} with the manufacturer-provided antenna factor (AF) the vertical polarized electric field can be calculated:

$$E_{[\mathrm{dB\mu V/m}]} = V_{M[\mathrm{dB\mu V}]} + AF_{[\mathrm{dB(1/m)}]}. \tag{4.9}$$

The obtained electric field is only an approximated value. The AF of the VAMP 9243 is plotted in Figure 4.11. Variation of the AF along the whole frequency range is within 1 dB.

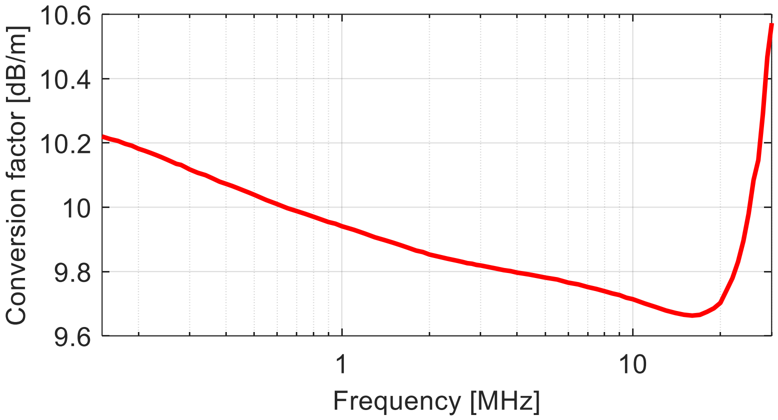

Figure 4.11: Antenna factor of VAMP 9243 [72].

4.3.3 Field Distribution at Rod Antenna Location and Huygens’ Surface

It is very important to analyze the field distribution at antenna location for CISPR 25 rod antenna for frequencies below 30 MHz. At such low frequencies, the antenna is in the near-field and the field at the antenna is not homogeneous. Furthermore, the CISPR 25 rod antenna is an active antenna, equipped with an amplifier with very high input impedance. In this section, the electric field distribution will be discussed at the antenna location, since the antenna is an electric antenna, i.e., mainly sensitive to electric fields. Furthermore, the influence of the rod antenna to the E-field distribution close to the cable structure will be investigated by comparing the E-field distribution on the defined Huygens’ surface with and without the rod antenna. This is important, because the field prediction relies on the field distribution on the Huygens surface. To predict correct CISPR 25 results, the rod antenna should not disturb significantly the fields on the Huygens’ surface.

The CISPR 25 rod antenna is specified especially for the CISPR 25 setup. The calibration and antenna factor calculation consider the special usage already. Calibration is defined in the standard CISPR 16-1-4 [73] by a pragmatic substitution approach. As the field along the rod antenna is not homogeneous, the question about the degree of inhomogeneity must be answered, i.e., can the field along the rod antenna approximated by a single value.

Electric field homogeneity analysis can be done directly with the CISPR 25 setup. The simplified model illustrated in Figure 4.2 is still used. The source impedance is assumed to be 50 Ω. The load impedances are set to be 5 Ω and 5 kΩ, to investigate some corner points.

Figure 4.12 and Figure 4.13 show the electric field distribution of the area calculated with CONCEPT-II between the center of cable and the location of the rod antenna for the 5 Ω and 5 kΩ load impedances at 1 MHz and 10 MHz respectively. The rod antenna was not included in the model. Shown is a side view of the structure (facing the cross-section of cable). When load impedance is 5 Ω, the cable self-inductance must be considered. Figure 4.12 illustrates the electric field distribution (magnitude of all field components) at 1 MHz (subfigure (a)) and 10 MHz (subfigure (b)). The field at rod antenna location gives a deviation within 5 dB at 1 MHz, and about 3 dB at 10 MHz. The deviation will become smaller with increased frequency, as far-field conditions result in a more uniform distribution. So the field distribution at 30 MHz is not shown here. With a load impedance of 5 kΩ, the current through the cable structure is small. At 10 MHz, the influence of cable self-capacitance to the metallic table becomes obvious. Figure 4.13 gives for both 1 MHz and 10 MHz a deviation of less than 5 dB.

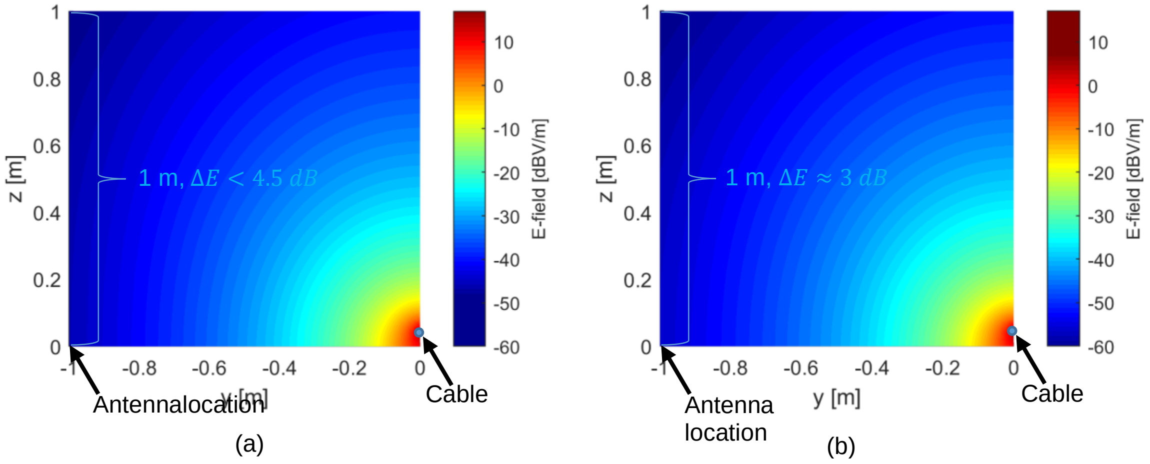

Figure 4.12: Electric field distribution between the location of the rod antenna and cable structure for load 5 Ω at 1 MHz (a) and 10 MHz (b).

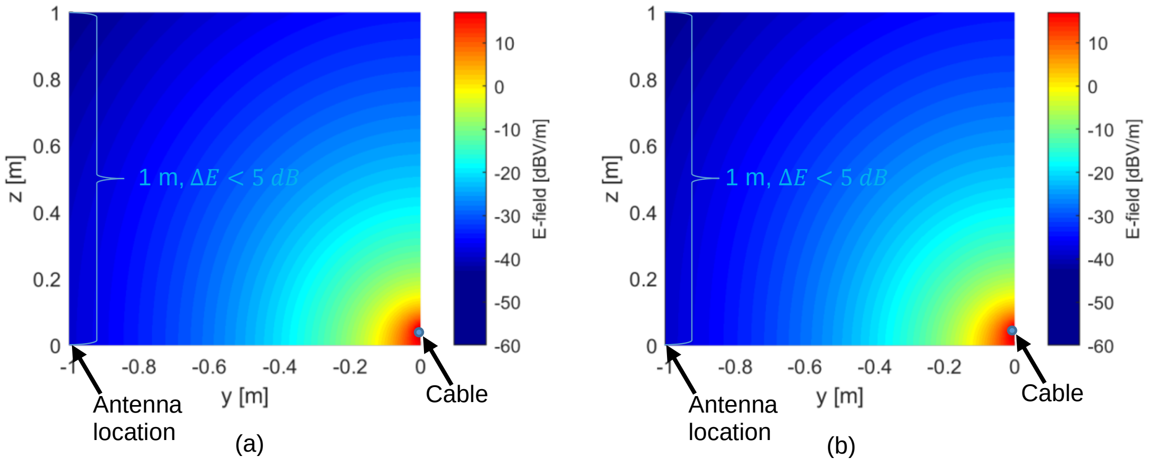

Figure 4.13: Electric field distribution between the location of the rod antenna and cable structure for load 5 kΩ at 1 MHz (a) and 10 MHz (b).

It can be seen from the above discussion that the electric field at the rod antenna location is weakly non-uniform, where a deviation within 5 dB is shown for the extreme cases. The field at the top of the rod antenna is smaller than the field close to the plate. At the height of 0.5 m, an average value can be assumed. Nevertheless, in this work, the reference field point is chosen to be at 10 cm above the plate. This gives a good consistency to the reference height used for frequencies above 30 MHz. Furthermore, a quite high field value can be found at this height. For pre-compliance analysis it is important not to underestimate the emissions of a system.

To find out if the presence of the rod antenna influences the field distribution over the Huygens' surface significantly, further simulations were done in CONCEPT-II by applying a simplified simulation model in Figure 4.2. The defined Huygens' surface has 5 cm distance to the cable structure, and the rod antenna location has 1 m distance to the cable structure. The configuration is specified in Figure 4.14. The Huygens' surface is parallel to xz-plane, which has 1.5 m width (parallel to x-axis) and 1 m height (parallel to z-axis).

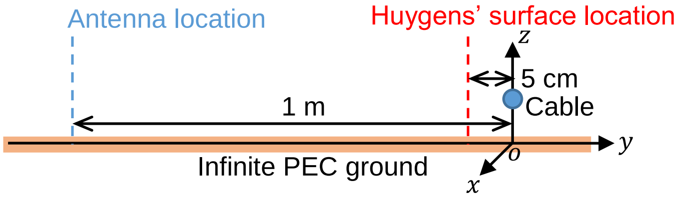

Figure 4.14: The location of the Huygens' surface and antenna location to the cable structure.

As an example, comparison of the electric field (expressed by the magnitude of all field components on the Huygens' surface) are shown in Figure 4.15 and Figure 4.16 for the model with 5 Ω load impedance at 1 MHz and 5 kΩ load impedance at 10 MHz respectively. The two cases are related to the cases that were studied in Figure 4.12 and Figure 4.13. Both Figure 4.15 and Figure 4.16 show a deviation within 0.01 dB, which confirms that the involvement of the rod antenna has a negligible influence on the E-field distribution close to the cable structure. This observation can be seen as proof that the feedback effect to the E-field distribution of cable structure caused by the rod antenna is minimal. The detailed analysis of the feedback effect influence will be described in chapter 4.4. Moreover, since the influence on the E-field distribution is negligible, it gives the possibility of applying the Huygens principle for electric field prediction at the rod antenna location without the existence of the antenna.

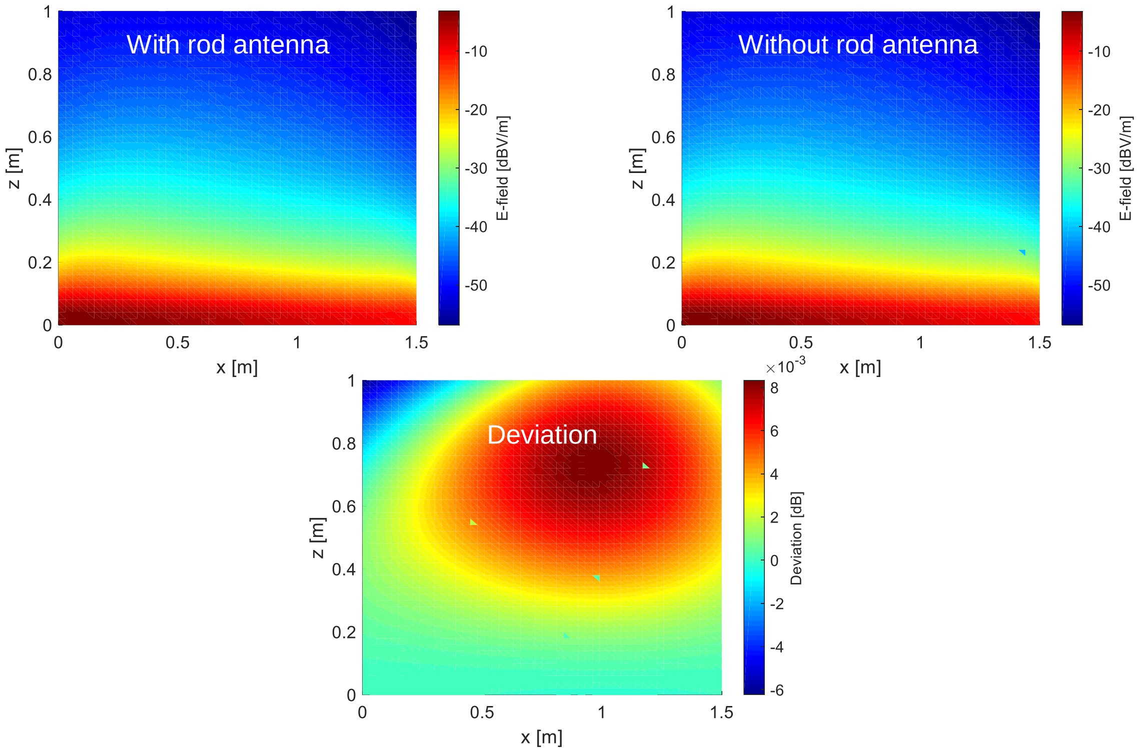

Figure 4.15: Comparison of electric field distribution on the Huygens' surface with and without antenna for 5 Ω load impedance at 1 MHz.

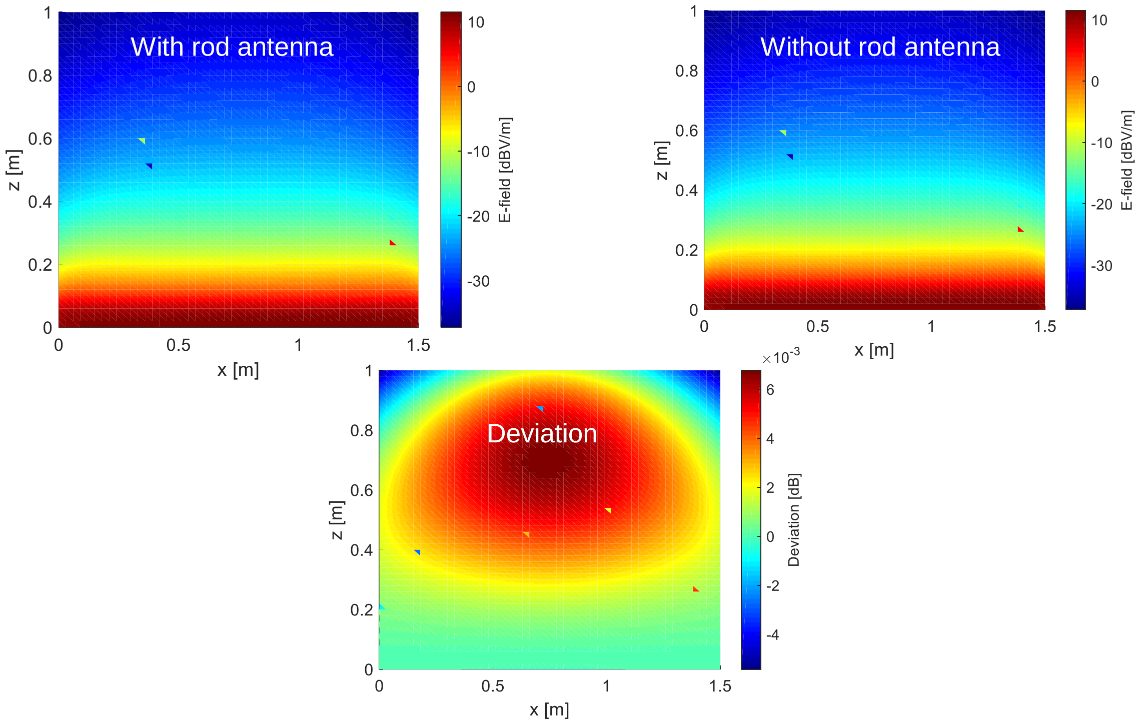

Figure 4.16: Comparison of electric field distribution on the Huygens' surface with and without antenna for 5 kΩ load impedance at 10 MHz.

4.3.4 Equivalent Circuit Model of Rod Antenna

An equivalent circuit of the rod antenna can be derived according to [15], which is shown in Figure 4.17. In the figure, (a) shows the rod antenna with a length h_A and thickness $2r_A$ perpendicular to the ground plane, where r_A is the radius of the rod antenna. The electric field E is assumed to be uniformly distributed (see the section 4.3.3). Z_A is the rod antenna input impedance seen at the feed point of the rod antenna. The electrical equivalent circuit can be formulated as an ideal current source I_A in parallel to Z_A and Z_M (Norton equivalent circuit), as shown in (b). The voltage drop V_M over the load impedance Z_M is the actual antenna voltage.

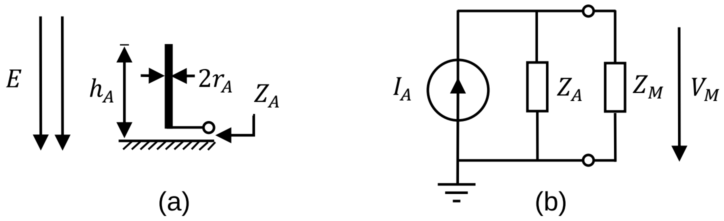

Figure 4.17: Illustration of a rod antenna (a), and the rod antenna's equivalent circuit (b).

The rod antenna's input impedance Z_A, in general, is a complex value, which depends on antenna size (length, thickness) and wavelength. It can be written as [51]:

$$Z_A = R_A + jX_A. \tag{4.10}$$

The real part R_A consists of two components:

$$R_A = \mathrm{R}_{loss} + \mathrm{R}_{rad}, \tag{4.11}$$

where

R_{loss} : Loss resistance of the antenna;

R_{rad} : Radiation resistance of the antenna.

The losses of the antenna (R_{loss}) are frequency- and material-dependent, and usually can be neglected as $R_{loss} \ll R_{rad}$[74]. R_{rad} relates to the energy that radiates into space in case the antenna is used as a transmitting antenna. For a short monopole antenna, [75] gives an approximation of R_{rad} valid as long as the antenna length $h < 0.14\lambda$,

$$R_{rad} \approx 40\pi^2 \left(\frac{h}{\lambda}\right)^2. \tag{4.12}$$

For example, if the antenna is 1 m long at a frequency of 10 MHz, the radiation resistance is only 0.4386 Ω. The reactance part, X_A, is capacitive for an electrically short antenna [77],[78]. Therefore, the input impedance can be approximated to

$$Z_A \approx \frac{1}{\mathrm{j}\omega C_A}. \tag{4.13}$$

C_A is antenna capacitance, which is frequency independent as long as the antenna is electrically short. The value can be approximated as [15]:

$$C_A = \frac{2\pi\varepsilon_0 h_A}{\ln\left(\frac{h_A}{r_A}\right) - 1}. \tag{4.14}$$

The simplified equivalent circuit is shown in Figure 4.18.

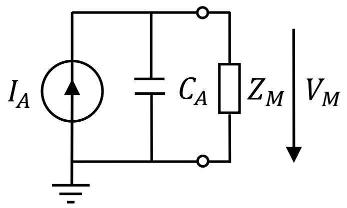

Figure 4.18: Equivalent circuit of an electrically short rod antenna.

Equivalent source current I_A of the antenna is given by [15]:

$$I_A = j\omega\varepsilon E A_{eff}, \tag{4.15}$$

in which A_{eff} is the effective antenna area,

$$A_{eff} = \frac{C_A}{\varepsilon} \cdot h_{eff}, \tag{4.16}$$

and h_{eff} is the effective height of the antenna. For an electrically short antenna h_{eff} is given by [75]:

$$h_{eff} = \frac{h}{2}. \tag{4.17}$$

The voltage V_M can be expressed as [77]:

$$V_M = I_A \frac{Z_A Z_M}{Z_A + Z_M} = j\omega\varepsilon E A_{eff} \frac{Z_A Z_M}{Z_A + Z_M}. \tag{4.18}$$

By inserting formula (4.13) and (4.16) to the expression (4.18), V_M can be written as:

$$V_M = j\omega C_A E h_{eff} \frac{\frac{1}{j\omega C_A} Z_M}{\frac{1}{j\omega C_A} + Z_M}. \tag{4.19}$$

Z_M is defined by the load, i.e., the amplifier with very high input impedance and should be as high as possible ($Z_M \gg \frac{1}{j\omega C_A}$). In this case, the voltage V_M in (4.19) can be approximated as $V_M \approx E \cdot h_{eff}$, which means the antenna is a self-integrating antenna with constant frequency response. It can be shown that high-impedance load Z_M gives the highest antenna voltage for practical applications.

EMI measurement receivers are terminated with 50 Ω. Since this impedance is too low, $Z_M \gg \frac{1}{j\omega C_A}$ is not valid. Thus, an impedance matching unit/amplifier with very high input impedance is needed between the high-impedance load Z_M and receiving system (50 Ω). Such impedance is implemented with transistor (FET) circuits; the antenna is connected to the gate of the transistor. Such circuits can offer an impedance of approximately 10 pF in parallel with more than about100 kΩ [76].

4.4 Analysis of Coupling Mechanisms and Feedback Effects

Based on the assumption that the wavelength λ of a disturbing signal is much larger than the overall dimension of a measurement setup (including cable bundle and rod antenna), near-field simplifications can be applied to analyze the coupling mechanisms. There are two fundamental coupling mechanisms: inductive coupling and capacitive coupling. Figure 4.19 gives a sketch of the capacitive coupling (represented by the mutual capacitance C_C) and inductive coupling (represented by mutual coupling inductance M).

As the short ground-based rod antenna required for CISPR 25 setups is not a loop antenna and is terminated with a high impedance amplifier, the rod antenna is very sensitive to electric fields, i.e., capacitive coupling, and insensitive to magnetic fields, i.e., inductive coupling. A short rod antenna terminated with high impedance can be also called an E-field sensor [71]. Typically, the amplifier is a transistor (FET) circuit, providing a high termination input impedance for the rod antenna (described in section 4.3). The output impedance of the amplifier is typically $50\,\Omega$ for connecting the measurement devices. This way, an antenna voltage measurement can be realized.

Equivalent circuit models [42] are commonly used to analyze low frequency coupling mechanisms. Most existing circuit models are used mainly to analyze the influence of the capacitive coupling, e.g., in [15],[40],[41],[79]. Inductive coupling is not discussed and neglected, as it is very weak. As proves for this assumption are rare, inductive coupling contribution will be discussed in this work together with capacitive coupling.

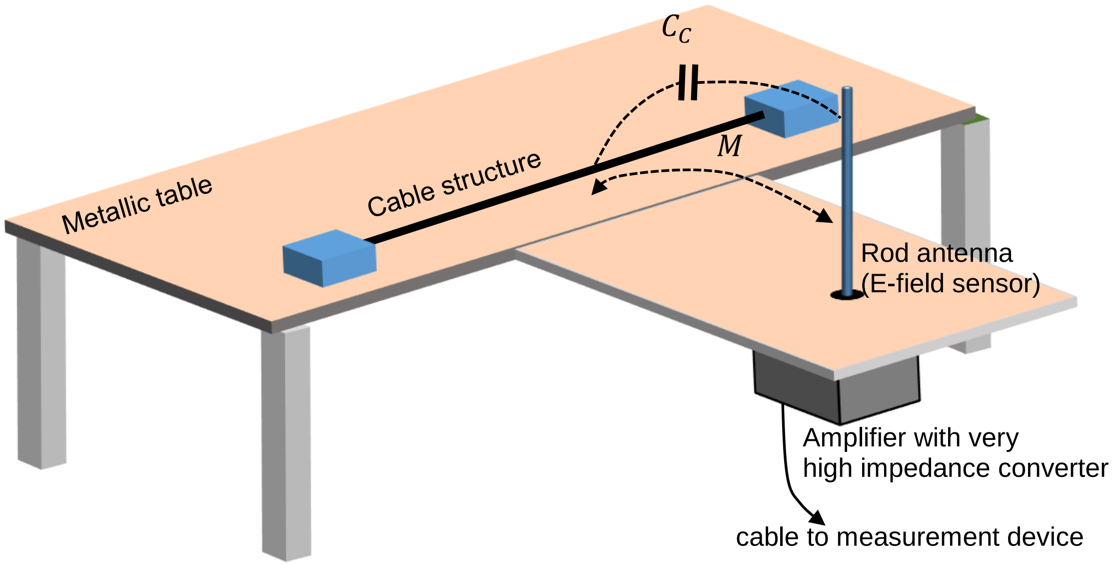

Figure 4.19: Sketch of capacitive and inductive coupling between on table structure and rod antenna.

4.4.1 Simple Equivalent Circuit Model

The capacitive coupling (mutual capacitance C_C) and inductive coupling (mutual coupling inductance M) in Figure 4.19 are represented in a simplified equivalent circuit model in Figure 4.20. In the figure, the on-table cable structure is modeled by a lumped-circuit model consisting of a voltage source V_S, a source impedance Z_S, a load impedance Z_L. The cable structure is represented by L_{TL} and C_{TL} (based on the transmission line theory, see the model in Figure 4.3, losses can be neglected). The antenna equivalent circuit consists of the lumped self-capacitance C_A and self-inductance L_A. A load Z_M is attached.

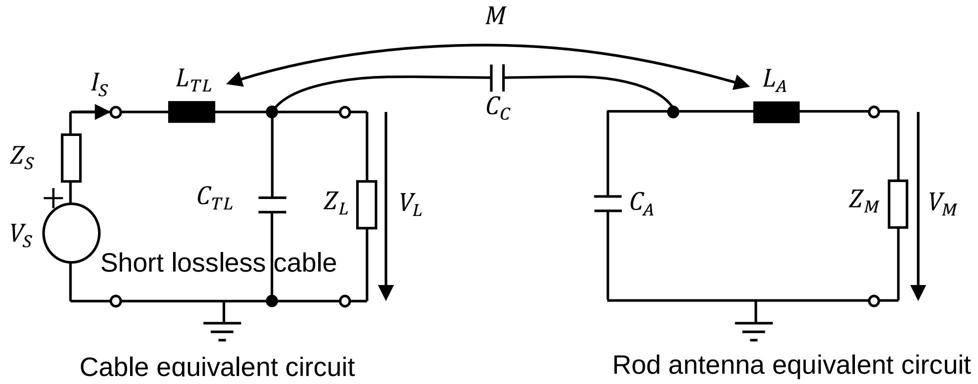

Figure 4.20 Simple equivalent circuit model for the CISPR 25 measurement setup.

The capacitive coupling can be considered as follows: the varying voltage on the cable structure generates a time-varying electric field. A portion of the field lines terminates at the antenna rod, and a current is generated in the rod. The small current generates a voltage drop at the high impedance termination Z_M of the rod antenna. Mainly the electric field will be measured. The coupling capacitance is in fF range [40],[41]. For example, in [40] a mutual capacitance of 15-24 fF was applied depending on the configurations. Similar investigations can be found in [41], where the mutual capacitance was found to be 52 fF or 146 fF. Since the purpose of this section is to investigate the behavior of coupling mechanisms, instead of finding an exact equivalent model, the coupling capacitance from [41], $52\ \mathrm{fF}$, is applied here.

The inductive coupling can be considered as follows: in case of the grounded rod antenna, the inductive coupling can only take place by the loop, which is formed by the antenna, the antenna self-capacitance to ground, and the antenna load realized by an amplifier with very high input impedance. As the self-capacitance of the antenna C_A is about 10 pF (approximated by (4.14)), the voltage drop across the self-capacitance is much larger than the voltage drop across the inductance of the antenna structure. The inductive coupled voltage is split mainly between the antenna amplifier impedance and the antenna self-capacitance. The orthogonality and symmetry of the rod structure with the cable furthermore reduce the inductive coupling. These considerations are supported by mutual inductance calculations. The mutual coupling inductance M is responsible for the inductive coupling between the cable structure and the antenna. Determination of the mutual inductance is not trivial, because the overall geometry of the setup is complex. With the quasi-static numerical solver FastHenry2 [68] a mutual coupling inductance of 0.3 nH could be calculated (see Appendix D) for the CISPR 25 geometry. In [15] a mutual inductance between cable and the receiving antenna in a vehicle was found in a range of 0.1 nH and 1 nH. This confirms the FastHenry2 result.

Typical antenna parameters ($C_A = 10\ \mathrm{pF}, L_A = 1\ \mathrm{\mu H}, Z_M = 100\ \mathrm{k\Omega}$) combined with C_C and M will be used to analyze the influence of the capacitive and inductive couplings in the coming section. Here, C_A can be approximated using (4.14); L_A describes the self-inductance of the antenna, which can be estimated using (9.50) in Appendix E.

As the mutual capacitance C_C ($= 52\ \mathrm{fF}$) from cable structure to the rod antenna is much smaller than self-capacitance from rod antenna to the ground plane ($C_A = 10\ \mathrm{pF}$), the small antenna voltage does not significantly affect the voltage from source cable to ground. Furthermore, both high impedance of the antenna amplifier input and high impedance of self-capacitance limit the currents flowing through the antenna due to inductive coupling. I.e., mutual back coupling to the cable structure can be neglected. The feedback effects caused by the mutual back couplings can be also observed by analyzing voltage at the load V_L of the cable structure. Both V_M and V_L will be calculated in the next two sections.

4.4.2 Comparison of Capacitive Coupling and Inductive Coupling

The circuit model in Figure 4.20 was calculated with a circuit simulator. The parameters of cable structure ($V_S = 1\,\mathrm{V}, Z_S = 50\,\Omega, Z_L = 100\,\Omega, L_{TL} = 1.5\,\mathrm{uH}, C_{TL} = 18\,\mathrm{pF}$) were used, as well as the abovementioned antenna parameters and mutual coupling parameters. Figure 4.21 gives the influence of the antenna voltage V_M caused by both capacitive and inductive couplings. The green curve and red curve show respectively the contribution of the capacitive coupling and inductive coupling to the antenna voltage. The blue curve shows the contribution of both couplings. It can be seen that compared with inductive coupling, the capacitive coupling dominates. The inductive coupling can be neglected at low frequencies.

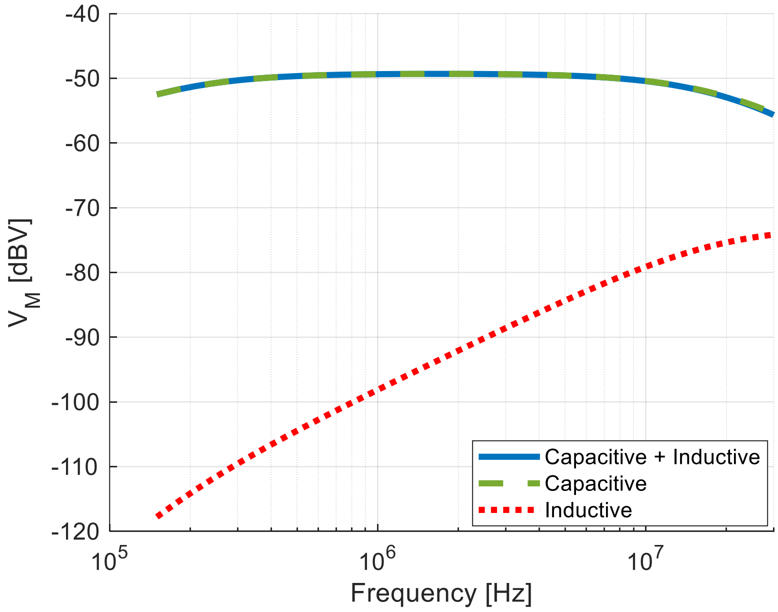

Figure 4.21: Influence of capacitive and inductive couplings to the antenna voltage.

4.4.3 Feedback Effects

Feedback effect caused by the mutual capacitive coupling and the mutual inductive coupling is analyzed by observing the voltage drop V_L at the load of the cable structure, as shown in Figure 4.22. As pointed out already in section 4.4.1, feedback effects can be theoretically neglected. The model in Figure 4.20 is also used now for quantifying the effects. The idea is that if the feedback effect dominant, the voltage drop V_L should be varied with/without the presence of the antenna. In the figure, the black curve gives the voltage drop V_L over frequency from only the cable structure, where the antenna is not included. The dark blue curve gives the voltage drop V_L when the antenna is present. It can be seen that both curves are close together, which means the feedback effect from both the capacitive and inductive coupling can be neglected.

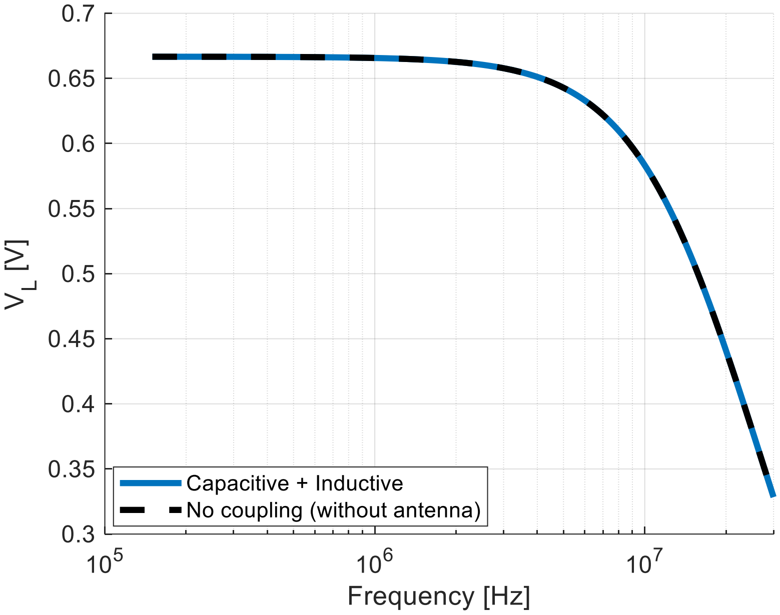

Figure 4.22: Analyzing feedback effects by observing voltage at the load of the cable structure.

A more detailed derivation for the mutual inductive coupling and the capacitive coupling and the related feedback effects can be found in Appendix E.

4.4.4 Extended Equivalent Circuit Model based on Capacitive Coupling

As described in the above sections, inductive coupling is very weak, and capacitive coupling is dominant. The model used in the section 4.4.1 is a simple model. Now, a refined model considering the voltage and current distribution along the cable structure is presented. The model is shown in Figure 4.23.

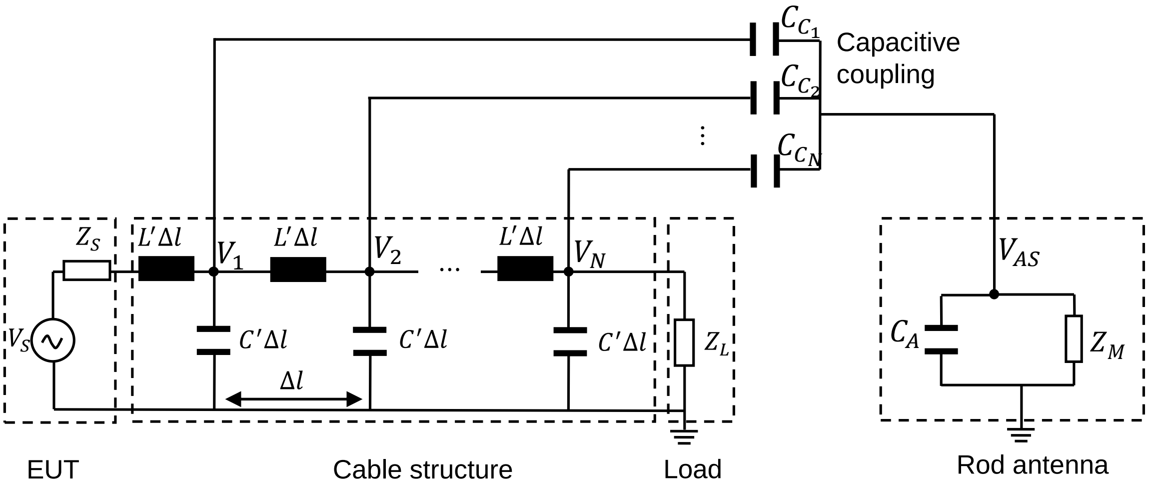

Figure 4.23: Circuit model of CISPR 25 measurement setup.

In this more accurate model, the cable (length l) is segmented into N subsegments. The length of each segment is expressed as $\Delta l(= l/N)$. The per-unit-length capacitance C' and inductance L' are used to model each segment (see Figure 4.3).

$V_1, V_2, \cdots, V_N$ represent the common-mode voltages at discrete locations. $C_{C_1}, C_{C_2}, \cdots, C_{C_N}$ describe the parasitic capacitances between the cable bundle segments and the receiving antenna [79]. The receiving antenna (1-m-long vertical monopole antenna) is modeled by its self-capacitance C_A in parallel with Z_M (as the antenna amplifier impedance). The self-inductance of the antenna L_A is ignored, as the contribution of L_A is very weak compared with that of Z_M. The considered monopole antenna has a value C_A of $10\ \mathrm{pF}$.

To verify the proposed circuit model, a cable having a radius of 0.4 mm and 5 cm height above ground was used. The source V_S is set to 1 V with $Z_S = 50\ \Omega$. The load impedance Z_L is set to 100 Ω. In the circuit, the per-unit-length inductance L' and capacitance C' were calculated using (4.2) and (4.3), respectively. The circuit is calculated with SPICE. Also, the structure was simulated with MoM (CONCEPT-II). Figure 4.24 compares the antenna voltage from the SPICE model with the MoM result. The deviation is only about 1 dB, which shows again, as discussed in chapter 2, that equivalent circuit models work well for simple structures in the low frequency range.

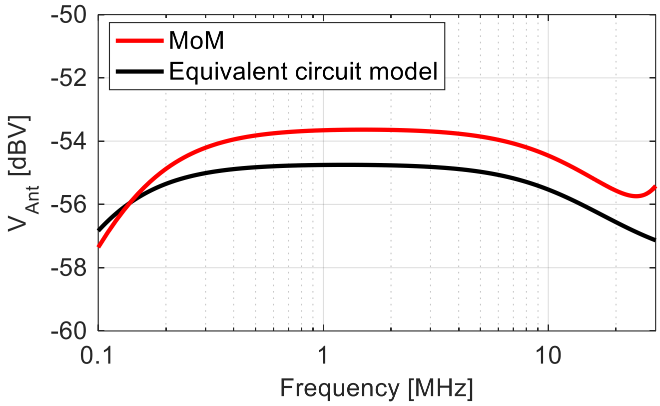

Figure 4.24: Comparison of antenna voltages from MoM (CONCEPT-II) and the circuit model.

4.5 Analysis of Table and Shielded Room Influence

Resonance problems are often reported for CISPR 25 field measurements at low frequencies, for example, in [80] and [81]. To investigate the root cause of such resonances introduced by measurement setup itself, [82] used the field simulation program CST MWS [65] to model different configurations of the measurement setup. The configurations include varying chamber sizes and different bonding schemes of the receiving antenna counterpoise, as well as variations in the grounding scheme of the conducting metallic table. It could be found that: resonance caused by chamber size can be important. For example, in [82] a large chamber was investigated; here, the first resonance appears already at 23 MHz. In [83] and [41] chambers were investigated, which came into a resonance above 30 MHz. More important is the grounding scheme of conducting metallic table. The capacitance of the metallic table to the chamber floor and the grounding inductance cause a resonance below 30 MHz [81].

In this work, considering that the cable structure involved in CISPR 25 setups is less than a half wavelength up to 30 MHz, it is assumed that possible resonances can only be introduced by the chamber and the table grounding scheme inside setups. The analysis is based on a simplified model (see Figure 4.2) and CONCEPT-II simulations.

4.5.1 Shielded Room

A metallic chamber is needed to have a noise-free environment for sensitive and reproducible measurements. Often absorbing material on walls and ceilings should potentially minimize reflections from the metallic walls. However, at lower frequencies, the absorbing material does not work. CISPR 25 demands for the absorber materials only a minimum performance below 70 MHz. In [65], a measurement setup below 30 MHz was simulated in the field simulation program CST MWS to observe whether absorbers influence the electric field. A setup placed on an elevated ground plane with perfect absorbers on the walls contrasts a setup that used PEC on the walls. The results showed large differences above 20 MHz, which can be attributed to the chamber absorbers. The absorbing walls may start to absorb in the range of 10-20 MHz.

As at higher frequencies, cavity resonances have to be considered. Depending on the size of the chamber, the resonance frequency can be calculated by [84]

$$f_{m,n,p} = \frac{1}{2\sqrt{\varepsilon_0\mu_0}}\sqrt{\left(\frac{m}{a}\right)^2 + \left(\frac{n}{b}\right)^2 + \left(\frac{p}{d}\right)^2}. \tag{4.20}$$

m, n, p are integer (≥ 0), where at least two of the three must be non-zero; a, b, d describes the chamber dimensions. The used chamber dimensions for this work: $a =$ 6.45 m, $b =$ 4.2 m, $d =$ 3.1 m. The calculated lowest resonance frequency appears at 42.6 MHz. Therefore, the cavity resonances of the shielding room can be neglected below 30 MHz.

4.5.2 Metallic Table Grounding Schemes

Resonances can also be caused by the capacitor formed by the metallic table and the chamber floor and by the inductive ground connection of the metallic table. Typical ground connections between the metallic table and the chamber floor are studied. The configurations shown in Figure 4.25 are screenshots from CONCEPT-II simulations.

The metallic table has a length of 2 m and a width of 1 m. The antenna-table bonding is 1.5 m long and 1 m wide. Figure 4.25 (a) creates the connection through a vertical metal plane of 2 m long and 0.9 m high, which is similar to the configuration in [81].

Figure 4.25 (b) shows a connection with eight metal stripes, that is used in [56], [85] and [86].

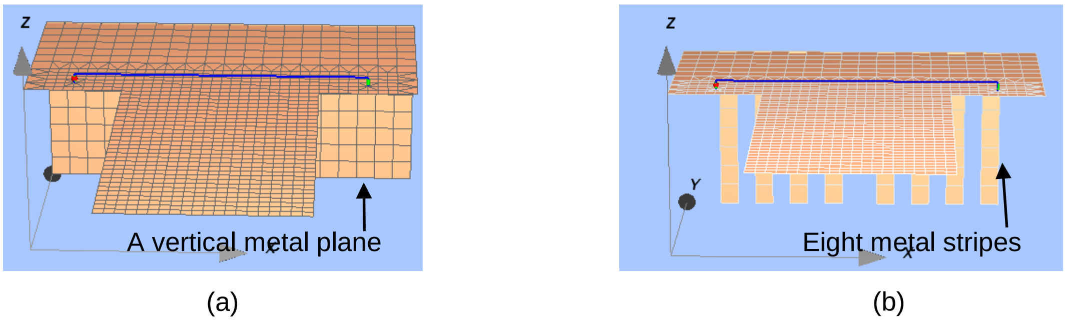

(a) (b)

Figure 4.25: CONCEPT-II models for different ground connections between the metallic plane and chamber ground, (a) grounding through a vertical plane, (b) grounding through eight metal stripes.

The electric fields obtained from the simulations are presented in Figure 4.26. The red curve is obtained from CONCEPT-II, where the simplified model shown in Figure 4.2 is used, the table with the antenna is here in free space. The solid blue line shows the results from a ground connection in Figure 4.25 (a). The dashed black line gives the electric field from the setup shown in Figure 4.25 (b). The solid blue curve matches well with the dashed black curve. Both curves show a resonance at approximately 18 MHz. This resonance is known from several investigations [81],[83] and is caused by the inductance of the ground connection together with the table capacitance. Depending on the termination impedances, this resonance can become stronger or weaker. Both curves follow the red curve with about 2 dB deviation below 10 MHz. The deviation is introduced by the involved metal structures.

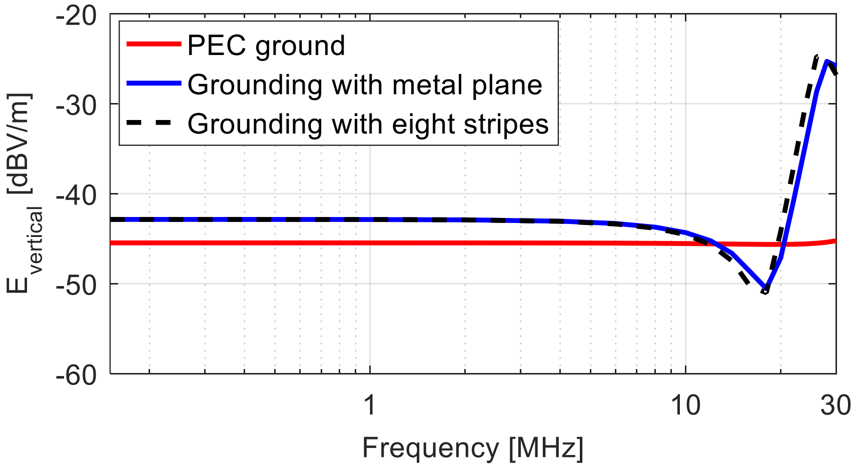

Figure 4.26: CONCEPT-II results showing the influence of different grounding schemes between the metallic table and chamber floor.

5 Electric Field Estimation Methods

The emissions and the near fields are caused by the common-mode current/voltage distributions along the cable bundle. In chapter 2, it is mentioned that the MDM method for predicting the electric fields shows deficiencies when used with measurement data. The first major research question of this thesis is to find the root cause of these deficiencies. In this chapter, the MDM method is described in detail, and an answer will be found for the question, why the MDM method fails.

To answer the second major research question of this thesis, in this chapter, a Huygens principle-based approach will be introduced, which uses near-field distribution instead of the common-mode currents as the sources to predict the electric fields in space. The Huygens principle is used here with a truncated Huygens’ surface. This approach is later verified based on simulation data. Furthermore, a static dipole-based approach is introduced.

5.1 Multi-Dipole Model (MDM) for Low Frequencies

Modeling near- and far-fields of CISPR 25 measurement setups using equivalent dipole radiation models based on measured common-mode currents have already been discussed, for example, in [31]. However, at low frequencies, this method fails. In this chapter, the limitations of the MDM method will be investigated.

In this chapter, the creation of the MDM model is described. After that, the accuracy of the method will be analyzed. It will be shown that the accuracy of the current distribution is the limiting reason for the poor performance of the MDM method at low frequencies.

5.1.1 Multi-Dipole Model (MDM)

To create a MDM radiation model from a current-carrying cable bundle, several steps are needed, as shown as follows:

Step 1: Subdivide the involved cable bundle into short sections (cable segments) and identify the centers of each segment.

Step 2: Conduct common-mode current measurements at the centers of cable segments.

Step 3: Assign the currents from current measurements as constant current to each cable segment.

Step 4: Model the radiation of each current segment as the radiation of an ideal dipole with the length of the segment and carrying the segment current.

Step 5: Add a set of image dipoles, replace the good conducting ground plane by applying the image theory.

Step 6: Combine the dipoles from Step 3 and the image dipoles from Step 5 to obtain the full multi-dipole model (MDM).

The radiated fields can be considered as a superposition of fields produced by the dipoles of the MDM, where the fields contributed from each current segment are considered from the ideal dipole through (3.59)-(3.61). An example of MDM creation is illustrated in Figure 5.1. The cable bundle with a length l placed above ground at height h is oriented parallel to the *x*-axis. The cable bundle is subdivided into N segments. The common-mode currents along the cable segments are known. They are denoted by $I_1, I_2, \cdots, I_N$. Each cable segment's common-mode current is modeled by an ideal dipole. The arrow over the dipole indicates the direction of the current flow and the dipole orientation. To include the ground plane effect into the model, the image theory is used by introducing a set of images. Therefore, the PEC ground plane (plane z=0) is not shown here.

The EUT and the load connect the cable to the ground plane. Thus, they are included by equivalent vertical connecting currents I_s and I_L, respectively. Introducing the vertical dipoles at both ends of the cable bundle creates a physical meaningful common-mode current flow path from the cable bundle to the ground plane that forms a closed circuit. Figure 5.1 shows the EUT and load replaced by one dipole. Real modeling may include many dipoles, as this increases the accuracy of the estimated fields.

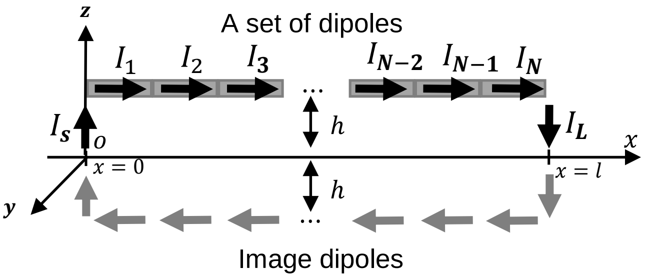

Figure 5.1: A sketch of a MDM for a cable above a PEC plane connected at both ends to the PEC plane.

5.1.2 Accuracy Analysis of MDM

This section focuses on the fields calculated with MDM at low frequencies from measured currents. As mentioned already, the method suffers from inaccuracies in the low frequency range [21]. First, the errors of the MDM method will be illustrated by using the measured currents. Then, in this section, it will be analyzed why the method fails at low frequencies.

5.1.2.1 **MDM at Low Frequencies Using Measured Currents**

The structure given in Figure 4.2 was used for investigation. The cable was driven with the first port of a VNA (Agilent E5071B [87]) and terminated with 10 Ω. The currents were measured using an FCC-F65 current probe at different locations along the cable. The second port of the VNA was connected with the probe to record the measured data. A VNA was used here, as with the VNA measurements, a quite accurate phase-resolved current distribution can be obtained. Since the short vertical ground connections are very short and difficult to measure. The measured currents at both ends of the cable were used to represent the vertical parts in the model.

The MDM-estimated electric field is shown in Figure 5.2. The red curve represents the field reference (obtained directly from CONCEPT-II simulation). The black curve gives the MDM result, where the measured currents (captured by the VNA) are used for creating the model. The blue curve gives the MDM result where a special measurement uncertainty is added to the simulated currents (extracted from CONCEPT-II). Here the measurement uncertainty is realized by shifting the position of dipoles within 5 mm in a random way [88] for modeling possible dipole positioning errors. The curves show that for frequencies above 10 MHz, all three curves have a good match. A large deviation can be seen below 10 MHz between the MDM results and the reference field. Since the currents obtained from the VNA based measurements are considered to be quite accurate, the deviation observed in the blue curve is mainly caused by the added positioning errors, which means the current distribution along the cable influences the accuracy of the MDM method.

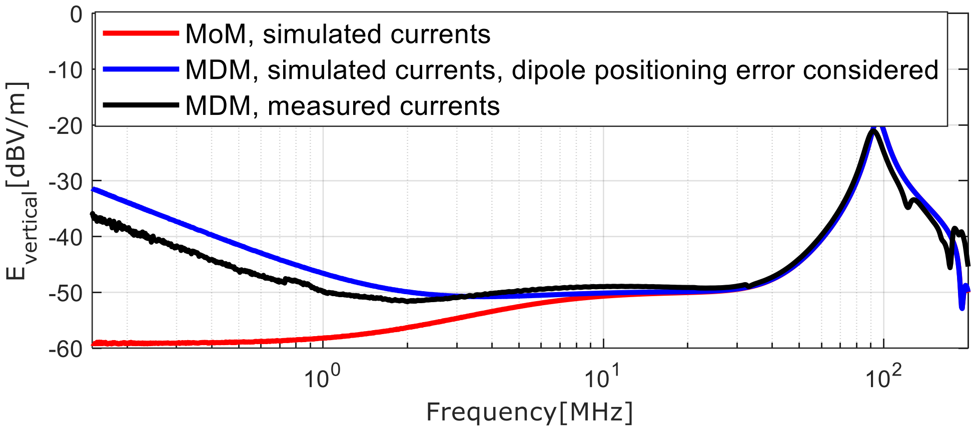

Figure 5.2: Field $E_{vertical}$ calculated with the multi-dipole model from measured currents and MoM.

5.1.2.2 **Minimum Usable Frequencies for MDM**

It was shown in the last section that there is a frequency limit, where MDM accuracy decreases significantly. The configuration in Figure 4.2 was used for further investigation to find the minimum usable frequencies for the MDM method. The cable was driven by an ideal voltage source of 1 V with 50 Ω source impedance and terminated with

100 Ω. A screenshot of the model in the CONCEPT-II is shown in Figure 5.3 (a). Thirty basis functions were used for the horizontal cable, and three basis functions were used for each vertical connection. An observation line indicated by the red dashed line in the figure was set at 1 m from the center of the cable and 10 cm above the ground plane.

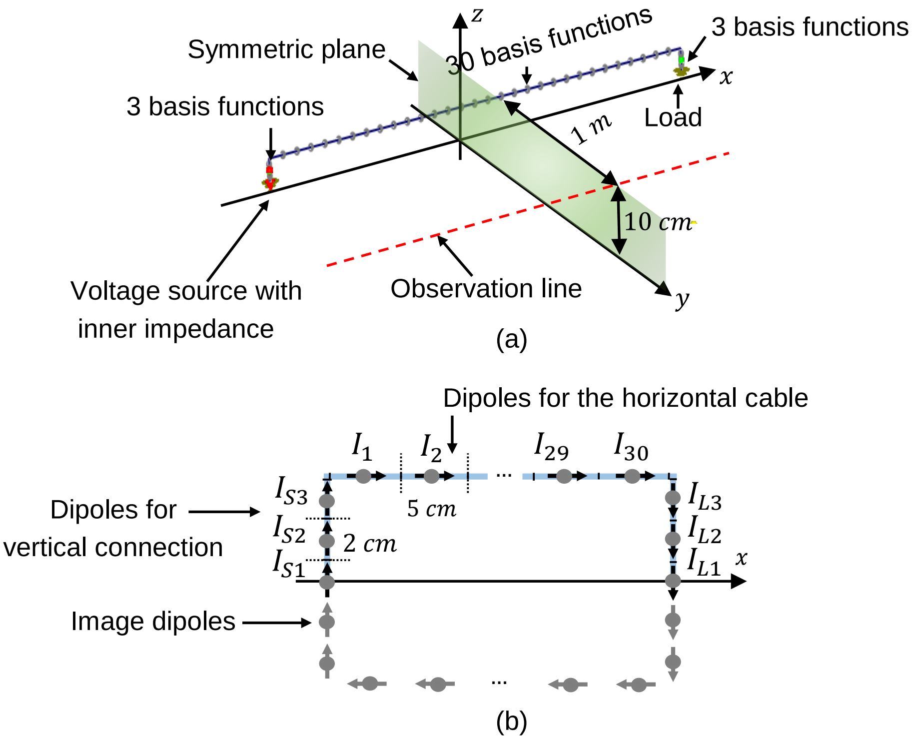

Figure 5.3: Model of a cable above ground. (a) a sketch of the model with segmentation, (b) the dipoles used for creating the MDM.

The MDM procedure needs the cable current as an input parameter. Different from the MDM creation process illustrated in the section 5.1.1, the current distribution was obtained using MoM. The location, direction, and the number of dipoles and their images are shown in Figure 5.3 (b). The segment length of the horizontal cable is 5 cm and the segment length of the vertical connection is 2 cm.

Figure 5.4 compares the calculated vertical components of the electric fields (E_z) along the observation line. In the figure, (a) illustrates the field distribution from the field integral formulation ($E_{z(\mathrm{MoM})}$) and (b) shows the data obtained from the MDM ($E_{z(\mathrm{MDM})}$). Differences in the fields mainly occur at low frequencies. $E_{z(\mathrm{MoM})}$ is almost constant for frequencies up to 100 kHz in (a), whereas two areas of strong fields and one symmetry plane of field cancellation exists exactly in the middle of the observation line in (b). The absolute deviation of E_z in dB is illustrated in the subfigure (c). The deviation at low frequencies reaches about 60 dB, but almost no deviation can be observed over the symmetry plane. Above about 100 kHz, the deviation tends to be very low. This finding is different from the results in Figure 5.2. Here only the termination was different. The reasons are investigated now.

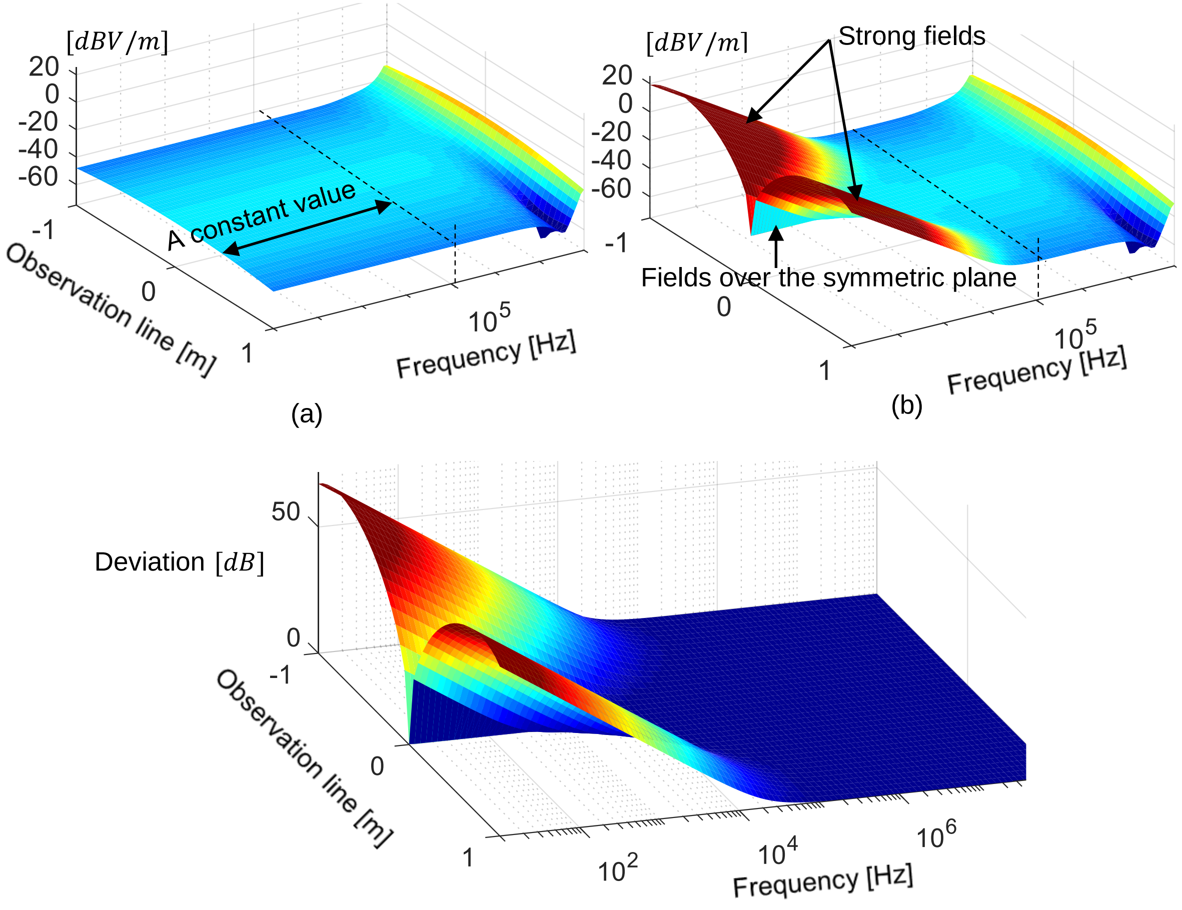

(a)

(b)

(c)

Figure 5.4: Comparison of E_{vertical} of the field observation line. (a) fields are obtained from electric field integral formulation, (b) fields are obtained from the MDM, (c) absolute deviation in dB.

To investigate the minimum usable frequency of the MDM, the loop model in Figure 5.3 was used, where the source impedance was 50 Ω and the load impedances varied from 1 Ω to 1 kΩ. Fields were calculated at 1 m, 5 m, and 10 m away from the structure. To avoid the symmetry plane of the model, that is not critical for the MDM, the observation points were shifted to -0.1 m and -0.75 m in the *x*-direction along the observation line shown in Figure 5.3 (a). The number of dipoles used for MDM creation is the same as that specified in Figure 5.3 (b). For each observation point and load impedance, the frequency which causes a deviation between $E_{z(\mathrm{MoM})}$ and $E_{z(\mathrm{MDM})}$ of 3 dB is considered as the minimum usable frequency. The results are shown in Figure 5.5. The star markers in the figure indicate the configured load impedances. The increase in the distances between the observation points and the cable structure causes the minimum usable frequency to decrease. Furthermore, the observation points closer to the symmetry plane of the model (x = -0.1 m, (a)) have smaller minimum usable frequencies than the observation points away from the symmetry plane of the model (x = -0.75 m, (b)). The minimum usable frequencies decrease when lower load impedances are used. The accuracy of MDM is very low at low frequencies under low load impedance conditions.

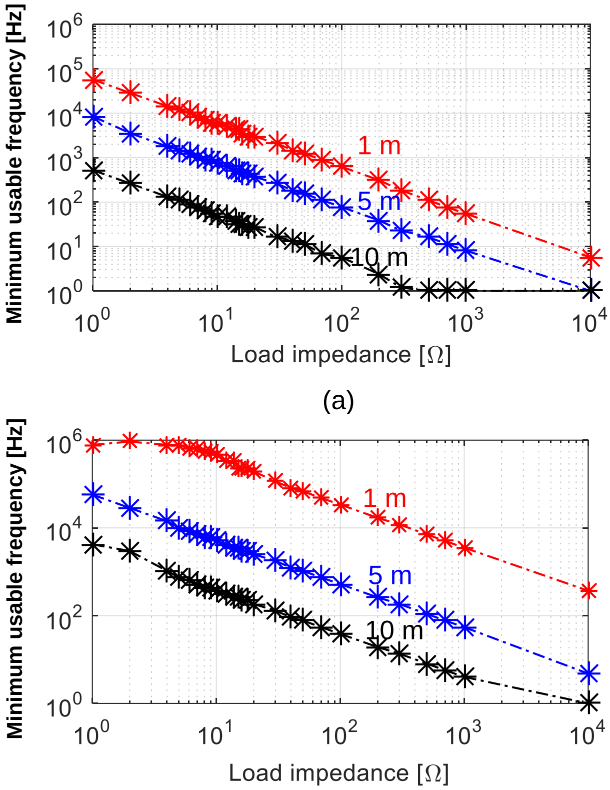

(a)

(b)

Figure 5.5: Minimum usable frequency of MDM related to the configuration from Figure 5.3, for different load impedances and observation points. (a) x = -0.1 m, (b) x = -0.75 m.

5.1.2.3 **Current and Charge Distribution**

The last section explained that the MDM has a minimum usable frequency. When the field observation points are close to the sharp bends of the cable structure, the minimum usable frequency decreases. This section identifies the root cause of the failure of the MDM at low frequencies. In doing so, the current distribution at the cable bending location, and the dominant charge distribution over the given cable will be compared using MoM and MDM. Again, the MoM solution is considered as a reference solution.

Figure 5.6 illustrates the current distribution for the MoM approximation (a), and the MDM approximation represented as a set of rectangular functions (or piecewise constant functions [53]) (b) over a cable bend. The cable bend is formed by cable 1 and cable 2, where the end of cable 1 connects to the beginning of cable 2. Cable 1 consists of N segments, where the currents over the last two segments are denoted by $I_{l_1,N-1}$ and $I_{l_1,N}$, respectively, and the related lengths of the segments are $d_{l_1,N-1}$ and $d_{l_1,N}$. The currents for the first two segments of cable 2 are denoted by $I_{l_2,1}$ and $I_{l_2,2}$. The implementation for MoM uses triangular basis functions in the EFIE for cable structures. The segment length dl $(=\frac{d_{l_1,N-1}}{2}+\frac{d_{l_1,N}}{2})$ length shown in Figure 5.6 (b) is a result of segmentation used for MDM.

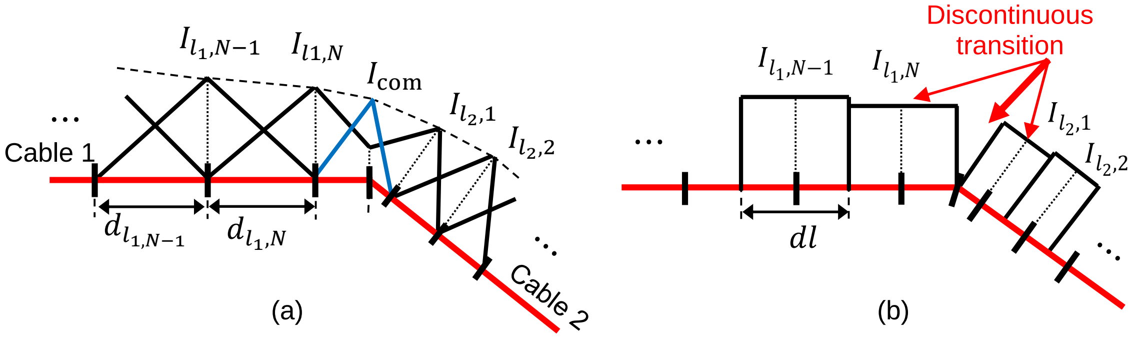

Figure 5.6: Current distribution over the connecting point of the cables. (a) MoM-based on triangular basis functions, (b) MDM.

The reason for the rectangular current distributions is that the MDM is composed of a set of dipoles. From the definition of the dipole moment, it is known that the current density of the segment only exists at the middle of the segment due to the involved Dirac function (see chapter 3 section 3.6). It is a good approximation to assume a constant current within the segment, as long as the segment length is short enough. By comparing the current distribution between (a) and (b), a continuous current distribution can be observed in (a). An additional triangular basis function (I_{com}) is therefore introduced at the bending point (the end of cable 1 and the beginning of cable 2). It ensures a continuous current flow from cable 1 to cable 2. A discontinuous transition at the bend can be observed in subfigure (b) due to the change of the current direction.

The charges also need to be considered since they dominate the field at low frequencies (see chapter 4, section 4.2.4). For MoM, chapter 3 (Figure 3.9 (b)) describe the charge density ρ_{l_n} for the current I_n over the n^{th} triangular basis function as a rectangular block. The rectangular block is shown again in Figure 5.7 (a). According to (3.52), the residual of the charge density distribution ρ_{res} over the segment length dl ($=\frac{dl_{n-1}}{2}+\frac{dl_n}{2}$) is a summation of the charge density over both the rising and the falling edge [53], which can be expressed as:

$$\rho_{\mathrm{res}}(dl_n)=\frac{j}{\omega}\frac{I_{n+1}-I_n}{dl_n}. \tag{5.1}$$

The same ρ_{res} is also illustrated in Figure 5.7 (b) for MDM. The location of the charge density distribution is slightly shifted in the figure for better visualization. To simplify the interpretation, assume the segment length is $dl_{n-1}=dl_n$. Therefore, the discrete charge density ρ_{l_n} over the segment length dl can be written as:

$$\rho_{l_n}=\frac{j}{\omega}\frac{dI_n(z')}{dz'}=\begin{cases}\frac{j}{\omega}I_n\delta(z') & \text{for } z'=-\frac{dl}{2};\\ -\frac{j}{\omega}I_n\delta(z') & \text{for } z'=+\frac{dl}{2}.\end{cases} \tag{5.2}$$

As a result, the ρ_{res} represented by the term ρ_{l_n} from (5.2) is discrete, which leads to problems with the numerical treatment. When using the current distribution on the cable structure for MDM creating (see Figure 5.1), a distribution of residual charges (determined by ρ_{res} obtained from (5.1) and (5.2)) will be created, which results in E_z field component (orientation see Figure 5.1).

Due to the residual charge distribution, more basis functions are required for a better representation of the current (charge) distribution; in other words, much more dipoles are required for MDM than basis functions in MoM to get better modeling accuracy.

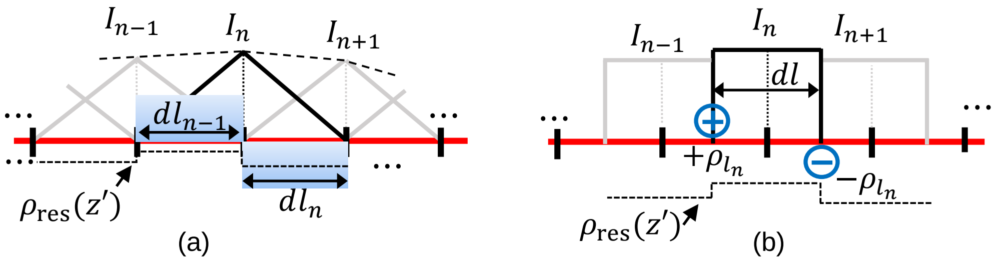

Figure 5.7: Charge density along a cable for (a) MoM and (b) MDM (charge density is shifted for better visibility).

It can be derived from the above considerations that the discontinuous transition at the sharp bending and using too few dipoles cause the error in the MDM. The accuracy of the calculated electric field was expected to improve if more dipoles at the transition were added to model the continuity of the current flow. To verify that assumption, the model in Figure 5.3 was utilized again. The cable was terminated with 5 Ω and the source impedance was chosen to 5 Ω. This is a critical case. The influence of the number of dipoles on result accuracy was investigated. The field observation point was set at 1 m distance with a 0.1 m shift in x-direction (x = -0.1 m) from the cable center. Figure 5.8 illustrates E_{vertical} calculated from MDM with a different number of dipoles.

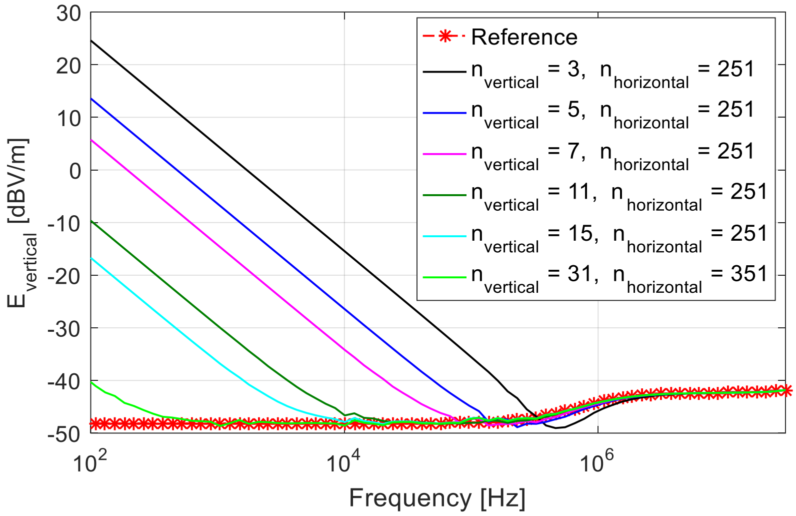

Figure 5.8: Accuracy of the electric field is associated with the number of dipoles used in the MDM.

In the figure, the field from the MoM calculation (red curve) is the reference. The star markers indicates the simulated frequencies. $n_{vertical}$ and $n_{horizontal}$ denote the number of dipoles used in the MDM. Using more dipoles for the MDM creation improved the accuracy of the MDM at low frequencies. For example, the minimum usable frequency can be shifted from more than 100 kHz to less than 1 kHz when comparing the black curve ($n_{vertical}$ = 3 and $n_{horizontal}$ = 251) and the green curve ($n_{vertical}$ = 31 and $n_{horizontal}$ = 351). However, the measurement time will be very long for such a large number of dipoles. The additional effects of measurement and positioning errors need to be considered too.

5.1.2.4 Current Amplitude and Phase Distribution

The current distribution along cable structure needs to be known for MDM creation. The accuracy of the current distribution can influence the accuracy of the MDM field estimation. Figure 5.9 illustrates the structure used for investigation. The structure was stimulated with an ideal current source I_S of 1 A, and Z_L varied from 10 Ω to 1 kΩ. More dipoles are required to improve the low frequency accuracy of MDM. Hence, for this investigation, 15 dipoles were set for each vertical section represented by wire 1 and wire 3, and 251 dipoles were set for wire 2 to create the MDM.

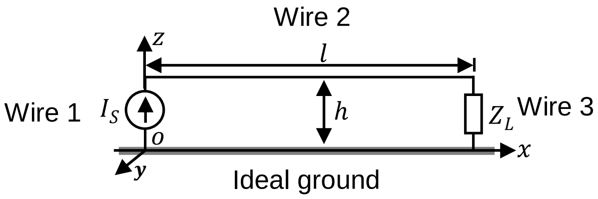

Figure 5.9: Configuration to analyze the current distribution.

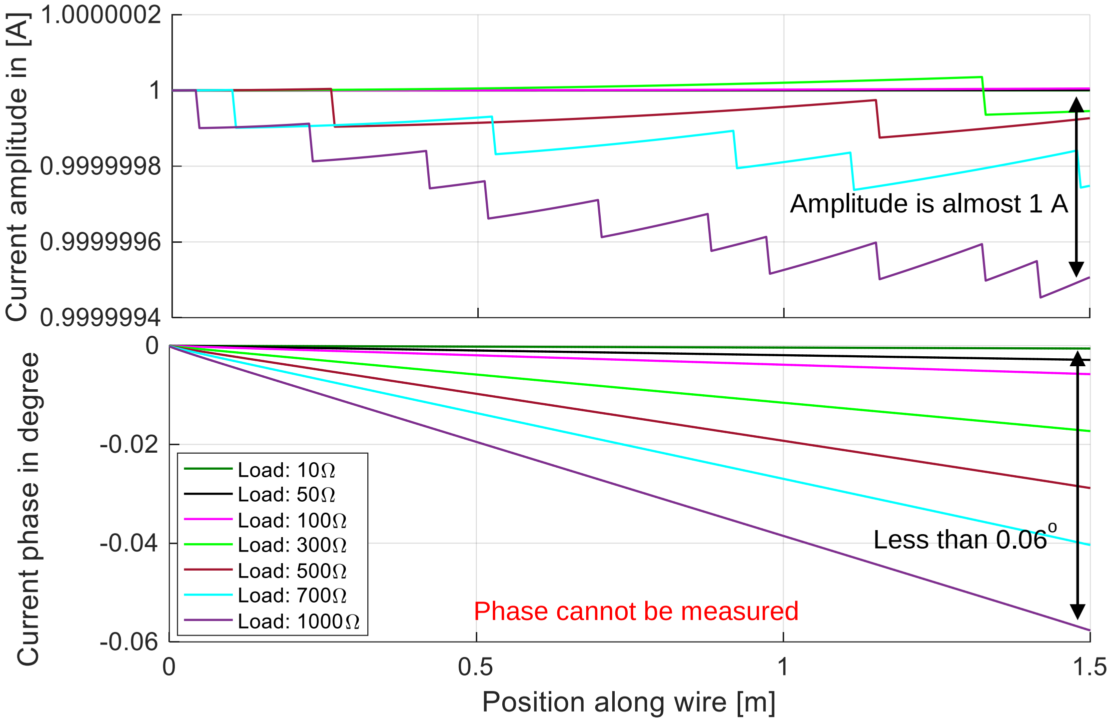

Figure 5.10: Current amplitude and phase distribution at 10 kHz.

The current distribution along wire 2 at 10 kHz is illustrated in Figure 5.10. The current amplitude is almost constant of 1 A (shown in the upper figure), and the phase variation along the wire (shown in the bottom figure) is less than 0.06°, which is a value that cannot be measured without extraordinary effort. The steps in the current amplitude curves are from the numerical solution. According to (5.1), the charge density distribution can be determined, but the numerator $(I_{n+1} - I_n)$ of the expression tends towards zero. However, it has a relevant, non-zero value. The numerator $(I_{n+1} - I_n)$ is hard to determine if measurement data is used. Noise from the measurement dominates. Furthermore, ω is included in the denominator. The factor $(1/\omega)$ leads to a magnification for the charge density distribution if the frequency is reduced. Hence, for low frequencies, it is almost impossible to use measured data for MDM creation.

As the variation of the phase is very small (less than 0.06°), arguably no phase is required at low frequencies for MDM creation. To check if the MDM works without phase distribution, the field observation point was set at 1 m distance facing the center of wire 2 and 10 cm above the ideal ground. To avoid the field cancellation over the symmetry plane of the structure, the field point was shifted 10 cm in x-direction. Figure 5.11 compares E_{vertical} for two cases: the MDM is first created with the accurate varying phase and then with a constant phase. The figure illustrates first the remarkable difference between MoM and MDM; the deviation is caused by the limited usable frequency range of MDM. Above 1 kHz, the electric field generated by the MDM based on amplitude data with constant phase (the dashed black curve) is far away from the MoM reference solution. When phase is considered (blue curve) above 1 kHz the MDM is quite accurate. Although phase variation is very small, the influence is very large.

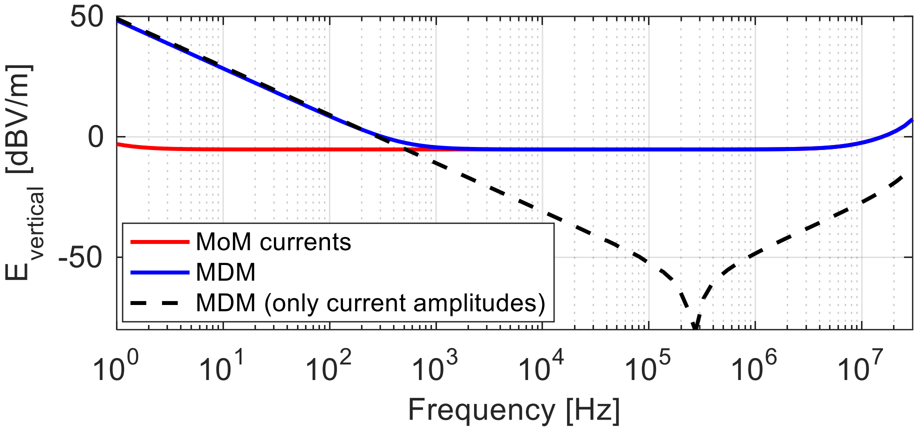

Figure 5.11: $E_{vertical}$ calculated with MDM and correct amplitude and correct phase function (MDM), and correct amplitude but constant (wrong) phase (only current amplitudes).

In Figure 5.12, the current shape for 1 MHz is shown. The magnitude is nearly a constant of 1 A. However, the phase changes by about 6º. Although the variation depends on the termination conditions, the phase variation can already be measured using a standard current clamp measurement setup.

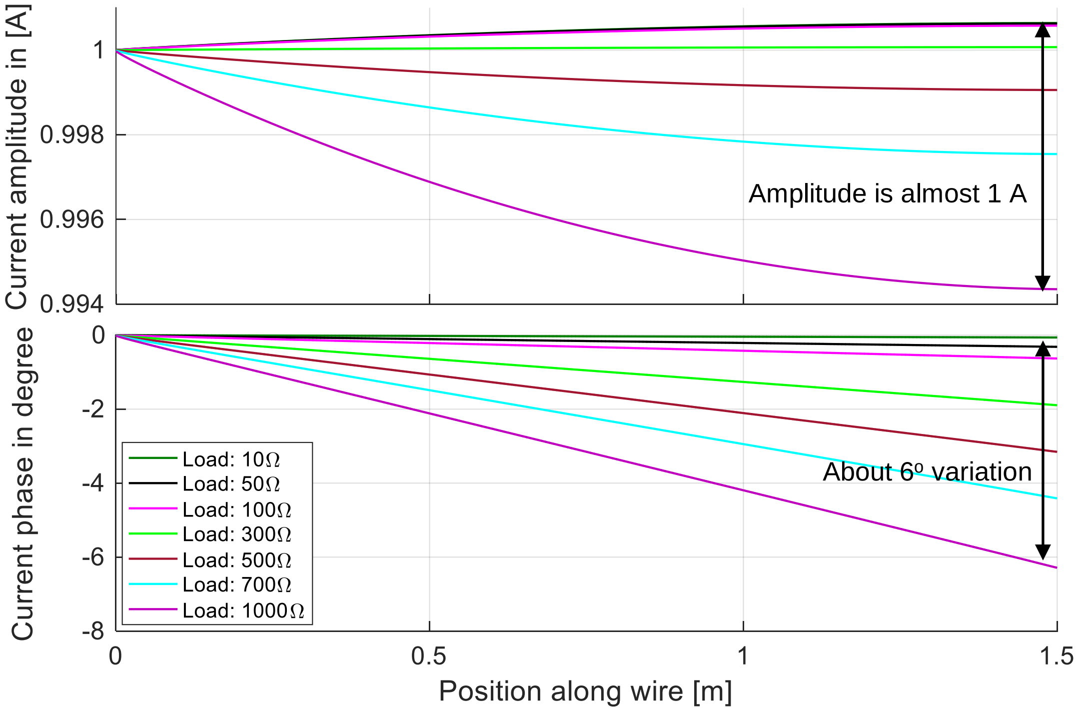

Figure 5.12: Current amplitude and phase distribution at 1 MHz.

This raises an interesting question: Even if the current can be measured exactly, how sensitive is MDM to phase errors? The configuration in Figure 5.3 was again investigated, and terminations of 50 Ω were selected. To simulate the phase error, a uniformly distributed random phase noise with a mean value of zero was added to an “ideal” current distribution extracted from MoM (CONCEPT-II calculation). The field observation point was 1 m away from the center of the structure and 10 cm above the ideal ground. Figure 5.13 illustrates E_{vertical} (the upper figure) and $E_{\text{horizontal}}$ (the bottom figure) as the phase errors influence the calculated electric field. The labels are associated with different levels of maximum phase perturbations; for example, $\pm 20°$ means the phase noise is between $+/-\ 20°$. The markers in the figure indicate the simulated frequency points. Only one group of random numbers was generated for this investigation to show a simple visualization of the effect of the noise in the phase data. The effect of the phase noise decreases with increased frequency. Especially above 10 MHz, the deviations of E_{vertical} mainly occur at the minimums. Here the variations are not important in EMC. At low frequencies, the curves show dramatic deviations up to 10 MHz for both vertical and horizontal field components. For example, for the vertical field component, where $\pm 3°$ phase noise (magenta curve in the top figure) causes more than 10 dB deviation at 1 MHz compared with the result from MoM. Furthermore, there is a large offset of $E_{\text{horizontal}}$ at very low frequencies when only $\pm 1°$ phase noise level is added.

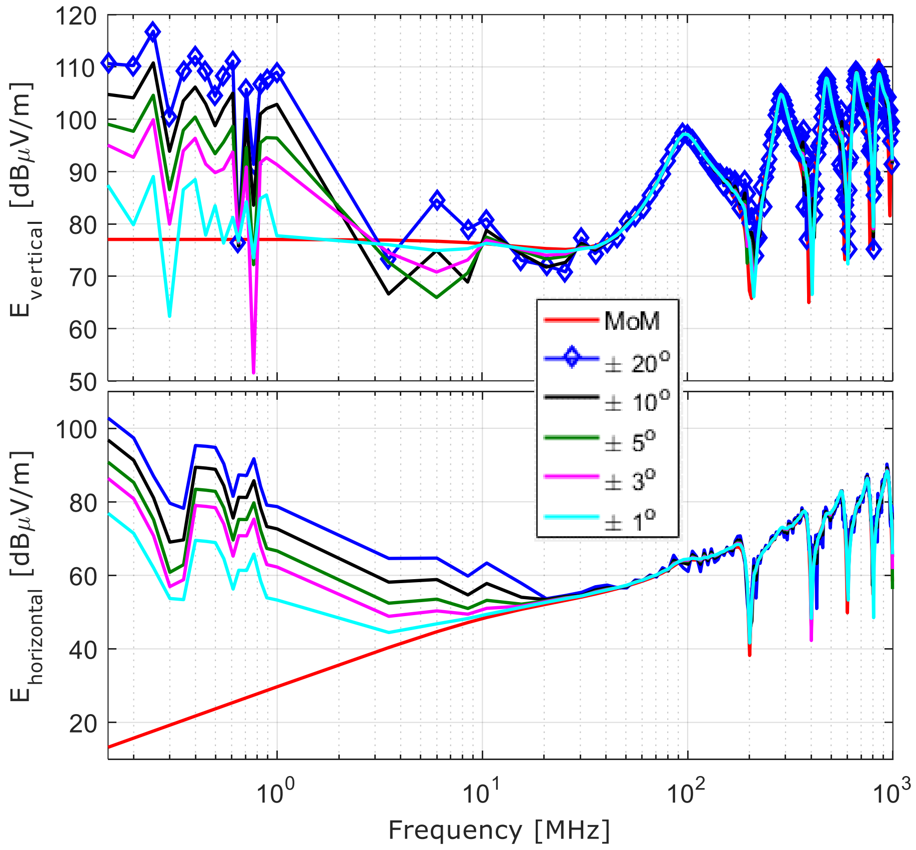

Figure 5.13: Influence of phase error on the calculated electric field.

The results can be summarized shortly. The first research question can be answered. Firstly, the MDM method gives worse estimated electric fields if measured common-mode current data is used as an input variable. Secondly, theoretical improvements are possible by increasing the number of segments, especially in the regions in which the current direction changes. Thirdly, if measured common-mode current data is applied, which means many measurements are required to be done, and each of them must be able to resolve very small differences. Nevertheless, this cannot be realized due to the limitation of measurement accuracy. Therefore, in practical applications electric fields cannot be predicted from currents at low frequencies.

5.2 Electrical Field Integral Equation

The EFIE introduced in chapter 3 provides another possibility for electric field calculation when the current distribution of a source structure is known (see formula (3.38)). The formula (3.38) can be directly applied to CISPR 25 measurement setup when the current distribution over the cable structure is known. By applying triangular basis functions, the formula (3.38) was expressed as (3.54). An example was already described in chapter 4 section 4.2.4, where the current distribution extracted from CONCEPT-II was used. In real setups, the common-mode currents can be captured, e.g., using a current probe (described in section 5.1). However, it was noted in section 5.1 that EFIE works accurately only with a precisely given current distribution along the cable structure. At low frequencies, the charge distribution dominates the electric fields; when applying measured currents, no precise currents can be obtained due to the limited measurement accuracy, and charge distribution cannot be calculated. Therefore, EFIE will fail if it is applied to real setups for electric field estimation. This method will not be discussed further.

5.3 Static Dipole-Based Method

As described in chapter 3 section 3.7, when the frequency is very low, the frequency dependency of a current distribution can be neglected. The Hertzian dipole can be considered as a static dipole, which provides another possibility of electric field estimation. The static dipole is therefore introduced and described in detail in the following sections.

5.3.1 Motivation for Static Dipoles

It is known that the electric field is a contribution of both the electric current and the electric charge on a cable structure. This can be seen, e.g., in the electric field integral equation in (3.32). In chapter 4, section 4.2.4, this relation was verified, and it was pointed out that the contribution of charges dominates the electric field particularly in the very low frequency range.

From a theoretical point of view, it is possible to predict both electric and magnetic field exactly by using a set of Hertzian dipoles based on the current distribution in the cable structure for the whole frequency range (MDM). However, in real applications, the limited accuracy of current measurements (related to discretization and current magnitude/phase along the cable structure) limits the accuracy of MDM at low frequencies (see chapter 5 section 5.1.2).

To overcome the limitations, a static dipole approach can be applied to predict only the electric field from a cable. The reason is that only the electric field is interesting in CISPR 25 measurement setups at low frequencies since the rod antenna is mainly sensitive to the electric field). At the same time, the magnetic field can be neglected (see chapter 4, section 4.3). This approach does not provide a general solution and can only be applied to the specific setup at low frequency range in the electric near-field. Neglecting the current can introduce an error at higher frequencies.

To emphasize the idea of using only static dipoles, Figure 5.14 shows the arrangement of a static dipole in comparison with a Hertzian dipole applied to a cable segment over a conductive ground plane and applied image theory. The Hertzian dipole requires the current in the segment and should be arranged in the direction of the physical path of the current. In comparison, the static dipole, or better to say the charge in a segment, is placed at the physical position of the wire segment. By applying the image theory, a static dipole is formed.

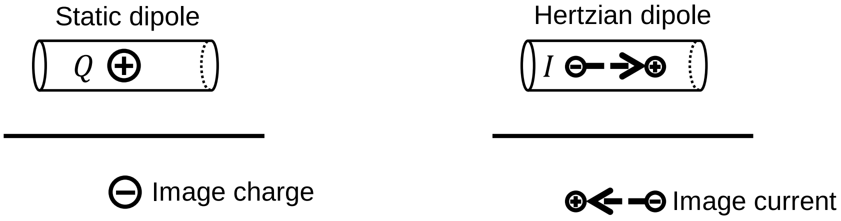

Figure 5.14: Comparison of the arrangement of a static dipole and a Hertzian dipole in a cable segment.

In case of a time-dependent excitation, the static dipole does not consider any changing current flow. It only considers the amount of charges and whether the charge is positive or negative in the segment related to the time dependency.

Based on the continuity equation, the charge density inside a volume, in this case, the cable segment, depends on the amount of charges per time (current) which flows into the segment and which flows out of the segment (neglecting the displacement current for simplification). Therefore, the segment is assumed to be a point charge.

5.3.2 Static Dipole-Based Model

Figure 3.11 shows the calculation of the electric field from a static dipole. In Figure 5.15, subfigure (a) illustrates a charged cable segment parallel to the x-axis. The plane $z = 0$ is the infinite PEC-ground plane. The cable segment has a length of Δl and is placed above the ground at a height of h. ρ_l is the area charge density over the cross-section of the segment. The vector $\vec{r}_i$ points to the middle of the segment. Subfigure (b) illustrates a static dipole model for the cable segment, where the distance between the positive and the negative charge is $2h$. The position of the static dipole is in the middle of the cable segment. The total charge of the cable segment Q can be obtained by $\rho_\mathrm{n}\Delta l$, if the cable segment is short enough such that the charges over the segment have a uniform distribution and the area charge density is constant over the cross-section of the segment.

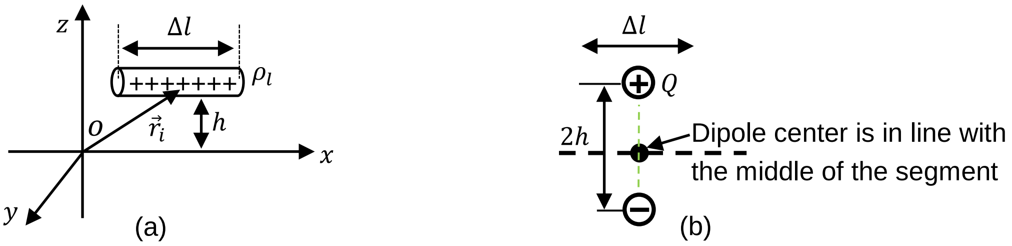

Figure 5.15: Static dipole-based model for a charged cable segment over the ground (plane z = 0). (a) the cable segment is of length Δl, placed above ground at height of h, (b) the static dipole model, where the ground influence is replaced by a negative charge.

5.3.3 Field Estimation Using Static Dipoles

Now a set of static dipoles is used to model the cable of a typical CISPR 25 setup. Figure 5.16 shows the static dipole-based model. Subfigure (a) illustrates the cable structure with positive charges. The cable structure is divided into N short segments, where the length of each segment is $\Delta l (= l/N)$. Subfigure (b) shows the static dipole model, where N dipoles are used. The negative charges are used to reproduce the effects of the ideal ground. The dipole centers correspond to the related center of the segments.

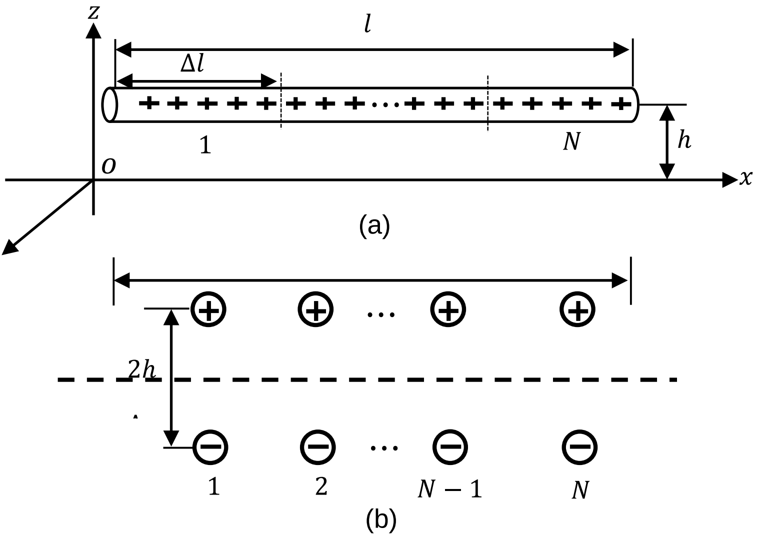

Figure 5.16: A static dipole-based model for cable structure of a CISPR 25 setup. (a) the cable structure above ideal ground, (b) the static dipole model.

The charge density distribution along the cable can be found through near-field measurements, e.g., with an electric field probe. Based on the measured electric fields, the charge density distribution can be calculated by using (5.4) based on the assumption that the segment length Δl can be considered as infinite when compared with the distance between the segment length and the field observation point. With the obtained charge density distribution, the vertical component of the electric field ($E_{z,n}$) for n^{th} cable segment can be obtained using (3.71) under the condition that $\theta = 90^o$. The contribution of all the cable segments gives the total electric fields:

$$E_z = \sum_{n=1}^{n=N} E_{z,n}. \tag{5.3}$$

To investigate the accuracy of the static dipole model, the parameter settings of the equivalent circuit model (see chapter 4, section 4.4.4) were used again. The cable was divided into four segments, where each segment has a length of 0.375 m. The four cable voltages are related to the charges ($Q_1, \dots, Q_4$), extracted from the equivalent circuit model, were used for creating the four static dipoles to estimate the electric fields.

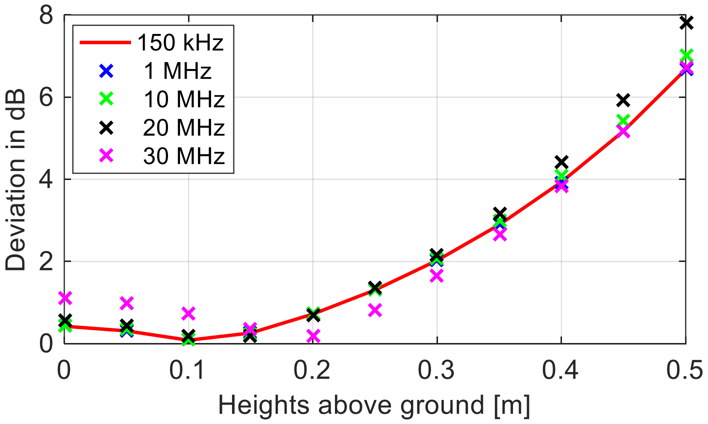

Figure 5.17: Comparison of the vertical component of the electric field from CONCEPT-II and calculation based on the static dipole model, where the field observation points face the middle of the cable, and 1 m distance to the cable, and at different heights above the ideal ground.

Figure 5.17 illustrates the absolute deviation of the vertical component of electric fields (E_z) in dB between the static dipole model and CONCEPT-II. The field observation points were set at the rod antenna location (1 m from the cable center) and different heights above the ideal ground. The results at 150 kHz, 1 MHz, 10 MHz, 20 MHz, and 30 MHz are shown. The figure shows that the observed deviations are less than 2 dB when the heights of observation points are less than 0.3 m. For the observation point at the height of 0.1 m, almost no deviation is observed for most represented frequencies. Even for the frequency at 30 MHz, the deviation is less than 1 dB.

Figure 5.18 shows the deviations when the field observation points are set to be above the ideal ground of 0.1 m and at different distances from the cable center. The arrow marks the field at a distance of 1 m and shows the maximum deviation is less than 1 dB for all the observed frequencies. However, the deviations increase with cable's decreasing distances. When the observation points are close to the structure, the length of the cable segments $dl(= 0.375$ m) are too long compared to the distance R from the observation point to the static dipole source, for example, at 0.2 m. Therefore, they cannot be considered as the cable segments having constant voltage potentials. As a result, the four static dipoles are not sufficient for modeling. Here, for CISPR 25 setups, the distance is fixed at 1 m. Hence, the static dipole model still works with an acceptable deviation for the low frequency range.

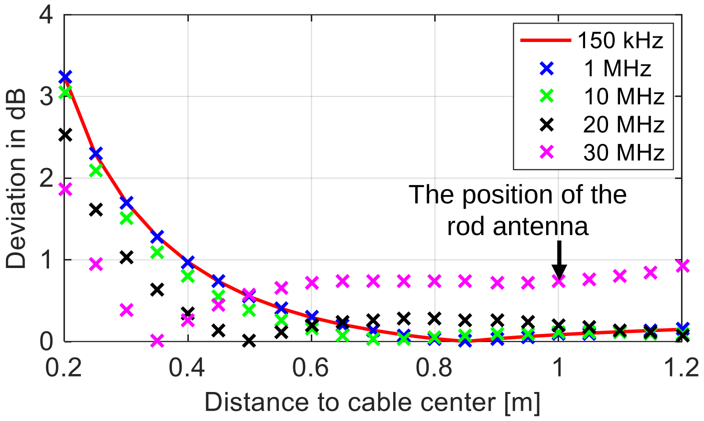

Figure 5.18: Comparison of the vertical component of the electric field from CONCEPT-II and calculation based on the static dipole model, where the field observation points facing the middle of the cable structure, at 10 cm above the ideal ground, and different distances to the cable center.

5.4 Huygens Principle-Based Method

In chapter 1, the Huygens principle was described as a method for near- and far-field calculation. The idea is to use only some local near-field measurements and to construct the field points on a Huygens' surface. In chapter 3, the derivation of the principle was detailed described. It pointed out that applying the Huygens principle to electric field calculation, both electric and magnetic current sources $\vec{J}_{\mathrm{eq}}$ and $\vec{M}_{\mathrm{eq}}$ over the Huygens' surface should be known. When the field region outside of the Huygens' surface is needed, the inner region of the Huygens' surface can be assumed to be null field. Furthermore, if an infinite planar Huygens' surface (closed in the infinite) and is filled with PEC/PMC, only $\vec{M}_{\mathrm{eq}}/\vec{J}_{\mathrm{eq}}$ distribution is required.

Usually, a closed surface should be defined, e.g., described in [13]. However, closed Huygens' surfaces are often not preferred for practical applications due to the requirement of a complex field scan system. In this work, an open Huygens' surface (a truncated Huygens' surface instead of a closed Huygens' box, already described in [89],[90],[91]) is proposed to reduce the measurement efforts. To reduce the measurement effort further, a planar Huygens' surface, assumed to be filled with PEC, can be applied (described in chapter 3 section 3.2). Then, only E-field measurements on the surface are required. According to the Huygens principle, determination of $\vec{M}_{\text{eq}}$ requires E-field distribution ($\vec{E}_S$) over the Huygens' surface (see equation (3.8)). By applying PEC and the image theory to the Huygens principle (surface equivalence theorem), $2\vec{M}_{\text{eq}}$ as the equivalent current source is required for field calculation[8] at any arbitrary observation point. There is no need to apply $\vec{J}_{\text{eq}}$ and therefore no need to measure the H-fields. The simplification method will be applied in this section for electric fields prediction. Furthermore, it will be shown that both electric and magnetic fields can be calculated with only the equivalent magnetic current densities $\vec{M}_{\text{eq}}$ on the Huygens' surface.

It will be shown that only the field distribution in selected discrete locations is needed for calculating the electric fields. The CISPR 25 setup is placed on the metallic table. The main field source is the cable bundle, and only the electric fields in the front of the setup are of interest. Hence, a closed Huygens' surface is in actual not necessary. Furthermore, the proposed method only needs near-field measurements at several locations along the cable above the metallic table, and only one component of the electric fields is required for obtaining the $\vec{M}_{\text{eq}}$ distribution on the Huygens' surface. The reduction of the measured near-field data can cause some inaccuracy in the estimated electric fields, which will be discussed in section 5.4.2.

5.4.1 An Open Huygens' Surface

As mentioned above, an infinite planar surface is introduced as the Huygens' surface. By applying the Huygens principle in combination with the image theory and introducing a PEC, $2\vec{M}_{\text{eq}}$ as the equivalent source on the surface can represent the original sources and gives the correct field result at any arbitrary observation point in front of the surface. However, for real applications, an infinite planar surface is not applicable. In this work, a truncated plane as an open Huygens' surface is introduced, instead of an infinite planar surface. An assumption is that the equivalent sources on the truncated area mainly contribute to the fields. The other area of the infinite surface contributes minimal to the fields and therefore can be neglected. By truncating the surface, a small error in the predicted fields should be expected.

The open Huygens' surface has already been introduced in Figure 1.4 (c). The surface is in the front of the cable bundle. Red arrows indicate the locations, where the near-field measurements can easily be performed. To obtain the equivalent current sources over the Huygens' surface, the measured data has to be interpolated to obtain fields at points between the measurement locations (represented by green arrows). Next, an extrapolation has to be performed to obtain the fields at the other locations on

---

[8] In this case $\vec{J}_{\text{eq}}$ has to be assumed to be zero.

the Huygens' surface (represented by blue arrows). With this information, the electric field at the rod antenna location can be estimated.

Figure 5.19 shows a simplified setup used to investigate the accuracy of the open Huygens' surface. The model was created and simulated using MoM. To save simulation time and to reduce model complexity, an infinite PEC ground plane replaces the metallic table. A single-wire cable represents the attached cable structure.

As shown in Figure 5.19 (a), the reduced Huygens' surface (dashed red outline) has the following dimensions: 3 m long, 1 m high, and the bottom of the surface touches the infinite PEC-ground. The cable is 1.5 m long, and both ends of the cable have the same distance to the edge of the Huygens' surface. The field reference point is located at a distance of 1 m from the center of the cable. A source V_S with an impedance of Z_S = 50 Ω is used. Z_L varied. 10 Ω, 50 Ω, 330 Ω, and 10 kΩ were chosen to investigate the effect of different terminations. The Huygens' surface is located 5 cm in front of the simplified measurement setup (see Figure 5.19 (b)).

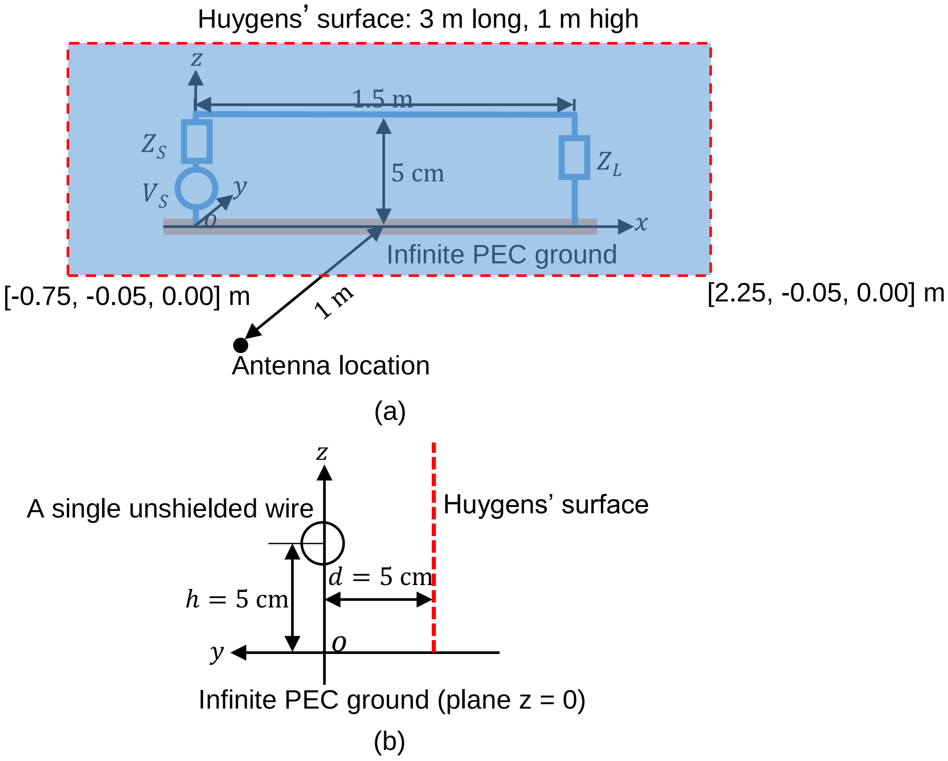

Figure 5.19: Simplified measurement setup. (a) A single-wire cable over the infinite PEC-ground, driven by an ideal voltage source V_S, with source impedance Z_S and load impedance Z_L, also the location of the defined Huygens' surface is shown; (b) Side view, which shows the relative position of cable and the Huygens' surface.

Figure 5.20 shows the simulated vertical polarized electric fields at an observation point (1 m distance to the cable structure and 5 cm above the infinite PEC ground). For all simulated termination impedances, dashed lines show Huygens principle-based predicted fields using the defined surface. It should be noted that here both $\vec{M}_{\mathrm{eq}}$ and $\vec{J}_{\mathrm{eq}}$

are used for the electric field calculation. The purpose is to show that when both $\vec{M}_{\mathrm{eq}}$ and $\vec{J}_{\mathrm{eq}}$ are applied on a truncated planar surface (not an infinite planar surface), the Huygens principle works with an acceptable error. The fields were calculated by using the methods described in chapter 3 section 3.5. The algorithm was implemented in MATLAB (see Appendix F).

In the figures, MoM-calculated (CONCEPT-II) results are considered as reference fields. The solid lines show the full-wave simulation results from MoM. Both results match with less than 0.5 dB deviation, indicating the correct implementation of the Huygens principle and supporting the simplification of only using a truncated plane. So, one main research question (introduced in chapter 2) can be answered. The Huygens principle can be applied at low frequencies with only a single truncated surface.

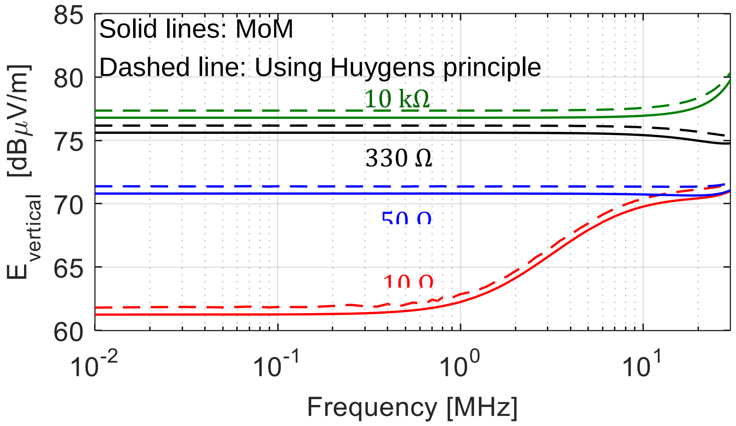

Figure 5.20: E-field calculated using the truncated open Huygens' surface with both $\vec{M}_{\mathrm{eq}}$ and $\vec{J}_{\mathrm{eq}}$. The cable was terminated with different load impedances. Deviation results from the truncated surface.

The configuration of the 50 Ω load impedance case in Figure 5.20 is used to further investigate the case where only E-fields are applied on the Huygens' surface ($2\vec{M}_{\mathrm{eq}}$ and $\vec{J}_{\mathrm{eq}} = 0$). The field observation point, the Huygens' surface size, and the location are the same as used for calculating the result shown in Figure 5.20.

Figure 5.21 shows all E-field components (subfigure (a)) and all H-fields (subfigure (b)) at the observation point. For both subfigures, the solid lines give the CONCEPT-II simulation result, representing the reference. The dashed lines with markers give the results where only $2\vec{M}_{\mathrm{eq}}$ is applied on the Huygens' surface. It can be seen that all important E-field components match well with the reference. The z- and y-component of the H-field are in line with the reference too. It can be observed that the H_x does not yield the correct result. This deviation can be caused by the truncated surface and the discretization[9]. As H-field is not required in this work, this deviation was not investigated further.

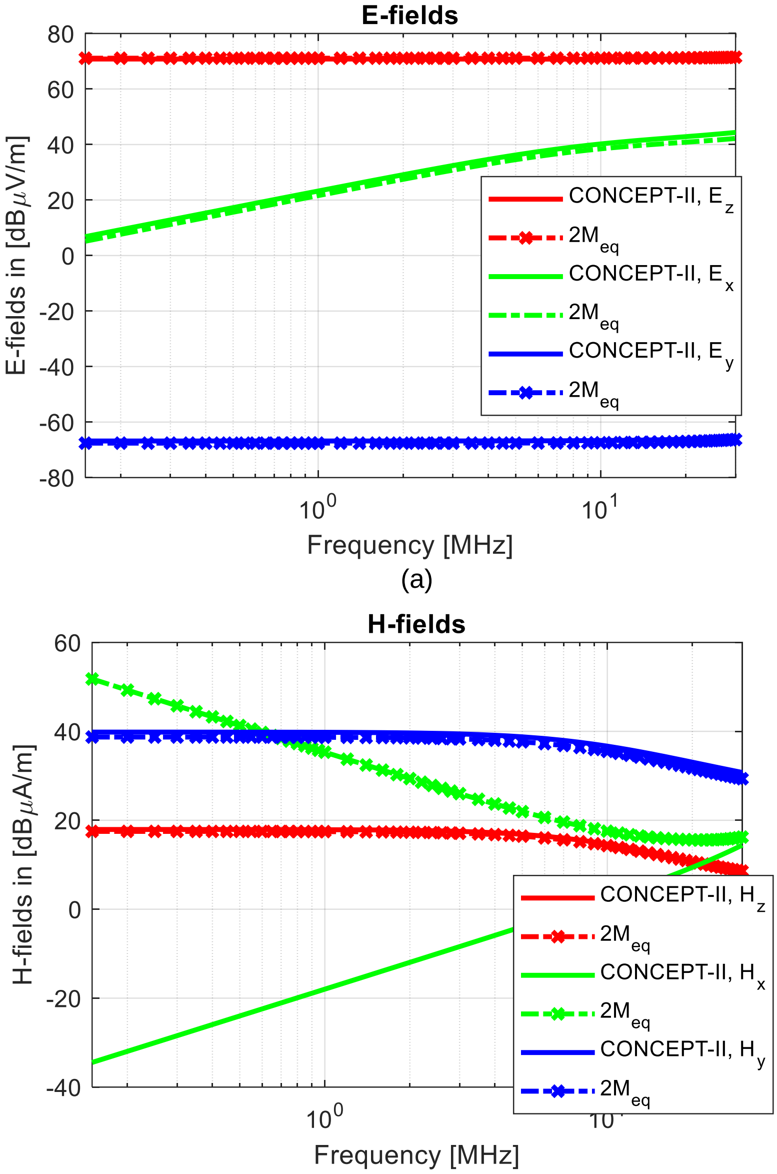

(a)

(b)

Figure 5.21: Comparison of E-fields and H-field when using only $2\vec{M}_{\mathrm{eq}}$ (introduced PEC on Huygens' surface) on the truncated open Huygens' surface for 50 Ω load impedance.

---

[9] To calculate $\vec{H}$, the equation $\vec{H} = \vec{H}_{\mathrm{A}} + \vec{H}_{\mathrm{F}} = \frac{1}{\mu}\nabla \times \vec{\mathrm{A}} - j\omega\vec{\mathrm{F}} - \frac{j}{\omega\mu\varepsilon}\nabla\left(\nabla \cdot \vec{\mathrm{F}}\right)$ is applied (see appendix A, equation (9.33)). As only $2\vec{M}_{\mathrm{eq}}$ is used, the first term $\frac{1}{\mu}\nabla \times \vec{\mathrm{A}} = 0$, and the second term $-j\omega\vec{\mathrm{F}}$ and the third term $-\frac{j}{\omega\mu\varepsilon}\nabla\left(\nabla \cdot \vec{\mathrm{F}}\right)$ are relevant (see equation (3.13)(3.8)). At low frequencies, especially $\frac{1}{\omega}$ in the third term becomes very high. Therefore, as a compensation, $\nabla\left(\nabla \cdot \vec{\mathrm{F}}\right)$ needs to be very accurate. The accuracy depends on the discretization and size of the surface.

5.4.2 Dominant Field Components on the Huygens' Surface

It proved above that by applying the truncated single surface, an acceptable error of the calculated electric fields can be seen. However, it is not so easy to scan all the field components over the defined Huygens' surface with few costs but time-effective. Therefore, the dominant field sources must be investigated, which is done in this section.

It is proven by Figure 5.20 that the assumption adds less than 0.5 dB deviation to the calculated electric fields. Furthermore, to reduce near-field scan time, one can fill the closed surface e.g., with PEC. In this case, only the $\vec{M}_{\mathrm{eq}}$ is relevant, which means only the E-field distribution is required. In this section, the field contribution of each field component over the Huygens' surface will be investigated.

Using the coordinate system defined in Figure 5.19 (a), the tangential field components on the Huygens' surface are E_z and H_z, E_x and H_x. In order to determine which tangential field component has the most significant contribution to the field at the rod antenna location, the simplified setup shown in Figure 5.19 was used and a load impedance (Z_L = 50 Ω) was chosen. Other impedances (10 Ω, 330 Ω, 10 kΩ) were also simulated and have shown similar results with respect to the dominating contribution.

Figure 5.22 shows E_{vertical} at the rod antenna location contributed from different field components over the Huygens' surface (Z_L = 50 Ω); the E_z field component dominates. When only using E_z, the observed error is about 5 dB relative to a full-wave simulation. The contribution from E_x is weak, thus, it is neglected and not shown in the figure. The observed magnetic field components (H_x and H_z) have smaller contributions than E_z component. Thus, the method simplifies further by using only the E_z fields.

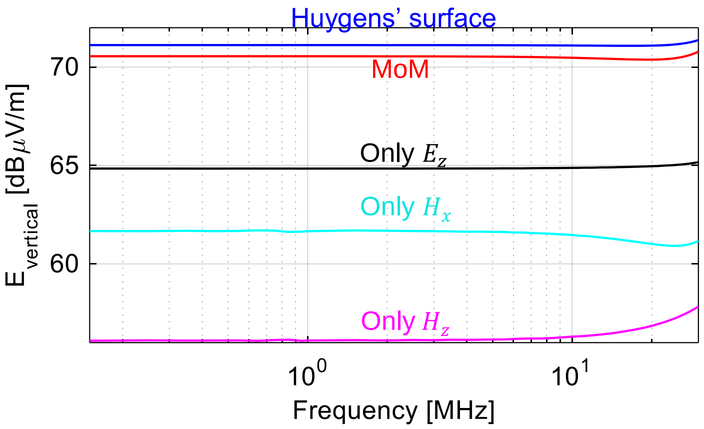

Figure 5.22: Contribution from different field components on the Huygens' surface.

Till now it has been figured out that E_z is the dominant field component. One must consider that measuring magnetic field over a plane should be much easier than measuring electric field. However, one must measure two magnetic field components, as both H_x and H_z are dominant. One the other side, if an infinite PEC-Huygens plane is assumed, only E_z is necessary.

To save near- field scan time, a field extrapolation method will be introduced in the coming section for estimating the E_z distribution. Introducing such simplifications and inter-/extrapolation can result in slight deviations compared to an ideal solution with a large number of measurement points. But the error can be acceptable in EMC measurements.

5.4.3 Field Extrapolation for the Huygens' Surface

To reduce the measurement time only the amplitude of the dominant E_z-field should be measured at several locations above the metallic table. Figure 1.4 (c) shows the measured and interpolated locations). A spline function [92] is introduced for field interpolation. This interpolation is required to obtain sufficient near-field data [93]. Second, to extrapolate E_z for the remainder of the points over the defined Huygens' surface, a quasi-static approximation was used, as described in [94] and [95]. A side view of a single-wire cable is illustrated in Figure 5.23. The cable was placed at a height h above the ground plane, parallel to the *x*-axis in a Cartesian coordinate system. The cable has a radius of a, is infinitely long, and carries a charge density ρ_l. The field approximation can only be suitable for a cable of infinite length; it assumes a quasi-static field. Thus, the observation point must be very close to the cable regarding the wavelength of the frequency of interest. The electric fields from the cable at observation point $P(y_P, z_P)$ can be taken as a sum of the electric field from the cable above ground and the electric field from the image of the cable, which are given by

$$E_z = \frac{\rho_\mathrm{l}}{2\pi\varepsilon_0}\left[\frac{z_P - h}{(z_P - h)^2 + y_P^2} - \frac{z_P + h}{(z_P + h)^2 + y_P^2}\right], \qquad (5.4)$$

$$E_y = \frac{\rho_\mathrm{l}}{2\pi\varepsilon_0}\left[\frac{-y_P}{(z_P - h)^2 + y_P^2} + \frac{y_P}{(z_P + h)^2 + y_P^2}\right]. \qquad (5.5)$$

The comparison between fields approximated using MoM and (5.4) are shown in Figure 5.24 at position x = 0.25 m for frequencies 150 kHz (top figure) and 30 MHz (bottom figure), respectively. The parameter settings are the same as those used in Figure 5.19. The field extrapolation delivers the missing field values along the Huygens' surface. Star markers within the figure indicate points at which the fields are compared. Only E_z magnitude distributions are shown.

Phase information is not captured, the phases of the measured E_z and the interpolated E_z are assumed $0°$. This assumption can be made because the E-field is insensitive to phase distribution at low frequencies. However, for observation points at different heights along the Huygens' surface, a phase shift of 180^{o} occurs due to the cable structure itself, which can be obtained from the equation (5.4) for the extrapolated fields.

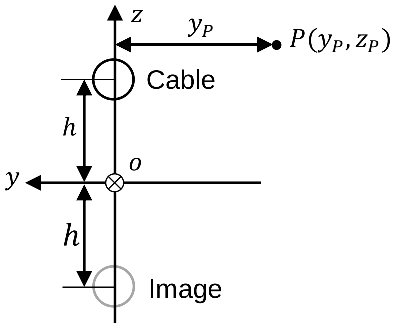

Figure 5.23: The side view of the cable, which is parallel to the *x*-axis, having the charge density ρ_l and is above the ground plane. The image represents the ground effects.

Using the electrostatic approximation is acceptable in the frequency range of interest. Thus, the functional behavior expressed in (5.4) (see Figure 5.24, red curve) can be used for the approximation of the field distributions along the Huygens' surface. By applying only the magnitude of the measured E_z and the interpolated E_z as the start values for the curves, the electric field at the rod antenna location can be predicted.

Since the field observation point is required to be very close to the cable, (5.4) can also be used to indirectly calculate the charge distribution on the cable, which can be achieved by firstly placing an electric field probe close to the cable to measure E_z, then resolving the charge density through (5.4).

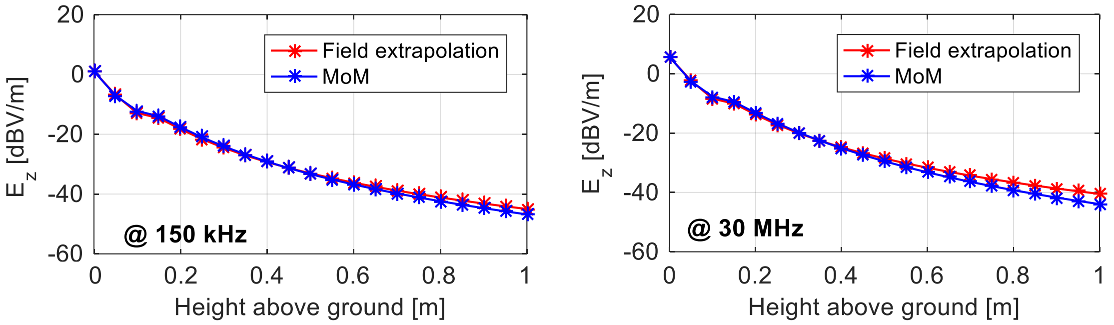

Figure 5.24: Comparison of E_z along the height of Huygens' surface between field extrapolation and MoM result for at 150 kHz and 30 MHz.

With the measured, interpolated and extrapolated E_z-distribution over the defined surface, the equivalent current sources can be calculated using (3.8). The workflow for the Huygens principle-based method is shown in Figure 5.25.

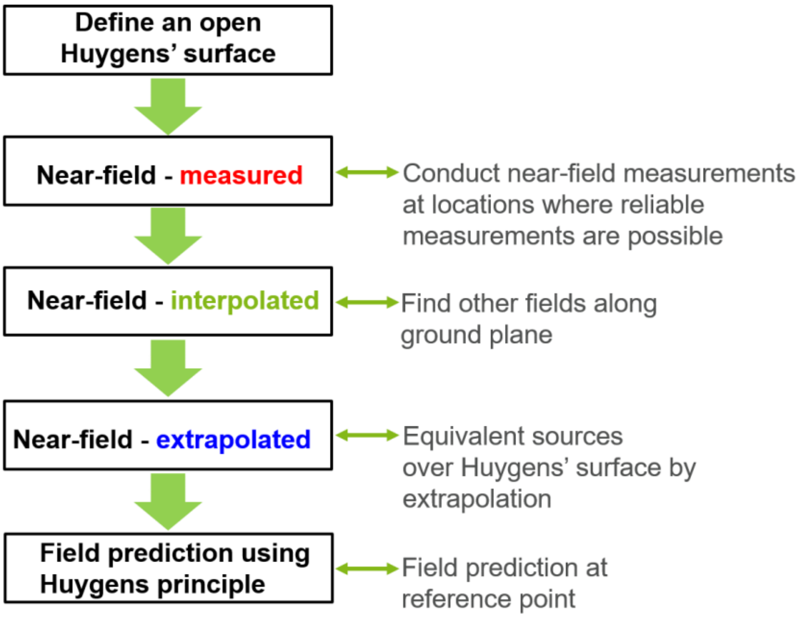

Figure 5.25: Workflow of using the Huygens principle-based method.

6 Measurement of Local E-Field Distribution

It was shown before that the current based field estimation methods must fail at low frequencies due to the high sensitivity against wrong input data unavoidable measurement errors. More promising are E-field based methods like the Huygens principle-based method or the static dipole-based method. Both methods require local E-field measurements. In this chapter, the used measurement approach is described.

6.1 Electric Field Probe

Probes for measuring RF electric and magnetic fields were intensively investigated, for example in [96]. Some probes can be used well for near-field scans. Often small dipole/monopole structures are used to measure the electric fields. In this work, a monopole probe was applied that is known to provide very robust results. The characteristics of the probe can be analyzed using the theory described in chapter 4.

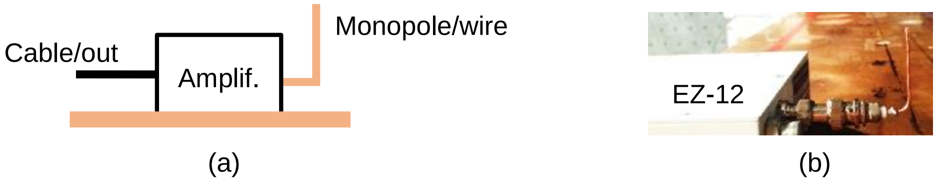

(a) (b)

Figure 6.1: Electric field probe, (a) sketch, (b) photo.

The used probe is illustrated in Figure 6.1. A special antenna amplifier with very high input impedance (R&S EZ-12 [97]) provides a high impedance as the load for the monopole/short wire. The amplifier provides a 50 Ω output impedance for direct connection to 50 Ω measurement equipment.

Before conducting near-field measurements, the field probe (see Figure 6.1) needs to be calibrated. Small electric-field probes can be calibrated using a TEM cell [98] or based on a calibration structure [99]. In this work, the size of the antenna amplifier significantly disrupts the E-field distribution inside the TEM cell. Therefore, a small calibration structure is used to calibrate the field probe, shown in Figure 6.2. In contrast to a TEM cell, it is not possible to calculate the field analytically for this structure. For that reason, a numerical solution from CONCEPT-II is used to determine the field at the probe's location. The probe factor (P_f) can be simply defined by, e.g., in [99]:

$$P_\mathrm{f} = \frac{E_\mathrm{simu}}{V_\mathrm{Ant}}. \tag{6.1}$$

where V_{Ant} is the output voltage of the antenna amplifier when the field probe is placed in the calibration structure. E_{simu} is the field at the observation point obtained from the simulated calibration structure.

In Figure 6.2 subfigure (a) shows a sketch of the calibration structure. It consists of an unshielded cable of 15 cm length placed 1 cm above the ideal PEC ground. The radius of the cable is 1.5 mm. Both source impedance Z_S and load impedance Z_L are 150 Ω. The field observation point is at [7.5, -5.0, 0.0] cm, which has 5 cm distance to the cable, and directly over the PEC ground. Only E_z $(= E_{\mathrm{simu}})$ is considered for calibration. Meanwhile, the field probe is placed 5 cm away from the cable in the calibration structure (see subfigure (b)), and then, the V_{Ant} can be obtained. Applying the formula (6.1) the probe factor can be determined.

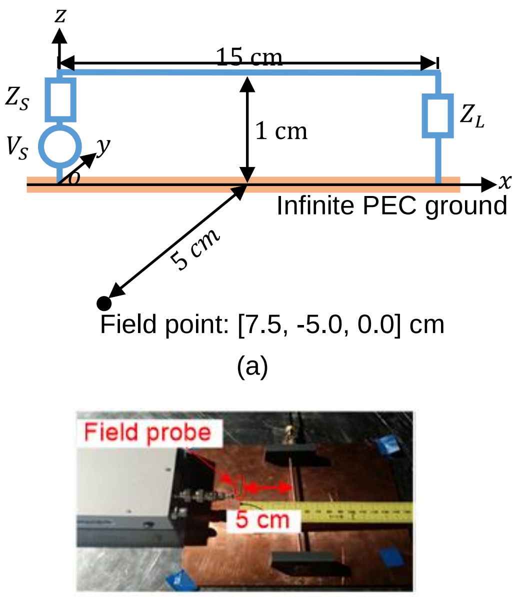

(a)

(b)

Figure 6.2: Field probe calibration, (a) A sketch of the calibration model, (b) Probe in calibration (picture).

6.2 Accuracy of Field Measurements in a CISPR 25 Setup

Near-field measurements in CISPR 25 setup were conducted with the E-field probe, as shown in Figure 6.3. A single-wire cable with a length of 1.5 m was positioned 5 cm above the ground and terminated at one end with 50 Ω. The other end was fed by the tracking generator mode of a test receiver (R&S ESPI 3 [100]). The electric field probe was moved along with the cable, and the antenna voltage was measured with the test receiver input.

Using the probe factor P_{f} obtained from the calibration, the measured electric fields can be determined. As an example, the electric fields (vertical field component, E_z) at 150 kHz, 1 MHz, 10 MHz, and 30 MHz are represented in Figure 6.4. The red curves were obtained by CONCEPT-II and can be considered as reference fields. The point markers on the curves specify the measurement positions of the field probe along the cable length. The data indicates a 3 dB higher measurement value for 150 kHz and 1 MHz. For 10 MHz and 30 MHz, the measured results are in line with the simulated data having a deviation of only 1 dB. The 3 dB deviation at low frequencies might be caused by the different field shapes in calibration and measurement since the electric field used for calibration is different compared with the electric field in the CISPR 25 measurement setup.

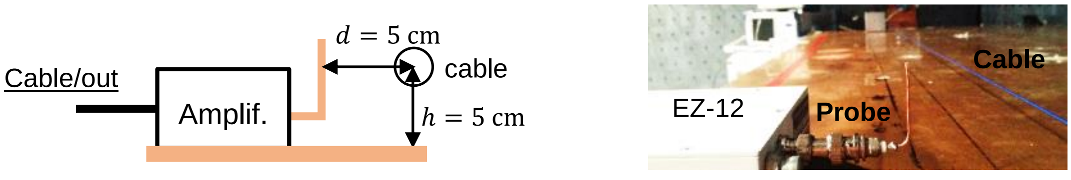

(a) (b)

Figure 6.3: Setup of near-field measurements, (a) sketch, (b) photo.

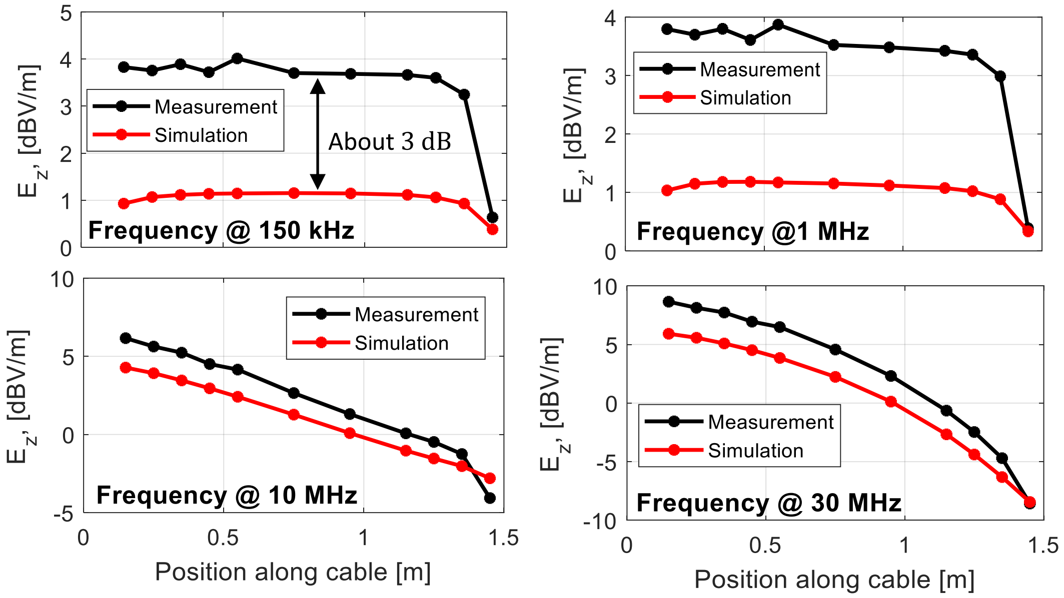

Figure 6.4: Comparison of the measured and simulated electric fields.

7 Validation and Discussion

It has been shown that the current measurement-based field prediction methods must fail at low frequencies due to unavoidable measurement errors. Now only the E-field measurement-based methods are considered as promising candidates for a practical application. This chapter shows the validation of the Huygens principle-based method and the static dipole-based method. It is discussed how accurate the antenna fields in a standard CISPR 25 setup can be predicted.

7.1 Validation of the Methods

7.1.1 Simple Cable Structure Configuration inside ALSE

7.1.1.1 Validation Setup

Before introducing the near-field measurements for a CISPR 25 measurement setup in a laboratory environment, a single-wire cable structure inside the chamber was involved in validating the proposed estimation methods (described in chapter 5, section 5.3 and 5.4). The structure was introduced, as shown in Figure 6.3 (b).

7.1.1.2 Near-Field Measurement Results

The near-field measurements were done, as described in chapter 6, and the measured near-field data (see Figure 6.4) were used for post-processing.

7.1.1.3 Comparison of Estimated Electric Fields

Totally eleven points were measured to prove the accuracy of the near-field measurements, and these near fields are used for estimating the electric fields at a field observation point. Here, the field observation point is set facing the cable center at 1 m distance and 10 cm above the ground.

Figure 7.1 shows the predicted results. MoM solution (CONCEPT-II) serves as a reference. The black curve gives the ALSE rod antenna measurement result, which was obtained by adding the captured antenna voltage with the antenna factor. As it has already described in chapter 1, the calculated antenna field is an approximated value. Here, a deviation of about 5 dB can be observed between the black curve and the MoM result, excepting the resonance at around 18 MHz. The resonance is known, as it described in 4 section 4.5.2.

The magenta curve shows estimated fields from the Huygens principle-based method, which is about 4 dB smaller than the result from MoM. The deviation is reasonable because it is a result of using only the E_z distribution for creating the Huygens' equivalent current sources. The reason is that from the theoretical analysis it is known that the calculated electric fields should be about 5 dB smaller than MoM results, when only E_z distributions are utilized (as demonstrated in Figure 5.22) (see chapter 5, section 5.4.2). Therefore, a deviation of about 4 dB is acceptable. If applying PEC to the closed Huygens' surface and supposing that the plane surface is closed in infinite, the $\vec{M}_S$ should be doubled. As a result, the calculated value should be additional added with 6 dB. With the additional 6 dB, the Huygens principle-based method will give a deviation of about 2 dB to the MoM result. The deviation comes mainly due to the inaccuracy from the near-field measurements.

The blue curve shows the result of the static dipole-based method. This method placed uniform charges along each subdivided segment of the cable (see Figure 5.16). By inserting the measured electric fields into (5.4), the charge densities were resolved. The data indicates that the estimated field is about 3 dB bigger than the result of MoM. The deviation is caused by errors in the conversion of the measured probe voltage to electric fields (the measured fields are about 3 dB stronger than the simulated values as given in Figure 6.4).

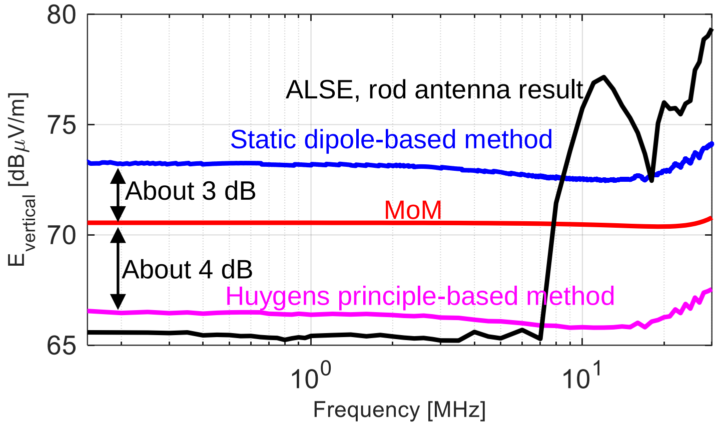

Figure 7.1: Estimated fields based on near-field measurements.

Figure 7.1 illustrates the results only for the case of having a 50 Ω termination; Figure 7.2 shows the results for some other load impedances conditions. The results are represented as the deviation in dB between the estimated electric fields and the MoM results. The cross markers illustrate the load impedances used for this investigation. The figure shows results at 1 MHz since at low frequencies and for most load impedances, the electric field maintains a constant value, which is a consequence of having a nearly constant voltage on the cable. The data shows that the static dipole-based method caused a deviation within 3 dB compared with the MoM results. In contrast, the Huygens principle-based method gives a deviation of about 5 dB, due to that the magnetic field distribution over the Huygens' surface is not involved. Here, it should be mentioned again, if PEC is applied, the Huygens principle-based method provided result should be added with 6 dB, which gives a result of around 1-2 dB deviation.

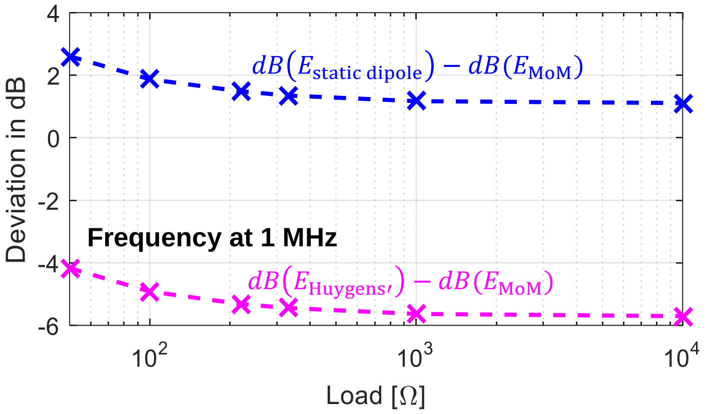

Figure 7.2: Deviation of estimated E_{vertical} for different resistive loads at 1 MHz.

7.1.2 Validation of Methods in a Laboratory Environment

7.1.2.1 **Validation Setup**

To validate the proposed methods for electric field estimation, a more complex CISPR 25 measurement setup was used, as shown in Figure 7.3. A simple floating PCB represents the EUT, and a 1.5 m long **t**wisted **w**ire **p**air (TWP) cable connects two ANs in one enclosure, according to CISPR 25.

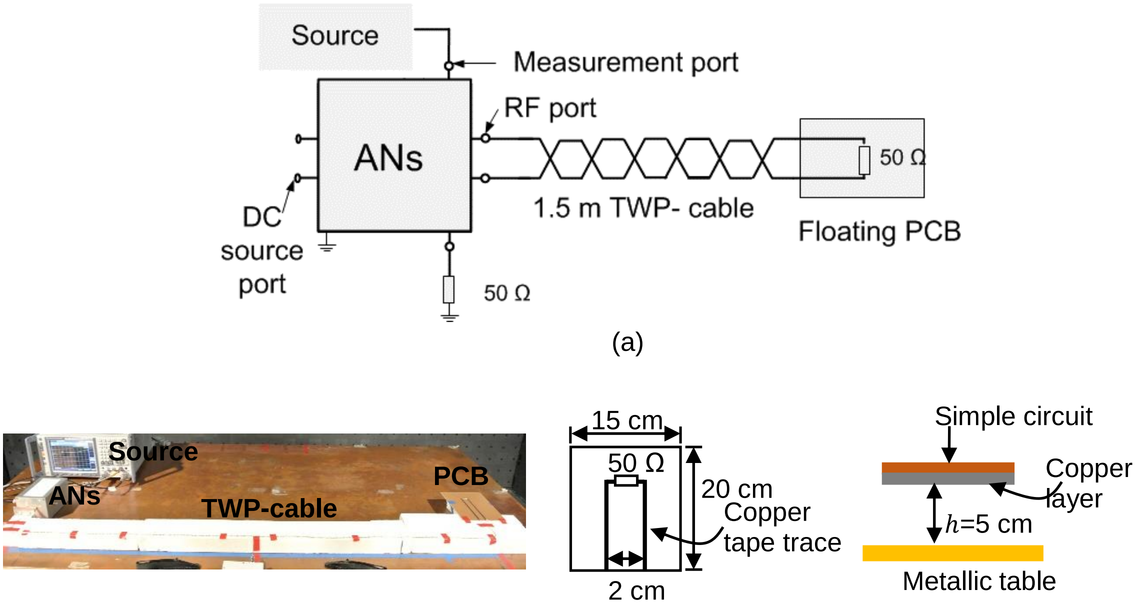

(a)

(b) (c) (d)

Figure 7.3: Measurement setup, (a) schematic of the setup, (b) photo of the setup inside the shielded chamber, (c) drawing of PCB, top view, (d) drawing of PCB, side view.

Figure 7.3 (a) shows the schematic of the setup, and (b) shows a photo of the measurement setup. Figure 7.3 (c) shows the dimensions of the PCB. On the top 15 cm, copper traces are placed at a distance of 2 cm and are terminated with 50 Ω. The bottom layer is a solid copper plane. The PCB is placed on a styrofoam block 5 cm above the metallic table. A side view is shown in Figure 7.3 (d). The setup was fed by the measurement port of the ANs using the tracking generator of the measurement receiver. This setup was used to analyze the different methods.

7.1.2.2 Near-Field Measurement Results

The measured electric fields along the cable of the setup in Figure 7.3 are shown for different frequencies in Figure 7.4.

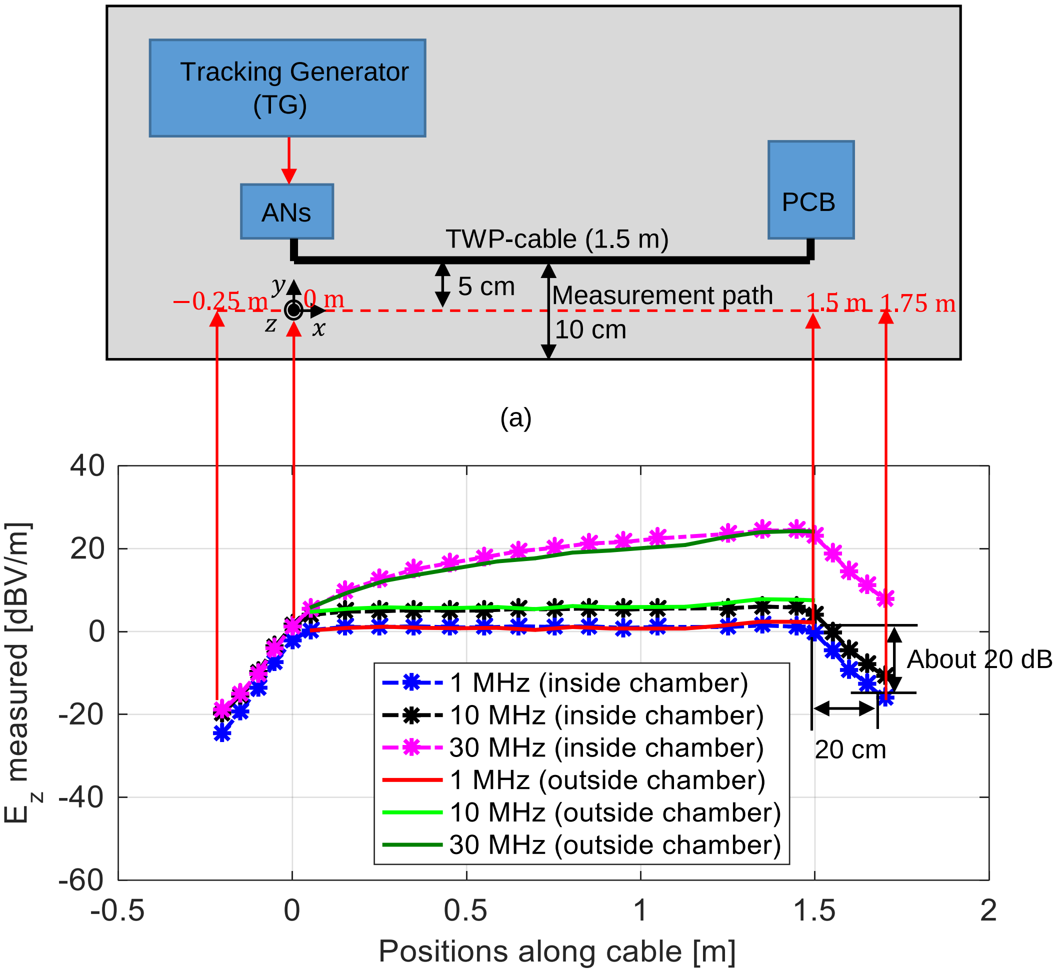

(a)

(b)

Figure 7.4: Near-field measurement results inside and outside a chamber.

The measurements were done inside and outside of a semi-anechoic chamber. Figure 7.4 (a) gives the measurement path. The cable starts at 0 m (AN-side) and ends at 1.5 m (PCB-side). An EMI measurement receiver [100] with an output power of 0 dBm was used as the source for exciting the measurement setup. The electric field probe, described in Figure 6.2, was placed at a distance of 5 cm in front of the cable. Figure 7.4 (b) shows the measured electric fields at 150 kHz, 1 MHz, 10 MHz, and 30 MHz. The star markers show the positions where fields were measured. The fields measured inside and outside of the chamber are nearly the same, which means there is no need to use the chamber. Only in a very noisy environment which may disturb the measurement, a small chamber might be needed. In this configuration, the dominating field contribution comes from the TWP-cable. The field intensity declines quickly when the probe moves far away from the cable. Only 20 cm distance causes a 20 dB decrease.

7.1.2.3 **Comparison of Estimated Electric Fields**

Figure 7.5 shows the estimated electric fields from different estimation methods. The red curve represents the standard field measurement result from a CISPR 25 rod antenna. The measurement was performed inside the ALSE. The antenna factor provided by the manufacturer was applied to calculate the electric field from the measured antenna voltage. At 150 kHz, a significant deviation can be seen, which is caused by the used test receiver that is specified only for frequencies above 300 kHz. It does not mean that measurements are impossible below 300 kHz, but sensitivity can be low.

The black curve shows the Huygens principle-based field prediction result. The measured near-field data shown in Figure 7.4 was used to calculate the equivalent current sources on the Huygens' surface. The Huygens' surface has a length of 1.5 m and a height of 1 m and is perpendicular to the metallic table and located in the front of the TWP-cable, 5 cm away from the metallic table's edge. The length of the Huygens' surface (from x = 0 cm to x = 1.5 m) is the same as the path where the near-field measurements were performed. This length is equal to the length of the TWP-cable, which produces fields. Based on the measured near-field points at x = 0.25 m, 0.75 m, and 1.25 m, the field data at other locations of the Huygens' surface could be found by field interpolation and approximation. The method was explained in section 5.4.3.

The cyan curve shows the predicted result using the static dipole-based method, where three segments were applied to create the static model. The measured near fields at x = 0.25 m, 0.75 m, and 1.25 m were used to calculate the charge density distribution over the TWP-cable.

Figure 7.5 shows that both the Huygens principle-based method and the static dipole-based method match well with the referenced standard field measurement result. The deviations between the field prediction methods and the standard field measurement result are within 3 dB.

Theoretically, a deviation of up to 5 dB can be expected when only E_Z distribution is used (the case used in the curve, no PEC is applied to the principle). The reason is that the rod antenna gives an antenna voltage, and the electric field is obtained by multiplication of the voltage with the antenna factor. It is known that the antenna voltage is the result of the integrated field along the rod antenna. Nevertheless, the Huygens principle-based method gives a field in only one field point. As it was shown before (chapter

4, section 4.3), the field at rod antenna location varies by 5 dB. Therefore, such a deviation should be expected. Another reason can be the electric field measurements with short probes (see Figure 6.4). A deviation of up to 3 dB could be found.

The static dipole-based method gives a result of about 3-5 dB more than the standard field, which is due to that each segment is assumed to have a uniform charge distribution and an infinite length to obtain the charge density from the measured electric field. Another source of errors is introduced by the measured field, which cannot be measured with very high accuracy.

Anyway, both proposed methods show a good match to the CISPR 25 standard measurement result and can be very helpful for pre-compliance analysis.

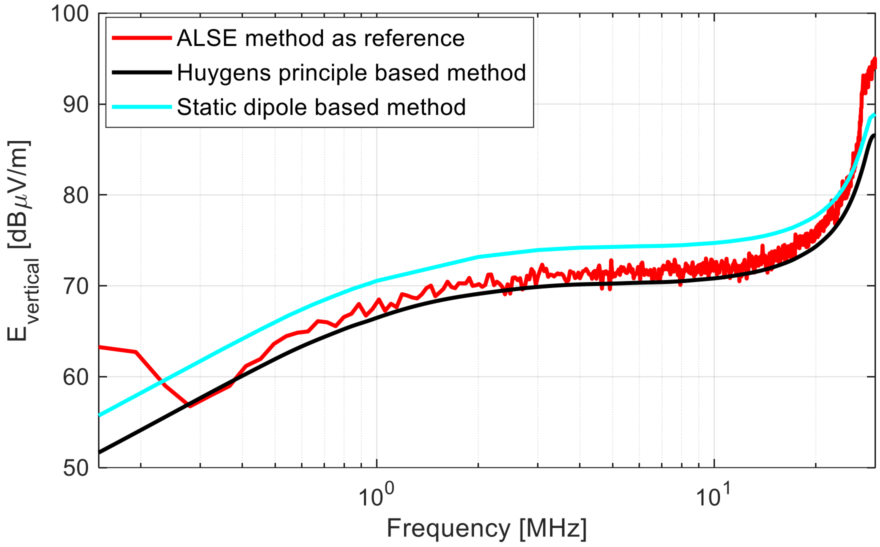

Figure 7.5: Estimated electric fields.

7.2 Discussion of the Presented Methods

The methods mentioned above are now shortly summarized and discussed:

1. MDM Method

This method has been proved to work well at higher frequencies. But at low frequencies it fails. The reasons for low frequency problems are summarized now and are described more in detail in chapter 5 section 5.1:

- From a theoretical point of view, the MDM method can be considered as a numerical summation of a set of piecewise constant current basis functions. Compared with triangular basis functions, which provide a continuous current distribution at cable connection especially for cables have a perpendicular connection (related to horizontal and vertical currents in this work), the piecewise constant current distribution limits the accuracy since the piecewise constant basis function shows a bad convergence. The work could show that the usage of a large number of segments at the vertical cable parts can reach a better field calculation result. However, the improvement only relates to very accurate current data from the simulation.

- The current measurement accuracy is limited. Furthermore, it is very difficult to obtain the vertical currents. The measurement of a high-resolution current distribution is impossible. Especially at lower frequencies, the measurement will not be able to resolve small phase changes along a cable. Data will be noisy. At low frequencies, this noise will be strongly amplified by the MDM data processing, as shown in chapter 5, section 5.1. Further deviations may be introduced by the insertion impedance of the current probe and position errors.

2. Huygens Principle-Based Method

The method described here uses a highly simplified application of the Huygens principle. Instead of capturing all four tangential field components with phase and magnitude on a surface that separates the measurement setup and the field location of interest, only the magnitude of the E_z-field is captured at a few locations along the harness. A good agreement to standard field measurements for the low frequency range can be seen. The reason for small deviations is that only the E_z field distribution from some measurement points is used, and the field extrapolation process is based on some assumptions not given fully. Furthermore, the E-field data can be inaccurate.

One can introduce, for example, an infinite large planar Huygens' surface filled with PEC, as shown in Figure 3.4. Under this condition, only the electric field distribution over the defined Huygens' surface is required. The equivalent magnetic current sources (calculated with electric field distribution over the surface) should be doubled, which results in the calculated final electric field must be added with 6 dB mathematically. As in this work, a truncated Huygens' surface is used, which produces theoretically 5 dB difference of field to the reference value (using only E_z, since contribution from E_x is negligible, see Figure 5.22). 1 dB deviation introduced by the truncated surface (by assuming the field distribution in the area outside of the truncated range is zero) must be considered. To observe the contribution from H-field distribution, this work also tried to add magnetic field measurement to compensate contribution from magnetic field distribution. Figure 7.6 shows the magnetic probe output power in dBm for the measurement setup in Figure 7.3. It can be seen that for this configuration at low frequencies, the magnetic field signal is very weak. Another reason would be the chosen magnetic field probe doesn't have enough sensitivity at low frequencies.

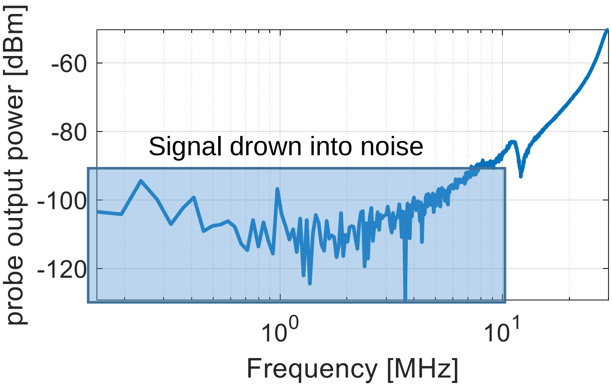

Figure 7.6: The influence of magnetic field distribution.

3. Static Dipole-Based Method

The basic idea of the method is that the charge on the cable with its image forms a set of static dipoles. The cable can be subdivided into segments, and the number of segments can equal the number of static dipoles. To obtain the charge over each segment, measured E-field data can be used. The measured data can be used to estimate the charges on the cable, and then, using electrostatic methods, the field at the point of interest can be calculated.

The results show a deviation in the range of 3 dB compared with the CISPR 25 standard field measurements. However, the accuracy highly depends on the charge estimation. The accuracy of the field probe is a limiting factor. Furthermore, as the method is only based on a static field approximation, it fails at higher frequencies.

8 Conclusion and Outlook

In automotive component emissions measurements, the ALSE method, as specified in CISPR 25 shows the best correlation to the emission behaviors of in-vehicle automotive components and is therefore commonly used. However, this measurement method requires a large and expensive chamber. Alternative methods were proposed from several scientific groups to avoid the need for a large chamber. These methods should predict the fields of a chamber measurement and can be used at least for pre-compliance measurements. Several approaches were developed in the past. The most promising ones are based on common-mode current measurements for emission source characterization. The underlying assumption is that the common-mode currents along the cable bundle of equipment under test dominate the emission. This method uses a multi-dipole model (also called MDM in this dissertation) to estimate the electric fields at the rod antenna location. While the common-mode current based methods work well for high frequencies, they fail for frequencies below 30 MHz. This thesis focuses on the analysis of the root cause for the failures at low frequencies and on finding a better alternative method to predict the CISPR 25 ALSE method results for the low frequency range. The main contributions can be subdivided into three parts.

First, the standard CISPR 25 measurement setups were analyzed. It is discussed that at lower frequencies, the capacitive coupling is the dominant coupling mechanism in comparison to the magnetic coupling. Feedback effects of the rod antenna can be neglected. Threshold values in the CISPR 25 standard are given as electric field strength values. As the rod antenna is in the near-field region, where the electric field is inhomogeneous, the single field value assumption for the rod antenna is incorrect. However, in practical engineering work, a simple measurement specification, which is in line with other specifications, can be more useful than an exact but difficult to handle method. Thus, the reduced accuracy is accepted. It is assumed that the antenna field can be found by multiplying the antenna voltage with an antenna factor, retrieved in a calibration procedure. The accuracy of this assumption is discussed. It could be found that the electric field varies at the rod antenna location up to 5 dB. Due to this reason, it is difficult to define a dedicated point at the rod antenna location where the electric field should be predicted.

Second, the limitations of the MDM at low frequencies were studied using theoretical analysis and measurements. An MDM configuration was investigated. The MDM requires current measurements as input data. It could be shown that accurate phase information is essential for a current based field prediction at low frequencies. Some parts of a current carrying structure have to be subdivided into a large number of dipoles to obtain acceptable results parameterized with highly accurate currents. As the phase measurements cannot provide the required accuracy, the MDM must fail at low frequencies.

Third, two new prediction methods were introduced, analyzed, and validated. The first approach uses measured electric fields along the cable bundle combined with the Huygens principle for antenna field prediction. This method is well known from high frequency applications, but is not limited to low frequencies and can be attractive to cover a wide frequency range with a single alternative method. In this method, in a first step, the vertical electric field is measured at a small number of locations close to the cable bundle on the ground plane. Next, additional data points are created using interpolation. In the next step, an analytical solution of the fields close to a charged line is used to obtain the field distribution by extrapolation above the ground plane. This way, the Huygens' surface adjacent to the emitting structure can be parameterized. It could be found that a closed Huygens box is not required. Finally, the Huygens principle is applied to obtain the field at the antenna location based on the field points on the Huygens' surface. The second approach uses the measured near-field data to create a set of static dipoles. The summation of the contribution of each dipole can also be used to predict the field at the antenna location.

There are three major scientific findings in this work. First, this dissertation analyzes the standard CISPR 25 setups in detail. For example, the work analyzes and discusses the coupling mechanisms and the feedback effects in the measurement setups. This has not been done in detail before. The antenna factor, which is typically used for the calculation of a field from an antenna voltage, is analyzed. Secondly, the limitations of the MDM model are analyzed in detail. It could be shown that a very fine discretization of a radiating structure can be necessary, and the current measurements have to be extremely accurate. The needed accuracy cannot be achieved with typical equipment today. Thirdly, the applicability of the Huygens principle to low frequency field estimations was investigated. It could be shown the first time that the Huygens principle cannot only be used at high frequencies for CISPR 25 pre-compliance analysis but also for low frequencies. A single method could cover the whole frequency range of CISPR 25 field measurements. A further alternative method, but accurate only at very low frequencies, could be found by using static dipoles. All findings are supported by simulation and measurement results.

An outlook of the work is to extend the founded method to higher frequencies using automation and data fusion. For automatization purposes, a measurement setup table could include a scanner that moves an electric field probe along the cable harness to capture the electric field. Particularly at the termination devices where the field is inhomogeneous or at high frequencies, automated capturing of many points can be advantageous. Data fusion can be applied if multiple sensors capture partially redundant data with the known weaknesses of each sensor path. In the data fusion process, the advantages of each sensor data could be used to create a weighted average over all sensor information. An example of such an approach may be the combination of an electric field sensor and a magnetic field sensor. Data fusion could reduce uncertainty and can be used to check plausibility mutually. For example, this could detect damage in one of the sensor paths.

Taking the idea of data fusion one step further, one may consider cancellation of ambient signals as part of the data fusion. Here, methods such as a direct cancellation from a reference antenna may be considered in case of a highly noisy unshielded laboratory environment.

9 Appendix

A. Derivation of the Vector Potentials $\vec{\mathrm{A}}$ and $\vec{\mathrm{F}}$ and the Field Equations

The following derivation is taken from [13].

Vector Potential $\vec{\mathrm{A}}$

In a source-free region, the magnetic flux density $\vec{B}$ is always solenoidal, that is, $\nabla\vec{B} = 0$. Therefore, it can be represented as the curl of another vector because it obeys the vector identity

$$\nabla \cdot (\nabla \times \vec{\mathrm{A}}) = 0. \tag{9.1}$$

where $\vec{\mathrm{A}}$ is an arbitrary vector. Thus, we define

$$\vec{B}_{\mathrm{A}} = \mu\vec{H}_A = \nabla \times \vec{\mathrm{A}}, \tag{9.2}$$

or

$$\vec{H}_{\mathrm{A}} = \frac{1}{\mu}\nabla \times \vec{\mathrm{A}}, \tag{9.3}$$

where subscript A indicates the fields due to the $\vec{\mathrm{A}}$ potential. Substituting (9.3) into Maxwell's curl equation

$$\nabla \times \vec{E}_{\mathrm{A}} = -j\omega\mu\vec{H}_{\mathrm{A}} \tag{9.4}$$

reduces it to

$$\nabla \times \vec{E}_{\mathrm{A}} = -j\omega\mu\vec{H}_{\mathrm{A}} = -j\omega\nabla \times \vec{\mathrm{A}}, \tag{9.5}$$

which can also be written as

$$\nabla \times \left[\vec{E}_{\mathrm{A}} + j\omega\vec{\mathrm{A}}\right] = 0. \tag{9.6}$$

From the vector identity

$$\nabla \times (-\nabla\phi_{\mathrm{e}}) = 0, \tag{9.7}$$

and (9.6), it follows that

$$\vec{E}_{\mathrm{A}} + j\omega\vec{\mathrm{A}} = -\nabla\phi_{\mathrm{e}}, \tag{9.8}$$

or

$$\vec{E}_{\mathrm{A}} = -\nabla\phi_{\mathrm{e}} - j\omega\vec{\mathrm{A}}. \tag{9.9}$$

ϕ_e represents an arbitrary electric scalar potential that is a function of position.

Taking the curl of both sides of (9.2) and using the vector identity

$$\nabla \times \nabla \times \vec{A} = \nabla\left(\nabla \cdot \vec{A}\right) - \nabla^2 \vec{A} \tag{9.10}$$

leads to

$$\nabla \times \left(\mu \vec{H}_{\mathrm{A}}\right) = \nabla\left(\nabla \cdot \vec{\mathrm{A}}\right) - \nabla^2 \vec{\mathrm{A}}. \tag{9.11}$$

For a homogeneous medium, (9.11) reduces to

$$\mu \nabla \times \vec{H}_{\mathrm{A}} = \nabla\left(\nabla \cdot \vec{\mathrm{A}}\right) - \nabla^2 \vec{\mathrm{A}}. \tag{9.12}$$

Equating Maxwell's equation

$$\nabla \times \vec{H}_{\mathrm{A}} = \vec{J} + j\omega\varepsilon \vec{E}_{\mathrm{A}} \tag{9.13}$$

to (9.12) leads to

$$\mu \vec{J} + j\omega\mu\varepsilon \vec{E}_{\mathrm{A}} = \nabla\left(\nabla \cdot \vec{\mathrm{A}}\right) - \nabla^2 \vec{\mathrm{A}}. \tag{9.14}$$

Substituting (9.9) into (9.14) reduces it to

$$\nabla^2 \vec{\mathrm{A}} + \beta \vec{\mathrm{A}} = \mu \vec{J} + \nabla\left(\nabla \cdot \vec{\mathrm{A}}\right) + \nabla(j\omega\mu\varepsilon\phi_{\mathrm{e}}) = -\mu \vec{J} + \nabla\left(\nabla \cdot \vec{\mathrm{A}} + \omega\mu\varepsilon\phi_{\mathrm{e}}\right), \tag{9.15}$$

where $\beta^2 = \omega^2 \mu\varepsilon$.

In (9.2) the curl of $\vec{\mathrm{A}}$ was defined. Now we are free to define the divergence of $\vec{\mathrm{A}}$, which is independent of its curl. Both are required to uniquely define $\vec{\mathrm{A}}$. In order to simplify (9.15), let

$$\nabla \cdot \vec{\mathrm{A}} = -j\omega\mu\varepsilon\phi_{\mathrm{e}} \Rightarrow \phi_{\mathrm{e}} = -\frac{1}{j\omega\mu\varepsilon} \nabla \cdot \vec{\mathrm{A}}, \tag{9.16}$$

which is known as the Lorenz condition (or gauge). Other gauges may be defined. Substituting (9.16) into (9.15) leads to

$$\nabla^2 \vec{\mathrm{A}} + \beta^2 \vec{\mathrm{A}} = -\mu \vec{J}. \tag{9.17}$$

In addition, (9.9) reduces to

$$\vec{E}_{\mathrm{A}} = -\nabla\phi_{\mathrm{e}} - j\omega\vec{\mathrm{A}} = -j\omega\vec{\mathrm{A}} - j\frac{1}{\omega\mu\varepsilon}\nabla\left(\nabla \cdot \vec{\mathrm{A}}\right). \tag{9.18}$$

Once $\vec{\mathrm{A}}$ is known, $\vec{H}_{\mathrm{A}}$ can be found from (9.3) and $\vec{E}_{\mathrm{A}}$ from (9.18). $\vec{E}_{\mathrm{A}}$ can just as easily be found from Maxwell's equation (9.13) by setting $\vec{J} = 0$.

Vector Potential $\vec{\mathrm{F}}$

In a source-free region, the electric flux density $\vec{D}$ is always solenoidal, that is, $\nabla\vec{D} = 0$. Therefore, it can be represented as the curl of another vector because it obeys the vector identity

$$\nabla \cdot \left(-\nabla \times \vec{\mathrm{F}}\right) = 0, \tag{9.19}$$

where $\vec{\mathrm{F}}$ is an arbitrary vector. Thus we can define $\vec{D}_{\mathrm{F}}$ by

$$\vec{D}_{\mathrm{F}} = -\nabla \times \vec{\mathrm{F}}, \tag{9.20}$$

or

$$\vec{E}_{\mathrm{F}} = -\frac{1}{\varepsilon}\nabla \times \vec{\mathrm{F}}, \tag{9.21}$$

where the subscript F indicates the fields due to the $\vec{\mathrm{F}}$ potential. Substituting (9.21) into Maxwell's curl equation

$$\nabla \times \vec{H}_{\mathrm{F}} = j\omega\varepsilon\vec{E}_{\mathrm{F}} \tag{9.22}$$

reduces it to

$$\nabla \times \left(\vec{H}_{\mathrm{F}} + j\omega\vec{\mathrm{F}}\right) = 0. \tag{9.23}$$

From the vector identity (9.7), it follows that

$$\vec{H}_{\mathrm{F}} = -\nabla\phi_{\mathrm{m}} - j\omega\vec{\mathrm{F}}, \tag{9.24}$$

where ϕ_{m} represents an arbitraty magnetic scalar potential that is a function of position. Taking the curl of (9.21)

$$\nabla \times \vec{E}_{\mathrm{F}} = -\frac{1}{\varepsilon}\nabla \times \nabla \times \vec{\mathrm{F}} = -\frac{1}{\varepsilon}\left[\nabla\left(\nabla \cdot \vec{\mathrm{F}}\right) - \nabla^2\vec{\mathrm{F}}\right] \tag{9.25}$$

and equating it to Maxwell's equation

$$\nabla \times \vec{E}_{\mathrm{F}} = -\vec{M} - j\omega\mu\vec{H}_{\mathrm{F}} \tag{9.26}$$

lead to

$$\nabla^2\vec{\mathrm{F}} + j\omega\mu\varepsilon\vec{H}_{\mathrm{F}} = \nabla\left(\nabla\vec{\mathrm{F}}\right) - \varepsilon\vec{M}. \tag{9.27}$$

Substituting (9.24) into (9.27) reduces it to

$$\nabla^2\vec{\mathrm{F}} + \beta^2\vec{\mathrm{F}} = -\varepsilon\vec{M} + \nabla\left(\nabla \cdot \vec{\mathrm{F}} + j\omega\mu\varepsilon\phi_{\mathrm{m}}\right). \tag{9.28}$$

Letting

$$\nabla \cdot \vec{\mathrm{F}} = -j\omega\mu\varepsilon\phi_{\mathrm{m}} \Rightarrow \phi_{\mathrm{m}} = -\frac{1}{j\omega\mu\varepsilon}\nabla \cdot \vec{\mathrm{F}} \tag{9.29}$$

reduces (9.28) to

$$\nabla^2\vec{\mathrm{F}} + \beta^2\vec{\mathrm{F}} = -\varepsilon\vec{M} \tag{9.30}$$

and (9.24) to

$$\vec{H}_{\mathrm{F}} = -j\omega\vec{\mathrm{F}} - \frac{j}{\omega\mu\varepsilon}\nabla\left(\nabla\cdot\vec{\mathrm{F}}\right). \tag{9.31}$$

Once $\vec{\mathrm{F}}$ is known, $\vec{E}_{\mathrm{F}}$ can be found from (9.21) and $\vec{H}_{\mathrm{F}}$ from (9.31) or (9.26) by setting $\vec{M} = 0$.

Field equations in terms of $\vec{\mathrm{A}}$ and $\vec{\mathrm{F}}$

The total $\vec{E}$ and $\vec{H}$ fields are obtained by the superposition of the individual fields due to $\vec{\mathrm{A}}$ and $\vec{\mathrm{F}}$. Superposition of (9.18) and (9.21) leads to the total electric field

$$\vec{E} = \vec{E}_{\mathrm{A}} + \vec{E}_{\mathrm{F}} = -j\omega\vec{\mathrm{A}} - j\frac{1}{\omega\mu\varepsilon}\nabla\left(\nabla\cdot\vec{\mathrm{A}}\right) - \frac{1}{\varepsilon}\nabla\times\vec{\mathrm{F}}, \tag{9.32}$$

and superposition of (9.3) and (9.31) leads to the total magnetic field

$$\vec{H} = \vec{H}_{\mathrm{A}} + \vec{H}_{\mathrm{F}} = \frac{1}{\mu}\nabla\times\vec{\mathrm{A}} - j\omega\vec{\mathrm{F}} - \frac{j}{\omega\mu\varepsilon}\nabla\left(\nabla\cdot\vec{\mathrm{F}}\right). \tag{9.33}$$

B. Determining the Current Direction over a Surface Patch

The rectangular patches used in the dissertation are the discrete patches over the Huygens' surface. Here, the direction the currents flow inside/outside of a patch is also determined with the help of the Huygens' surfaces. Following derivation is coming from [61].

Figure 3.7 is used for explanation. To determine the direction of the currents over the surface patch, several steps should be performed. The first step is to determine the vector $\vec{b}$. This vector gives the direction from the centroid $\vec{S}$ to the edge center (see sub-figure (a)). The second step is to determine the normal vector $\vec{n}$ of the patch using the vector $\vec{b}$ and the edge vector $\vec{v}$. It can be calculated by:

$$\vec{n} = \pm \frac{\vec{v} \times \vec{b}}{\left|\vec{v} \times \vec{b}\right|}. \tag{9.34}$$

The sign of $\vec{n}$ can be ascertained with the inner product of $\vec{n} \cdot (\vec{S} - \vec{A})$, where $\vec{S}$ is the aforementioned centroid of the patch. The point $\vec{Q}$ is any inner point inside the Huygens' box (see Figure 3.5). If the inner product satisfies:

$$\vec{n} \cdot (\vec{S} - \vec{Q}) > 0, \tag{9.35}$$

where the sign doesn't need to be changed. Otherwise, the $\vec{n}$ should be converted to $-\vec{n}$. Once the vector $\vec{n}$ is determined, the edge vector $\vec{v}$ can be obtained according to the right-hand rule. The third step is to determine a vector $\vec{c}$, which is given by:

$$\vec{c} = \pm \vec{v} \times \vec{n}. \tag{9.36}$$

The sign of $\vec{c}$ can be decided through the inner product of $\vec{c} \cdot \vec{b}$. If the inner product: $\vec{c} \cdot \vec{b} < 0$, $\vec{c}$ should have the opposite sign ($-\vec{c}$). Finally, using the determined vector $\vec{c}$, the direction of surface electric current I_J passing the edge of the patch, for example, can be acquired using:

$$\vec{c} \cdot (\vec{n} \times \vec{H}) > 0 \quad => \quad I_J = +\left|\vec{v} \cdot \vec{H}\right|, \tag{9.37}$$

$$\vec{c} \cdot (\vec{n} \times \vec{H}) < 0 \quad => \quad I_J = -\left|\vec{v} \cdot \vec{H}\right|, \tag{9.38}$$

$$\vec{c} \cdot (\vec{n} \times \vec{H}) = 0 \quad => \quad I_J = 0. \tag{9.39}$$

Similarly, the direction of magnetic current I_M can be also determined with $\vec{c} \cdot (\vec{E} \times \vec{n})$.

C. Gaussian Integration

Chapter 3, section 3.5.1 introduced how to calculate the surface electric current density $\vec{J}_{\mathrm{s_n}}(\vec{r}')$ and surface magnetic current density $\vec{M}_{\mathrm{s_n}}(\vec{r}')$ for n^{th} patch. When for all patches over the defined Huygens' surface, the surface electric and magnetic current densities are known, the electric fields can be calculated with equation (3.24). However, equation (3.24) contains a surface integral. To accomplish the integration, usually numerically approximate integrals, such as Newton-Cotes Quadrature formulas, Open Newton-Cotes, Composite Simpson's rule, Legendre-Gauss quadrature, etc. can be applied. In this work, Gaussian Quadrature integrals (which is described in detail in [101]) are applied.

The general 1D Gaussian quadrature formula (e.g., described in [57] (p. 259)) in one dimension is conventionally defined for the standard interval [-1, 1] as

$$\int_{-1}^{1} f(\xi)d\xi \approx \sum_{i=1}^{N} w_i f(\xi_i), \tag{9.40}$$

where ξ_i and w_i are Gaussian quadrature points and weights. Weights w_i and ξ_i are tabulated for some lower order (up to $N = 3$), as shown in the Table 2.

TABLE 2: WEIGHTS AND GAUSSIAN QUADRATURE POINTS FOR INTEGRATION

Number of points, N	w_i	ξ_i
1	2	0
2	1	$\pm\sqrt{1/3}$
3	$8/9$	0
	$5/9$	$\pm\sqrt{3/5}$

When the numerical calculation applied to quadrilateral elements for a 2D integration, the standard quadrilateral element is often used, as illustrated in Figure 9.1. The domain of integration is [-1, 1] for both direction ξ_1 and ξ_2, and the integral can be numerically calculated by

$$\int_{-1}^{1}\int_{-1}^{1} f(\xi_1, \xi_2)d\xi_1 d\xi_2 \approx \sum_{i=1}^{M}\sum_{j=1}^{N} w_i w_j f\big(\xi_{1i}, \xi_{2j}\big), \tag{9.41}$$

in which ξ_{1i} and w_i are Gaussian quadrature points and weights of order M in the ξ_1 direction; ξ_{2j} and w_j are Gaussian quadrature points of order N in the ξ_2 direction. When $M = N$, we call it as Gaussian quadrature of order N.

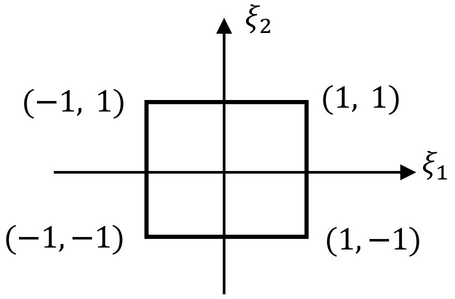

Figure 9.1: The standard quadrilateral element.

However, the integration of surface is usually in a global coordinate system. An example is given in Figure 9.2 (a), where the surface patch is in the interval $[x_1, x_2]$ and $[y_1, y_2]$. To solve the integration, a linear mapping is required to transform the patch from the global coordinate system to the local coordinate system. The local coordinate is illustrated in Figure 9.2 (b). Assuming the Gaussian quadrature is of order $N = 3$, Hence, there are nine total Gaussian points (black cross points) represented in the standard quadrilateral element. The mapping can be expressed by:

$$\int_{x_1}^{x_2}\int_{y_1}^{y_2} f(x,y)dxdy \approx \frac{x_2 - x_1}{2}\cdot\frac{y_2 - y_1}{2}\cdot\sum_{i=1}^{M}\sum_{j=1}^{N}\omega_i\omega_j f\left(u_i, v_j\right), \tag{9.42}$$

in which $u_i = \frac{x_2+x_1}{2} + \frac{x_2-x_1}{2}\xi_{1i}$; $v_j = \frac{y_2+y_1}{2} + \frac{y_2-y_1}{2}\xi_{2j}$.

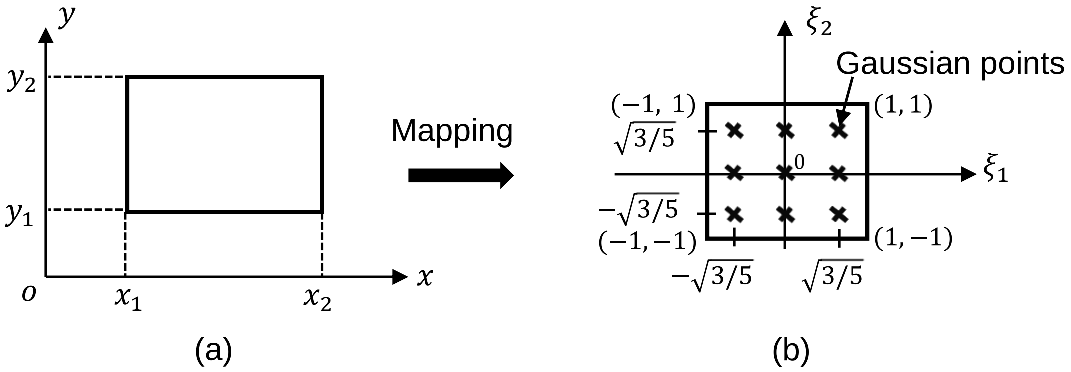

(a) (b)

Figure 9.2: Linear mapping. (a) a patch in the global coordinate system, (b) the local system, where the Gaussian quadrature points ($N = 3$) in the standard quadrilateral element.

D. Calculation of Mutual Inductance with FastHenry2

For the computation of the mutual inductance between the cable structure and the rod antenna the software FastHenry2 was applied. This software is capable to calculate the frequency-dependent self and mutual inductances of 3D conductive structures with a magnetoquasistatic approximation [68].

The setup in Figure 4.2 was applied. The 1.5 m cable is shorted to the ground plane at one end to form a loop. A 1 m rod is placed in 1 m distance to the loop. For detailed model information the FastHenry2 model code is shown below. As the antenna rod is perpendicular to the loop, it can be expected that the mutual inductance is zero, due to perfect symmetry in the simulation environment. To provide a more realistic setup a tilt angle of the antenna rod was introduced (rotation in parallel to xz-plane). The calculation was performed with a tilt angle between 0° and 10°, which seems to be a realistic range in a real setup.

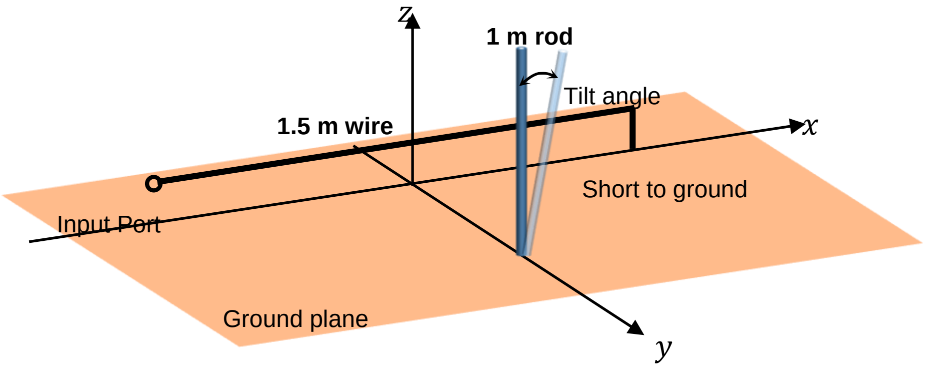

Figure 9.3: Setup for calculation of the mutual inductance.

To verify the simulation results, the loop inductance of the cable structure and the partial inductance of the rod can be compared first with analytical results. Table 3 shows the results. It is shown that the simulated results agree to some extent with the analytical results.

TABLE 3: COMPARISON OF LOOP INDUCTANCE AND ROD PARTIAL INDUCTANCE BASED ON FASTHENRY 2 AND ANALYTICAL CALCULATIONS

	Loop inductance	**Rod partial inductance**
FastHenry2	1.61 μH	1.01 μH
Analytical	1.59 μH (equation (4.2))	0.98 μH (equation (9.49))

The mutual inductance dependence of the tilt angle is shown in Figure 9.4. For the analysis of coupling mechanisms, the maximum mutual inductance of 0.3 nH at 10° tilt angle was used in the simple equivalent circuit model.

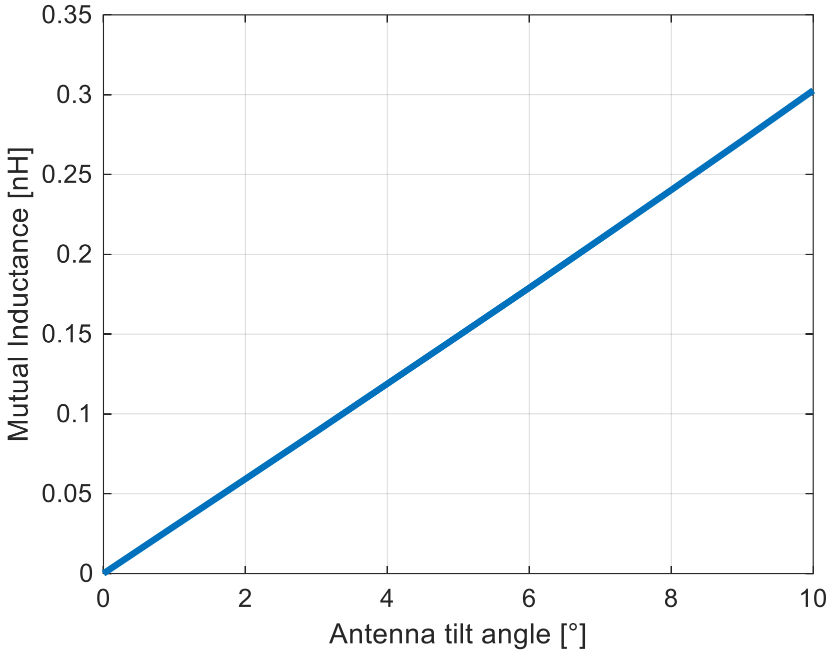

Figure 9.4: Mutual inductance depending on rod antenna tilt angle.

FastHenry2 model code

```
**** CISPR 25 mutual inductance between cable and rod antenna****

* All length in meter
.Units M

* Copper is default conductivity in 1/(m*Ohms)
.Default sigma=58.0e6

**** Ground plane ****
g1 x1 = -0.8 y1 = -0.25 z1 = 0
+ x2 = 0.8 y2 = -0.25 z2 = 0
+ x3 = 0.8 y3 = 1.25 z3 = 0
* thickness:
+ thick = 0.001
* discretization:
+ seg1 = 64 seg2 = 12
* define nodes for connecting cable to ground plane
+ nin (-0.75,0.0,0.0)
+ nout (0.75,0.0,0.0)

**** Single-wire cable over ground ****
N1 x=-0.75 y=0.0 z=0.05
N2 x=0.75 y=0.0 z=0.05
E1 N1 N2 w=0.001 h=0.001

* connect one end of cable to ground
.equiv N2 nout
```

```
* compute loop inductance of the cable over ground
.external nin N1

**** Rod antenna ****
N12 x=0.0 y=1.0 z=0.01
* here 10° tilt as example, see N22 coordinates
N22 x=0.1736 y=1.0 z=0.9848
E2 N12 N22 w=0.01 h=0.01

* compute partial inductance of rod antenna
.external N12 N22

* Compute impedance matrix at frequency
.freq fmin=9e3 fmax=9e3
.end
```

E. Equivalent Circuit Model-Based Analysis of Coupling Mechanisms and Feedback Effects of CISPR 25 Measurement Setups

How inductive and capacitive coupling are originated, can be initially explained for the CISPR 25 measurement setups as follows: supposing current on the cable structure creates a time-varying magnetic flux density, which passes through rod antenna. According to Faraday's law, a resulting voltage is induced in the antenna (by simplifying and imaging the antenna as a closed current loop, which is formed by the antenna self-capacitance and the antenna load). This mechanism is known as inductive coupling. At the same time, assuming that the voltage on the cable structure (from the charge distribution along the cable) generates a time-varying electric field. A portion of the field terminates on the charges which are induced in the antenna. The resulting time-varying charges create a current flow in the antenna. This mechanism is known as capacitive coupling.

Furthermore, since the electric and magnetic fields generated from cable structure induce current and voltage in the antenna, these induced sources on the other side create electric and magnetic fields, which may be coupled back to the cable structure. This "coupled back" influence is the influence from the antenna to the cable structure, which is referred to as feedback effect in the work. It will be analyzed if the feedback effect on the cable is significant. This is important because the field prediction methods applied in this work should predict the electric field at the antenna position without the antenna.

It is well known that in the near-field region the electric and magnetic fields can be regarded as independent. With this assumption, the inductive and capacitive coupling of adjacent structures can also be described independently.

E.1 Inductive Coupling and Related Feedback Effect

Both the cable structure and the antenna have self-inductance, respectively, as both can carry current. For the definition of the self-inductance of a current loop, a total magnetic flux ψ_1 though the loop surface S_1 is required and can be expressed as an integral of magnetic flux density $\vec{B}$ over S_1:

$$\psi_1 = \int_{S_1} \vec{B} d\vec{s}. \tag{9.43}$$

Then, the self-inductance can be defined as the ratio of the total magnetic flux ψ_1 and the current I_1 in the loop:

$$L = \frac{\psi_1}{I_1}. \tag{9.44}$$

The induced voltage V_1 across the self-inductance in case of harmonic magnetic flux density and current can be expressed by

$$V = j\omega\psi_1 = j\omega L I_1. \tag{9.45}$$

As the antenna and cable are adjacent, both are linked by mutual inductance. The mutual inductance between two loops, one of which carries a current I_1 is defined as

$$M_{12} = \frac{\psi_2}{I_1}, \tag{9.46}$$

where ψ_2 is the magnetic flux penetrating the surface of the second loop S_2 that is caused by the current I_1 of the first loop. ψ_2 can be written as

$$\psi_2 = \int\limits_{S_2} \vec{B}_{12} d\vec{s}. \tag{9.47}$$

Where $\vec{B}_{12}$ is the magnetic flux density caused by the first loop and penetrating the surface of the second loop. The induced voltage V_2 in the second loop is then:

$$V_2 = j\omega\psi_2 = j\omega M_{12} I_1. \tag{9.48}$$

The self- and mutual inductance depend on the geometry and surrounding material and can be found by measurements or computational models. In the case of simple geometries (e.g., two parallel circular loops), there are analytical solutions. The calculation of the per-unit self-inductance of a cable over the ground was already given in section 4.2.2 equation (4.2). Here the inductance L_A of the rod antenna can be estimated by the method of calculating the self-partial-inductance a wire, which is given in [69], as

$$L_A \cong 2 \cdot 10^{-7} h_A \left(\ln\left(\frac{2h_A}{r_A}\right) - 1\right) \quad r_A \ll h_A, \tag{9.49}$$

in which r_A is the rod antenna radius, and h_A is the antenna height. It is noted that the antenna is above ground, which means the height h_A should be doubled when using (9.49) (according to the image theory).

This work introduced the quasi-static numerical solver FastHenry2 [68] and obtained 0.3 nH for the present CISPR 25 geometry. The FastHenry2 solver program is described in Appendix D.

a) Equivalent Circuit Model for Inductive Coupling

Based on the simplified structure in Figure 4.2, the applied model for inductive coupling is shown in Figure 9.5. The cable equivalent circuit consists of a lumped self-inductance L_{TL} and capacitance C_{TL}, which can be calculated using transmission line theory described in section 4.2.2. A feeding voltage source V_S with a source impedance Z_S is attached on the left side and provides a current I_S. The circuit is terminated with a load impedance Z_L. The rod antenna equivalent circuit consists of the lumped self-capacitance C_A and self-inductance L_A. A load Z_M is attached. The inductive coupling between cable equivalent circuit and rod antenna equivalent circuit is illustrated by a mutual inductance M.

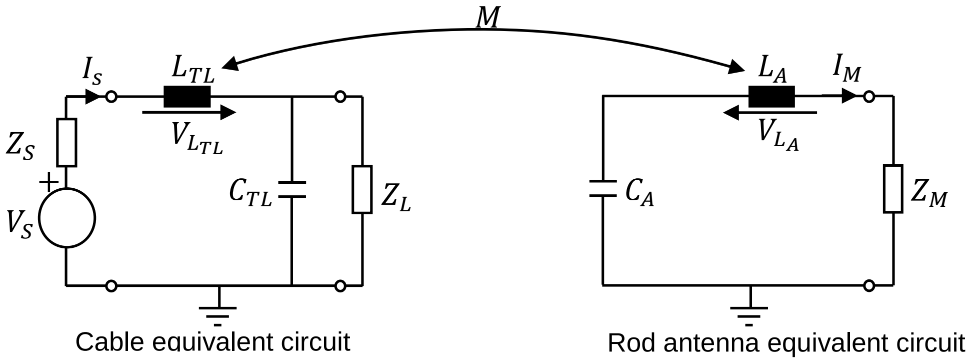

Figure 9.5: Equivalent circuit model for inductive coupling between cable structure and antenna.

Since there is no active source in the antenna circuit, the voltage V_{L_A} across the antenna self-inductance L_A is caused by the current in the cable circuit I_S and the mutual inductance M, which can be expressed as

$$V_{L_A} = -j\omega M I_S. \tag{9.50}$$

The voltage across the cable self-inductance is a contribution of the source current I_S through the self-inductance L_{TL} and the antenna current I_M coupled by the mutual inductance M, which can be expressed as

$$V_{L_{TL}} = j\omega L_{TL} I_S - j\omega M I_M. \tag{9.51}$$

The second term of (9.51) can be represented as an additional voltage source in the cable equivalent circuit due to the current in the antenna (feedback) and written as

$$V_{FB} = -j\omega M I_M. \tag{9.52}$$

This voltage V_{FB} is called here feedback voltage. Now the equivalent circuit model in Figure 9.5 can be remodeled with the help of the identified voltage sources in (9.50) and (9.52), as shown in Figure 9.6.

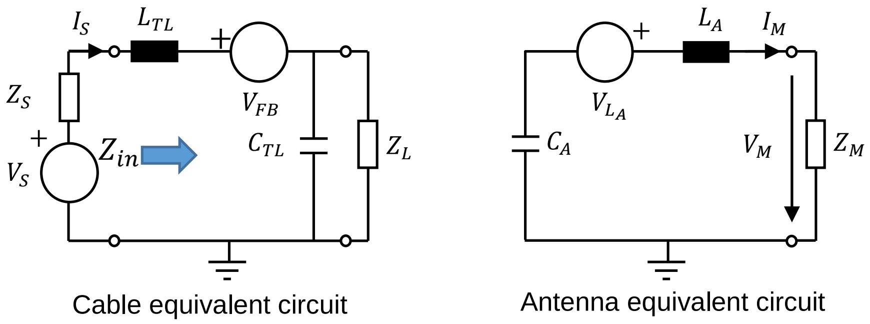

Figure 9.6: Representation of induced voltages due to inductive coupling.

b) Feedback Effect due to Inductive Coupling

Figure 9.6 is used to estimate the feedback effect of the rod antenna due to inductive coupling. The relation between the antenna current I_M and the induced voltage V_{L_A} can be written as:

$$V_{L_A} = \left(\frac{1}{j\omega C_A} + j\omega L_A + Z_M\right) I_M. \tag{9.53}$$

By replacing V_{L_A} using (9.50), (9.53) can be expressed as:

$$-j\omega M I_S = \left(\frac{1}{j\omega C_A} + j\omega L_A + Z_M\right) I_M. \tag{9.54}$$

By rearranging (9.54), I_M can be expressed as

$$I_M = \frac{-j\omega M I_S}{\frac{1}{j\omega C_A} + j\omega L_A + Z_M}. \tag{9.55}$$

Inserting (9.55) to (9.52), the feedback voltage V_{FB} can be expressed as:

$$V_{FB} = -\underbrace{\frac{\omega^2 M^2}{\left(\frac{1}{j\omega C_A} + j\omega L_A + Z_M\right)}}_{Z_{FB_M}} I_S. \tag{9.56}$$

Z_{FB_M} is defined as impedance between the feedback voltage V_{FB} and the current in the cable I_S. The input impedance of the cable at the source Z_{in} can be expressed as

$$Z_{in} = j\omega L_{TL} + Z_{FB_M} + \frac{Z_L \cdot \frac{1}{j\omega C_{TL}}}{Z_L + \frac{1}{j\omega C_{TL}}}. \tag{9.57}$$

When the load impedance satisfies $Z_L \ll \frac{1}{j\omega C_{TL}}$, the cable capacitance can be neglected, and (9.57) can be simplified as

$$Z_{in} = j\omega L_{TL} + Z_{FB_M} + Z_L. \tag{9.58}$$

Typical rod antenna parameters $C_A = 10\,\mathrm{pF}, L_A = 1\,\mu\mathrm{H}, Z_M \geq 100\,\mathrm{k\Omega}$ are used, which are introduced in chapter 4, section 4.4.1. Here, $Z_M = 1\,\mathrm{M\Omega}$ is used as an example. and mutual inductance of $M = 1\,\mathrm{nH}$ / $M = 0.1\,\mathrm{nH}$ (typically in vehicle [15]) and $0.3\,\mathrm{nH}$ (numerically determined from FastHenry2) are applied here to evaluate Z_{FB_M}. The results are shown in Figure 9.7, which points out that the feedback effect from the antenna can be neglected, as $Z_{FB_M} \ll j\omega L_{TL} + Z_L$ (see (9.58)) even for low Z_L(e.g. 1 Ω).

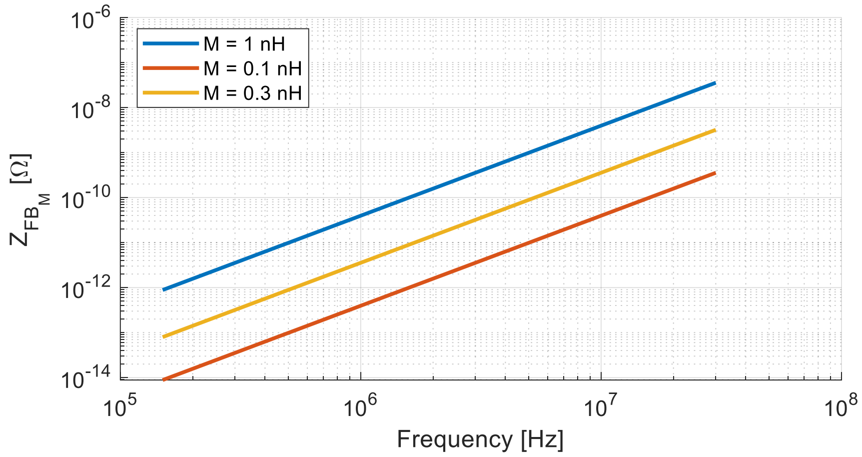

Figure 9.7: Additional impedance in the cable circuit due to the feedback effect of inductive coupling.

c) Induced Voltage at the Antenna due to Inductive Coupling

By neglecting the feedback effect caused by inductive coupling, the model in Figure 9.6 can be simplified to the model in Figure 9.8. This model (see Figure 9.8) can be used to derive induced antenna voltage caused by inductive coupling. Based on the rod antenna equivalent circuit in the model, the voltage V_M over load Z_M can be expressed as

$$V_M = \frac{Z_M}{\frac{1}{j\omega C_A} + j\omega L_A + Z_M} V_{L_A}. \tag{9.59}$$

where V_{L_A} is the voltage induced by the inductive coupling (see (9.50)). Replacing V_{L_A} by (9.50) to (9.59), V_M can be written as

$$V_M = -j\omega M \frac{Z_M}{\frac{1}{j\omega C_A} + j\omega L_A + Z_M} I_S. \tag{9.60}$$

where I_S is the current in the cable, which can be obtained by

$$I_S = \frac{1}{Z_S + j\omega L_{TL} + Z_L} V_S. \tag{9.61}$$

Combining (9.60) and (9.61), V_M can be written as

$$V_M = \underbrace{-j\omega M \frac{Z_M}{\frac{1}{j\omega C_A} + j\omega L_A + Z_M} \frac{1}{Z_S + j\omega L_{TL} + Z_L}}_{T_M} V_S. \tag{9.62}$$

T_M in (9.62) is defined as the transfer function between the antenna voltage V_M and the source voltage V_S.

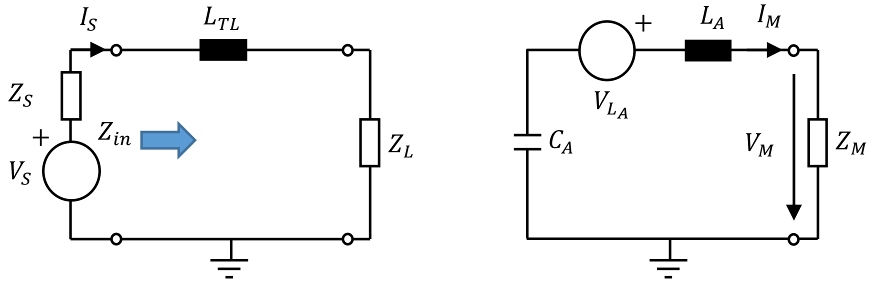

Cable equivalent circuit

Rod antenna equivalent circuit

Figure 9.8: Equivalent circuit model representing inductive coupling between cable and antenna by neglecting feedback effect and cable self-capacitance C_{TL}.

Using typical antenna parameters described above and typical cable inductivity ($L_{TL} = 1.5\ \mu\mathrm{H}$) and mutual inductance of $M = 0.3\ \mathrm{nH}$ for different loads Z_L (source impedance $Z_S = 0\ \Omega$), T_M can be represented in Figure 9.9.

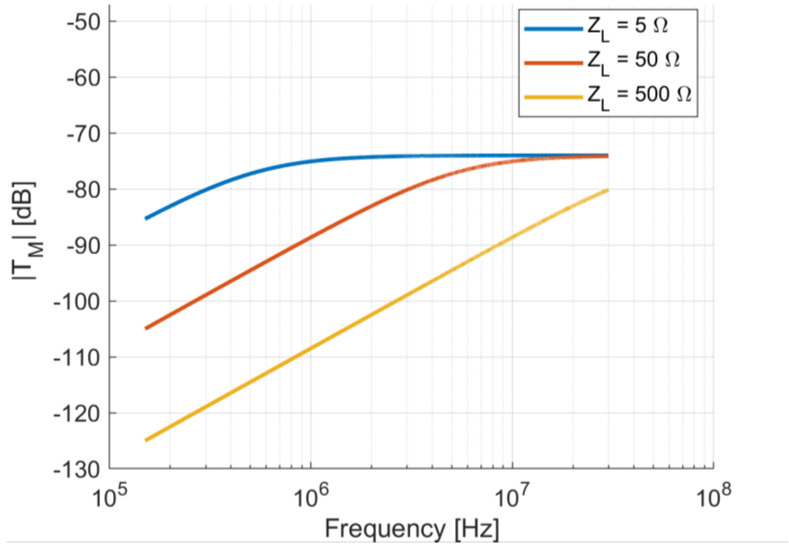

Figure 9.9: Transfer function for the induced voltage V_M and voltage V_S based on inductive coupling.

The figure shows that the transfer function is dependent on the load impedance. One can see that T_M of 5 Ω is larger by comparing the curves resulting from 50 Ω and 500 Ω load impedances. It is reasonable, as the inductive coupling is mainly determined by the current over the cable, which generates a magnetic field and couples to the antenna through mutual inductance M. The current through the 5 Ω load impedance is higher than the current through the 500 Ω load impedance. Here, it should be noted that the cable capacitance is neglected based on the assumption $Z_L \ll \frac{1}{j\omega C_{TL}}$ (see Figure 9.8). Therefore, the simplified model in Figure 9.8 is not proper for high load impedances.

E.2 Capacitive Coupling and Related Feedback Effect

a) Equivalent Circuit Model for Capacitive Coupling

Similar to inductive coupling, an equivalent circuit model in Figure 9.10 is used to illustrate capacitive coupling between the cable structure and the antenna. In the figure, the cable self-inductance L_{TL} is represented by two parts L_{TL1} and L_{TL2}, where $L_{TL1} = L_{TL2} = \frac{L_{TL}}{2}$. This makes sense, as the capacitive coupling is mainly based on cable voltage. For simplification, the cable self-capacitance C_{TL} is again neglected in the model by assuming $Z_L \ll \frac{1}{j\omega C_{TL}}$.

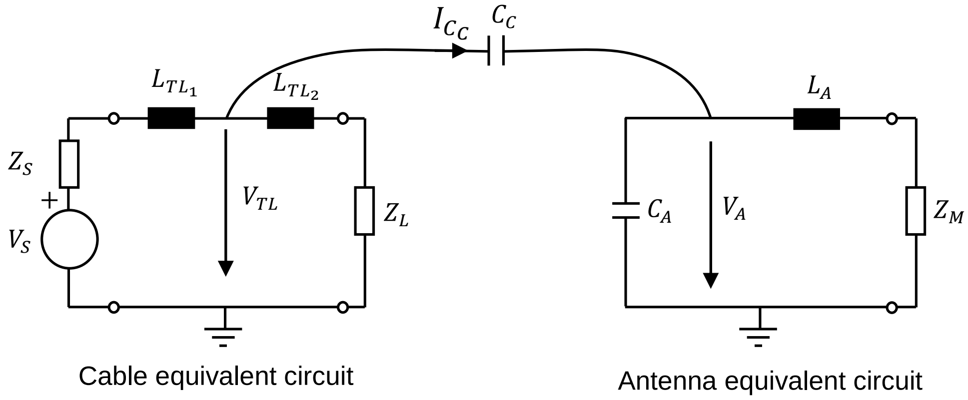

Figure 9.10: Equivalent circuit model for capacitive coupling between cable structure and antenna.

The cable voltage in the model is represented by V_{TL}. The capacitive coupling is illustrated by mutual capacitance C_C. The induced current I_{C_C} can be regarded as a displacement current between the cable and the rod antenna, which can be expressed as

$$I_{C_c} = j\omega C_C (V_{TL} - V_A). \tag{9.63}$$

The equation (9.63) can be decomposed into two following expressions:

$$I_A = j\omega C_C V_{TL}, \tag{9.64}$$

$$I_{FB} = -j\omega C_C V_A. \tag{9.65}$$

The expression (9.64) and (9.65) can be regarded as current sources impressing I_A in the antenna circuit and I_{FB} in the cable circuit respectively. I_{FB} is referred to as feedback current. The equivalent circuit can be remodeled by considering the current sources, as shown in Figure 9.11.

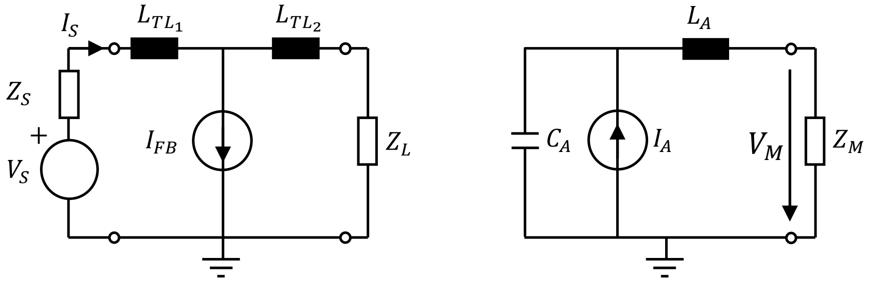

Cable equivalent circuit

Rod antenna equivalent circuit

Figure 9.11: Representation of induced current by the current source in the cable, and the antenna due to capacitive coupling caused by the voltage on the cable.

b) Feedback Effect due to Capacitive Coupling

The purpose of this section is to derive an expression that can be used to evaluate the significance of the feedback effect. Therefore, the antenna voltage V_A (see Figure 9.10) can be expressed in term of the current I_A, which results from the capacitive coupling, as

$$V_A = \frac{1}{j\omega C_A + \dfrac{1}{j\omega L_A + Z_M}} I_A. \tag{9.66}$$

Applying V_A of (9.66) to (9.65), the feedback current I_{FB} can be written as

$$I_{FB} = -\frac{j\omega C_C}{j\omega C_A + \dfrac{1}{j\omega L_A + Z_M}} I_A. \tag{9.67}$$

Inserting (9.64) to (9.67), I_{FB} can be expressed in term of the cable voltage V_{TL} as

$$I_{FB} = -\frac{\omega^2 C_C^2}{\underbrace{j\omega C_A + \dfrac{1}{j\omega L_A + Z_M}}_{1/Z_{FB_{C_C}}}} V_{TL}. \tag{9.68}$$

Here $Z_{FB_{C_C}}$ is defined as the impedance introduced by the feedback current I_{FB}. Using the model in Figure 9.11, the input impedance at the cable source can be expressed by

$$Z_{in} = j\omega L_{TL_1} + \frac{j\omega L_{TL_2} + Z_L}{1 + \dfrac{j\omega L_{TL_2} + Z_L}{Z_{FB_{C_C}}}}. \tag{9.69}$$

To evaluate $Z_{FB_{C_C}}$, typical antenna parameters and mutual capacitance of $C_C = 52\,\mathrm{fF}$ (described in chapter 4 section 4.4) are applied. The result is shown in Figure 9.12. One can observe that the impedance induced by capacitive coupling is very large, mainly in $\mathrm{M\Omega}$ range. For typical CISPR 25 setups, it satisfies: $Z_{FB_{C_C}} \gg j\omega L_{TL_2} + Z_L$. Therefore, the influence of feedback effect caused by capacitive coupling can be neglected.

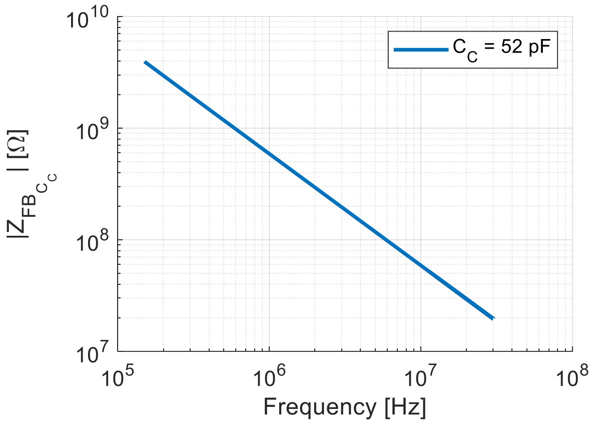

Figure 9.12: Additional impedance in the cable circuit due to the feedback effect of capacitive coupling.

c) Induced Voltage at Antenna due to Capacitive Coupling

By neglecting the feedback effect, the related coupling model in Figure 9.11 can be reduced to the model in Figure 9.13.

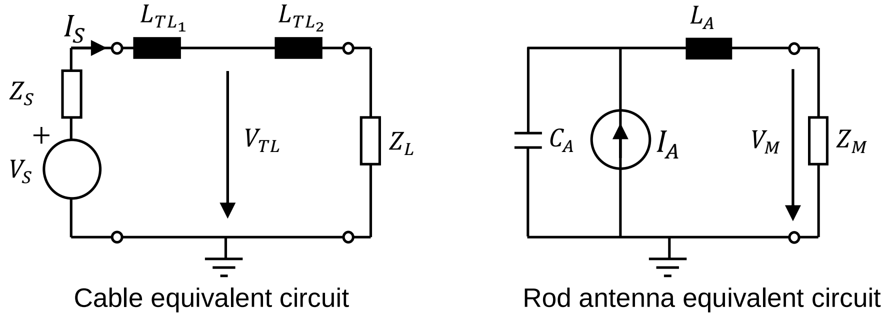

Cable equivalent circuit

Rod antenna equivalent circuit

Figure 9.13: Equivalent circuit model representing capacitive coupling between cable structure and rod antenna by neglecting feedback effect and cable self-capacitance C_{TL}.

The voltage V_M at the rod antenna load can be obtained by

$$V_M = \frac{Z_M}{j\omega L_A + Z_M} V_A. \tag{9.70}$$

Inserting the relation between the antenna voltage V_A and the induced current from capacitive coupling (9.66) in (9.71) leads to the expression

$$V_M = \frac{Z_M}{1 + j\omega C_A(j\omega L_A + Z_M)} I_A. \tag{9.71}$$

Now the V_M can be expressed in term of the cable voltage V_{TL} by inserting (9.64) into (3.36):

$$V_M = j\omega C_C \frac{Z_M}{1 + j\omega C_A(j\omega L_A + Z_M)} V_{TL}. \tag{9.72}$$

Finally, by applying the voltage divider rule in the cable equivalent circuit to calculate V_{TL} in dependence of the source voltage V_s and inserting into (9.72) the transfer function T_{C_C} between V_M and V_s can be expressed as

$$V_M = \underbrace{j\omega C_c \frac{Z_M}{1 + j\omega C_A(j\omega L_A + Z_M)} \frac{j\omega L_{TL_2} + Z_L}{Z_S + j\omega(L_{TL_1} + L_{TL_2}) + Z_L}}_{T_{C_C}} V_s. \tag{9.73}$$

T_{C_C} is defined as the transfer function based on capacitive coupling. In Figure 9.14, solid curves represent T_{C_C} for different load impedances. At the time, T_M for the same load impedances (already described in Figure 9.9) are again shown as dashed curves here for a direct comparison. It can be seen that the T_{C_C} is about 20 dB bigger than T_M, which means the capacitive coupling compared with the inductive coupling is dominant.

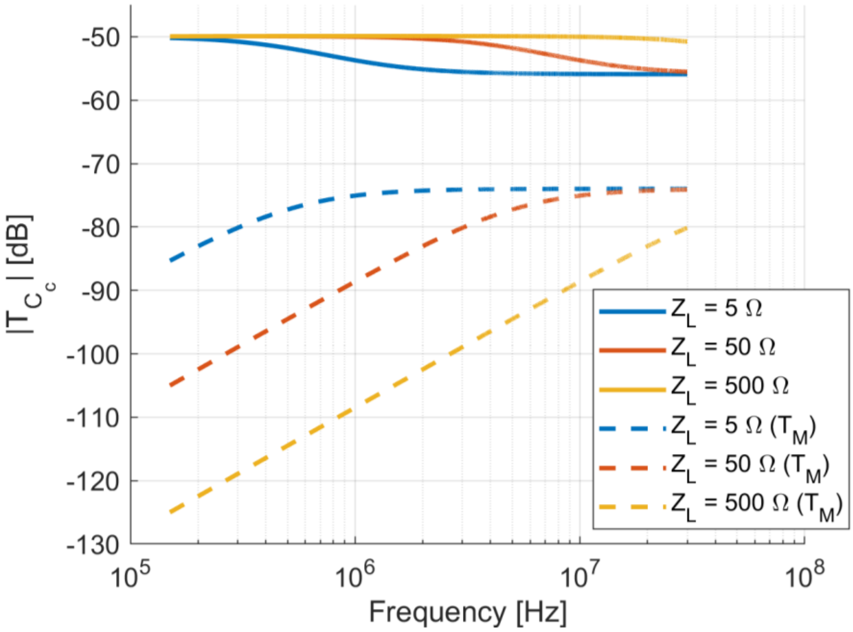

Figure 9.14: Transfer function for the induced voltage V_M and voltage V_S based on capacitive coupling.

F. Implementation of Huygens Principle in MATLAB

In this section, the kern code of the implementation of the field integral based on the Huygens principle are represented as two functions. The first function is to realize the electric field summation at an observation point P for all the electric and magnetic current sources over an opened plane, which is shown as follows:

```
% field computation from current sources on an opened plane
function [H_sum_xOy,E_sum_xOy,Ij,Im] = Opened_Huygens_field_XOY(freq,Bound-
ary_,E_field_s,H_field_s,Num_patches,normal_vector_n,F_Ori-
ent,Vertix_Patch_info,Vertix_info,Vertix_edge_center,P_ob)
%%
% find the center point of patch
Center_patch =zeros(Num_patches,3);
for m = 1:Num_patches
    Center_patch(m,:) = 0.25*(Vertix_info(Vertix_Patch_info(m,1),:)+...
                              Vertix_info(Vertix_Patch_info(m,2),:)+...
                              Vertix_info(Vertix_Patch_info(m,3),:)+...
                              Vertix_info(Vertix_Patch_info(m,4),:));
end

% vector 'b': the vector from the weightpoint to the edge center
b = zeros(Num_patches,4,3);
for m = 1:Num_patches
    for n=1:4
        b(m,n,:)= squeeze(Vertix_edge_center(m,n,:)).' - Center_patch(m,:);
    end
end

% vector 'c', reference current direction,
% normal_vector_n = [0,0,1]; % surface normal vector
c = zeros(Num_patches,4,3);
face_edge_v = zeros(Num_patches,4,3);
for m = 1:Num_patches
    m_patch = F_Orient(4*(m-1)+1:4*m,:); % grasp current face information
    for n=1:4
      face_edge_v(m,n,:) = Vertix_info(m_patch(n,2),:) -
Vertix_info(m_patch(n,1),:);
      c_temp = cross(squeeze(face_edge_v(m,n,:)).',normal_vec-
tor_n); %c_temp = vxn
      if(real(dot(c_temp,squeeze(b(m,n,:)).'))>0) %c.b>0
          c(m,n,:) = c_temp; % c_reference
      else
          c(m,n,:) = -c_temp;
      end
    end
end
%% Obtain edge current
 Ij = zeros(Num_patches,4); % electric current, from H_field -- |v.H|
 Im = zeros(Num_patches,4); % magnetic current, from E_field -- |v.E|

for m = 1:Num_patches
    for n = 1:4
        Ij_ini = dot(squeeze(face_edge_v(m,n,:)).',
squeeze(H_field_s(m,n,:)).'); % v.H
        if(real(Ij_ini)>0) %|v.H|
            Ij_ini = Ij_ini;
        else
            Ij_ini = -Ij_ini;
```

```
        end
        if( real(dot(squeeze(c(m,n,:)).', cross(normal_vec-
tor_n,squeeze(H_field_s(m,n,:)).')))>0 ) %c.(nxH)>0, current outside the
patch
            Ij(m,n) = Ij_ini;
        else
            Ij(m,n) = -Ij_ini;
        end

    end

end

for m = 1:Num_patches
    for n = 1:4
        Im_ini = dot(squeeze(face_edge_v(m,n,:)).',
squeeze(E_field_s(m,n,:)).');
        if(real(Im_ini)>0)  %|v.E|
            Im_ini = Im_ini;
        else
            Im_ini = -Im_ini;
        end
        if( real(dot(squeeze(c(m,n,:)).',
cross(squeeze(E_field_s(m,n,:)).',normal_vector_n)))>0 ) %c.(Exn)>0, cur-
rent outside the patch

            Im(m,n) = Im_ini;
        else
            Im(m,n) = -Im_ini;
        end

    end
end


% Boundary edges, no currents
B_size = size(Boundary_);
if (B_size(1)== 0) % no boundary edge
    Ij = Ij;
    Im = Im;
else
    for mm = 1:length(Boundary_(:,1))
        if (Boundary_(mm,3)== 0) % boundary edge, not connects to ground
           Ij(Boundary_(mm,1),Boundary_(mm,2))= 0;
           Im(Boundary_(mm,1),Boundary_(mm,2))= 0;
        else  % boundary edge, connects to ground
           Im(Boundary_(mm,1),Boundary_(mm,2))= 0;
        end
    end
end

%% parametric field integration
% Field Calculation
w = 2*pi*freq ;
u0 = 4*pi*10.^(-7);
e0 = 1/(36*pi)*10.^(-9);
k = w*sqrt(u0*e0);
% P = [1,1,5];%observation point
f_E = zeros(Num_patches,3 );
 for m = 1: Num_patches
     [vector_r,Js,Ms,WEI,divJs,divMs,Ngau,a_kesei,a_eta] = JsMs_computa-
tion(m,Vertix_info,Vertix_Patch_info,Im,Ij);
     % 9 point Gaussian integration
```

```
     for n = 1:9
          R = sqrt((P_ob(1)-vector_r(n,1)).^2+(P_ob(2)-vec-
tor_r(n,2)).^2+(P_ob(3)-vector_r(n,3)).^2);%Distance R between the observa-
tion point to the source current
          G = 1./(4*pi).*exp(-1i*k*R)./R;
          gradG = -[P_ob(1)-vector_r(n,1),P_ob(2)-vector_r(n,2),P_ob(3)-
vector_r(n,3)]./R*(1/R+1i*k)*G;
          S(n)  = norm(cross(a_eta(n,:),a_kesei(n,:)));
          part1_E(n,:) = -WEI(n)*1i*w*u0.*Js(n,:)*G*S(n);
          part2_E(n,:) = WEI(n)*cross(Ms(n,:),gradG)*S(n);
          part3_E(n,:) = WEI(n)*1./(1i*w*e0).*divJs(n)*gradG*S(n);   %from
jwp+divJs=0 current continuity equation
      end
      temp_1_E =  0.5*0.5*sum(part1_E);
      temp_2_E =  0.5*0.5*sum(part2_E);
      temp_3_E =  0.5*0.5*sum(part3_E);
      f_E(m,:) = temp_1_E + temp_2_E +temp_3_E ;
  end
  E_sum_xOy = sum(f_E);

%%%%%for H-field, each patch, 9 point gaussian integral%%%%%
f_H = zeros(Num_patches,3 );
 for m = 1: Num_patches
     [vector_r,Js,Ms,WEI,divJs,divMs,Ngau,a_kesei,a_eta] = JsMs_computa-
tion(m,Vertix_info,Vertix_Patch_info,Im,Ij);
     for n = 1:9
          R = sqrt((P_ob(1)-vector_r(n,1)).^2+(P_ob(2)-vec-
tor_r(n,2)).^2+(P_ob(3)-vector_r(n,3)).^2);
          G = 1./(4*pi).*exp(-1i*k*R)./R;
          gradG = -[P_ob(1)-vector_r(n,1),P_ob(2)-vector_r(n,2),P_ob(3)-
vector_r(n,3)]./R*(1/R+1i*k)*G;
          S(n)  = norm(cross(a_eta(n,:),a_kesei(n,:)));
          part1_H(n,:)  = WEI(n)*1i*w*e0.*Ms(n,:)*G*S(n);
          part2_H(n,:)  = -WEI(n)*cross(Js(n,:),gradG)*S(n);
          part3_H(n,:)  = WEI(n)*1./(1i*w*u0).*divMs(n)*gradG*S(n);   %from
jwp+divJs=0 current continuity equation
      end
      temp_1_H =  0.5*0.5*sum(part1_H); % sum of term 1 of all 9 points
      temp_2_H =  0.5*0.5*sum(part2_H); % sum of term 2 of all 9 points
      temp_3_H =  0.5*0.5*sum(part3_H); % sum of term 3 of all 9 points
      f_H(m,:) = temp_1_H + temp_2_H +temp_3_H ;% sum of all 3 terms for
each patch
  end
  H_sum_xOy = sum(f_H); % sum of all patches
```

The second function is to calculate the electric and magnetic current densities over the patches, which is shown as following, where the parametric structure and the local coordinate are described in [62].

```
function [vector_r,Js,Ms,WEI,divJs,divMs,Ngau,a_kesei,a_eta] = JsMs_compu-
tation(m,Vertix_info,Vertix_Patch_info,Im,Ij)


%parametic structure
[eta,kesei,WEI,Ngau] = GAUSSpoint(0,0,1,1,3);
for n=1:Ngau
    V1 = Vertix_info(Vertix_Patch_info(m,1),:);
    V2 = Vertix_info(Vertix_Patch_info(m,2),:);
```

```
    V3 = Vertix_info(Vertix_Patch_info(m,3),:);
    V4 = Vertix_info(Vertix_Patch_info(m,4),:);
    vector_r(n,:) = V1+(V2-V1)*eta(n)+(V4-V1)*kesei(n)+(V1-V2+V3-
V4)*eta(n)*kesei(n);%r'(eta,kesei)
    a_eta(n,:) = V2-V1+(V1-V2+V3-V4)*kesei(n);
    a_kesei(n,:) = V4-V1+(V1-V2+V3-V4)*eta(n);

    % Calculating Js
    Js(n,:) = 1/norm(cross(a_eta(n,:),a_kesei(n,:)))*(
    Ij(m,1)*eta(n)*a_eta(n,:)+...
    Ij(m,2)*kesei(n)*a_kesei(n,:)+...
    Ij(m,3)*(eta(n)-1)*a_eta(n,:)+...
    Ij(m,4)*(kesei(n)-1)*a_kesei(n,:));
    % Calculating Ms
    Ms(n,:) = 1/norm(cross(a_eta(n,:),a_kesei(n,:)))*(
    Im(m,1)*eta(n)*a_eta(n,:)+...
    Im(m,2)*kesei(n)*a_kesei(n,:)+...
    Im(m,3)*(eta(n)-1)*a_eta(n,:)+...
    Im(m,4)*(kesei(n)-1)*a_kesei(n,:));
    % Calculating the divergence of the charge density distribution
    divJs(n) =
1/norm(cross(a_eta(n,:),a_kesei(n,:)))*(Ij(m,1)+Ij(m,2)+Ij(m,3)+Ij(m,4));
    divMs(n) =
1/norm(cross(a_eta(n,:),a_kesei(n,:)))*(Im(m,1)+Im(m,2)+Im(m,3)+Im(m,4));
end
```

Reference

[1] S. Alexandersson, M. Alakula, “Automotive Power Electronic Future - from an EMC Perspective,” *Int. Symp. Power Electron. Elect. Drives Automat. and Motion*, pp. 609-613, May 2006.

[2] C. R. Paul, *Introduction to Electromagnetic Compatibility*. 2^{nd} ed., Hoboken, New Jersey, John Wiley & Sons, Inc., 2006.

[3] CISPR 12, “Vehicles, motorboats and spark-ignited engine driven devices - Radio disturbance characteristics – Limits and methods of measurement,” 2004.

[4] CISPR 25 Ed. 4.0, “Vehicles, boats and internal combustion engines - Radio disturbance characteristics – Limits and methods of measurements for the protection of on-board receivers,” 2015.

[5] TESEQ Advanced Test Solution for EMC, “Compact X-Wing BiLog Antenna 30 MHz to 2 GHz,” [Online]. Available: http://www.teseq.com/products/CBL-6141.php [Accessed Apr. 19, 2020].

[6] T. Burghart, H. Rossmanith, G. Schubert, “Evaluating the RF-Emissions of Automotive Cable Harness,” *Proc. IEEE Int. Symp. Electromagn. Compat.*, vol. 3, no. 3, pp. 787-791, Aug. 2004.

[7] R. Videnka, J. Svacina, “Introduction to EMC pre-compliance testing,” *17th Intern. Conf. Microwaves Radar and Wireless Commun.*, pp. 1-4, May 2008.

[8] J. Jia, D. Rinas, S. Frei, “Prediction the radiated emission of automotive sytems according to CISPR 25 using current scan methods,” *IEEE Trans. Electromagn. Compat.*, vol. PP, no. 99, pp. 1-10, Jan. 2016.

[9] J. Jia, D. Rinas, S. Frei, “Prediction of radiated fields from cable bundle based on current distribution measurement,” *Proc. IEEE Int. Symp. Electromagn. Compat.*, pp.1-7, Sept. 2012.

[10] D. Schneider, M. Beltle, B. Siegel, S. Tenbohlen, and W. Köhler, “Radiated emissions of an electric drive system estimated on a bench using disturbance currents and transfer functions,” *IEEE Trans. Electromagn. Compat.*, vol. 57, no. 3, pp. 311-321, Mar. 2015.

[11] S. F. Gregson, J. McCormick, C. G. Parini, *Principles of Planar Near-Field Antenna Measurements*. London, UK, The Institution of Engineering and Technology, 2007.

[12] K. W. Kark, *Antennen und Strahlungsfelder*. Wiesbaden, Vieweg+Teubner Verlag, 2004.

[13] C. Balanis, *Advanced Engineering Electromagnetics*. John Wiley&Sons, Inc., 2012.

[14] P. Tipler, G. Mosca, J. Wagner, *Physik für Wissenschaftler und Ingenieure*, 7. Deutsche Auflage, Springer-Verlag Berlin Heidelberg, 2015.

[15] S. Frei, “Bestimmung der bordnetzgebundenen Störaussendung mit dem kapazitiven Spannungssensor,” *EMV Düsseldorf*, 2005.

[16] S. Frei, T. Nägel, R. Jobava, “Bestimmung der Störaussendung im KFZ durch die getrennte Betrachtung der elektrischen und magnetischen Verkopplungen,” *EMV Düsseldorf*, 2004.

[17] D. Hockanson, J. Drewniak, T. Hubing, T. Van Doren, F. Sha, M. Wilhelm, “Investigation of fundamental EMI source mechanisms driving common-mode radiation from printed circuit boards with attached cables,” *IEEE Trans. Electromagn. Compat.*, vol. 38, pp. 557-566, Jun. 1996.

[18] C. R. Paul, “A comparison of the contributions of common-mode and differential-mode currents in radiated emissions,” *IEEE Trans. Electromagn. Compat.*, vol. 31, no. 2, pp. 189-193, May 1989.

[19] J. Jia, D. Rinas, S. Frei, “An alternative method for measurement of radiated emissions according to CISPR 25,” *Proc. IEEE Int. Symp. Electromagn. Compat.*, pp. 304-309, Sept. 2013.

[20] J. Jia, F. Kremer, S. Frei, “Modellierung von CISPR 25 Antennenmessung mittels schneller approximierender Berechnungsverfahren,” *EMV Düsseldorf*, pp. 255-262, Feb. 2012.

[21] J. Jia, “Current Scan Methods to Predict Radiated Emissions of Automotive Components According to CISPR 25,” Ph. D. dissertation, On-board system lab, TU Dortmund, Dortmund, Germany, 2015.

[22] W. Smith, R. Frazier, “Prediction of anechoic chamber radiated emissions measurements through use of empirically-derived transfer functions and laboratory common-mode current measurements,” *Proc. IEEE Int. Symp. Electromagn. Compat.*, vol. 1, pp. 387-392, 1998.

[23] D. Schneider, S. Tenbohlen, W. Köhler, “Pre-compliance test method for radiated emissions of automotive components using scattering parameter transfer functions,” *Proc. IEEE Int. Symp. Electromagn. Compat.*, pp.1-6, Sept. 2012.

[24] D. Schneider, M. Bottcher, B. Schoch, S. Hurst, “Transfer functions and current distribution algorithm for the calculation of radiated emissions of automotive components,” *Proc. IEEE Int. Symp. Electromagn. Compat.*, pp. 443-448, Sept. 2013.

[25] D. Schneider, “Abschätzung gestrahlter Emissionen im Kfz-Komponententest bei entwicklungsbegleitenden Prüfungen,” Ph. D. dissertation, Institut für Energieübertragung und Hochspannungstechnik, Universität Stuttgart, Stuttgart, Germany, 2016.

[26] C. R. Paul, *Analysis of Multiconductor Transmission Lines*. John Wiley & Sons, Inc., 2008.

[27] C. R. Paul and S. Nasar, *Introduction to Electromagnetic Fields*. 2nd ed., New York, USA, McGraw-Hill, 1987.

[28] Z. Chen, J. Jia, S. Frei, S. Huq, D. Pommerenke, “Minimal detectable signal during current measurement in a CISPR 25 set-up,” *Int. Symp. Electromagn. Compat. (APEMC)*, vol. 1, pp. 845-848, 2016.

[29] FCC, “F-65 Current Monitor Probe,” [Online]. Available: https://www.fischercc.com/products/f-65/ [Accessed Apr. 19, 2020].

[30] V. Volski, “Efficient physical optics approximation for the calculation of radiation pattern of planar antennas located on a finite ground plane,” *IEEE Trans. Electromagn. Compat.*, vol. 53, no. 1, pp. 460-465, 2005.

[31] D. Rinas, J. Jia, A. Zeichner, S. Frei, “Substituting EMC emission measurement by field and cable scan method using measured transfer function,” *Adv. Radio Sci.*, vol. 11, pp. 183-188, 2013.

[32] X. Tong, D. W. P. Thomas, A. Nothofer, P. Sewell, C. Christopoulos, “Modeling electromagnetic emissions from printed circuit boards in closed environments using equivalent dipoles,” *IEEE Trans. Electromagn. Compat.*, vol. 52, pp. 462-470, May 2010.

[33] A. Taaghol, T. K. Sarkar, “Near-field to near/far-field transformation for arbitrary near-field geometry, utilizing an equivalent magnetic current,” *IEEE Trans. Electromagn. Compat.*, vol. 38, no. 3, pp. 536-542, Aug. 1996.

[34] T. K. Sarkar, A. Taaghol, “Near-field to near/far-field transformation for arbitrary near-field geometry utilizing an equivalent electric current and MoM,” *IEEE Trans. Electromagn. Compat.*, vol. 47, no. 3, pp. 566-573, Mar. 1999.

[35] J. Pan, G. Xu, Y. Zhang, F. Jun, “Far-field radiation estimation from near-field measurements and image theory,” *Proc. IEEE Int. Symp. Electromagn. Compat.*, pp. 609-614, 2014.

[36] J. Pan, G. Xu, F. Jun, “Far-field prediction by only magnetic near fields on a simplified Huygens’ surface,” *IEEE Trans. Electromagn. Compat.*, vol. 57, no. 4, pp. 693-701, 2015.

[37] R. D. Cook, D. S. Malkus, M. E. Plesha, *Concepts and Applications of Finite Element Analysis*. 3rd ed., John Wiley & Sons, Inc., 1989.

[38] A. Radchenko, V. Khilkevich, N. Bondarenko, D. Pommerenke, M. Gonser, J. Hansen, C. Keller, “Transfer function method for predicting the emissions in a CISPR 25 test-setup,” *IEEE Trans. Electromagn. Compat.*, vol. 56, no. 4, pp. 894-902, Aug. 2014.

[39] V. S. Reddy, P. Kralicek, J. Hansen, “A novel segmentation approach for modeling of radiated emission and immunity test setups,” *IEEE Trans. Electromagn. Compat.*, vol. 59, no. 6, pp. 1781-1790, Dec. 2017.

[40] C. Carobbi, “A lumped model of the rod antenna measurement setup for automotive and military testing,” *Int. Symp. Electromagn. Compat. (APEMC)*, pp. 57-62, 2018.

[41] H. Hackl, “On the simulation of radiated emission of integrated circuits according the CISPR 25 ALSE test,” Ph. D. dissertation, Technischen Universität Graz, Styria, Austria, 2019.

[42] F. Tesche, M. Ianoz, T. Karlsson, *EMC Analysis Methods and Computational Models*. New York, USA, Wiley-Interscience, 1997.

[43] H. Hackl, G. Winkler, B. Deutschmann, “Simulation of radiated emission during the design phase based on scattering parameter measurement,” *10th Int. Workshop Electromagn. Compat. Integr. Circuits*, pp. 228-231, Nov. 2015.

[44] B. Harlacher, R. Stewart, “CISPR 22 conducted common mode voltage measurements along a wire using a capacitive voltage probe,” *Proc. IEEE Int. Symp. Electromagn. Compat.*, vol. 1, pp. 1-5, 2002.

[45] H. Hackl, B. Auinger, “Calculation of very near field radiated emission of a straight cable harness,” 1*2th Conf. Ph.D. Res. Microelectron. and Electron. (PRIME)*, pp. 1-4, 2016.

[46] J. D. Kraus, *Electromagnetics*. New York, USA, McGraw-Hill, 1941.

[47] R. Harrington, *Time-Harmonic Electromagnetic Fields*. New York, USA, McGraw-Hill, 1961.

[48] J. Stratton, *Electromagnetic Theory*. New York and London, McGraw-Hill, 1941.

[49] A. E. H. Love, "The integration of the equations of propagation of electric waves," *Philos. Trans. Soc.*, vol. 197, pp. 1-45, 1901.

[50] S. A. Schelkunoff, "Some equivalence theorems of electromagnetics and their application to radiation problems," *The Bell Syst. Tech. J.*, vol. 15, pp. 92-112, 1936.

[51] C. Balanis, *Antenna Theory: Analysis and Design*. 3rd ed., John Wiley & Sons, Inc., 2005.

[52] A. Schroth, V. Stein, *Moderne numerische Verfahren zur Lösung von Antennen- und Streuproblemen*. Oldenburg Wissenschaftsverlag, 1985.

[53] H. Brüns, "Pluserregte Elektromagnetische Vorgänge in Dreidimensionalen Stabstrukturen," Ph. D. dissertation, Universität der Bundeswehr Hamburg, Hamburg, Germany, 1985.

[54] S. M. Rao, "Electromagnetic scattering and radiation of arbitrary-shaped surfaces by triangular patch modeling," Ph. D. dissertation, University of Mississippi, 1980.

[55] R. F. Harrington, *Field Computation by Moment Methods*. New York, USA, IEEE Press, 1993.

[56] R.F. Harrington, "Matrix methods for field problems," *Proc. IEEE*, vol. 55, no. 2, pp. 136-149, 1967.

[57] W. C. Gibson, *The Method of Moments in electromagnetics*. CRC Press, Taylor Francis Group, 2015.

[58] A. W. Glisson, "On the development of numerical techniques for treating arbitrary-shaped surface," Ph. D. dissertation, University of Mississippi, July 1978.

[59] A. W. Glisson, D. R. Wilton, "Simple and efficient numerical methods for problems of electromagnetic radiation and scattering from surfaces," *IEEE Trans. Antennas Propag.*, vol. AP-28, no. 5, Sept. 1980.

[60] M. Sørensen, O. Franek, G. F. Pedersen, A. Radchenko, K. Kam, D. Pommerenke, "Estimate on the uncertainty of predicting radiated emission from near-field scan caused by insufficient or inaccurate near-field data: Evaluation of the needed step size phase accuracy and the need for all surfaces in the Huygens' box," *Proc. IEEE Int. Symp. Electromagn. Compat.*, pp. 1-6, 2012.

[61] D. Leugner, "Berechnung der elektromagnetischen Einkopplung durch Aperturen mit analytische Verfahren und der Momenten-methode," Ph. D. dissertation, TU Hamburg-Harburg, Hamburg, Germany, 2004.

[62] T. Mader, "Berechnung elektromagnetischer Felderscheinungen in abschnittsweise homogenen Medien mit Oberflächenstromsimulation," Ph. D. dissertation, TU Hamburg-Harburg, Hamburg, Germany, 1992.

[63] K. Gonschorek, "Die Berechnung des elektromagnetischen Impulsverhaltens dreidimensionaler Anordnungen schlanker Elektroden," Ph. D. dissertation, Hochschule der Bundeswehr Hamburg, Hamburg, Germany, 1980.

[64] G. Ergaver and J. Trontelj, “Prediction of radiated emissions of automotive electronics early in the design phase based on automotive component level testing,” *J. Microelectron., Electron. Components and Materials*, vol. 46, no. 1, pp. 42-52, 2016.

[65] CST Studio Suite, “Software zur Simulation elektromagnetischer Felder,” [Online]. Available: https://www.3ds.com/de/produkte-und-services/simulia/produkte/cst-studio-suite/ [Accessed Apr. 19, 2020].

[66] Altair FEKO, “Altair Feko™ is a comprehensive computational electromagnetics (CEM) code used widely in the telecommunications, automobile, space and defense industries,” [Online]. Available: https://altairhyperworks.com/product/FEKO [Accessed Apr. 19, 2020].

[67] CONCEPT-II, “Features,” [Online]. Available: http://www.tet.tuhh.de/concept/features/ [Accessed Apr. 19, 2020].

[68] FastFieldSolvers, “FastHenry2,” [Online]. Available: https://www.fastfieldsolvers.com/fasthenry2.htm [Accessed Apr. 19, 2020].

[69] K. Nabors, J. White, “Fastcap: a multipole accelerated 3-D capacitance extraction program,” *IEEE Trans. Comput.-Aided Des.*, vol.10, no.11, pp. 1447-1459, Nov. 1991.

[70] H. Brüns, A. Vogt, M. Magdowski, M. Robinson, F. Heidler, C. Schuster, “Modeling challenging EMC problems,” *IEEE Electromagn. Compat. Mag.*, vol. 6, pp. 45-53, 2017.

[71] R. J. Spiegel, C. A. Booth, E. L. Bronaugh, “A radiation measuring system with potential automotive under-hood application, *IEEE Trans. Electromagn. Compat.*, vol. EMC-25, pp. 61-69, 1983.

[72] Schwarzbeck Mess-Elektronik, “Rauscharme aktive vertikale Monopol-Antenne VAMP 9243,” datasheet, [Online]. Available: http://www.reliantemc.com/download/Schwarzbeck/Schwarzbeck-Active-Monopole-Antenna-VAMP-9243-Data-Sheet.pdf [Accessed Apr. 19, 2020].

[73] CISPR 16-1-4, “Radio disturbance and immunity measuring apparatus – Ancillary equipment – Radiated disturbances,” 2008.

[74] J. Gerd, Kurze Antennen, Entwurf u. Berechnung verkürzter Sende- und Empfangsantennen. Kosmos Verlags-GmbH, 1989.

[75] A. Neugut, “Ultra short multiband AM/FM/DAB active antennas for automotive application,” Ph. D. dissertation, Universität der Bundeswehr München, Münschen, Germany, Nov. 2011.

[76] U. Hilger, “EMV Störfestigkeitssimulationen an ausgedehnten Kfz Bussystemen,” Ph. D. dissertation, TU Dortmund, Dortmund, Germany, 2014.

[77] G. Monien, “Die Beeinflussung der Meßabweichung von Feldsonden und Stromzangen durch reale Umgebungsbedingungen,” Ph. D. dissertation, Technische Universität Hamburg, Hamburg, Germany, 2003.

[78] M. Spang, “Einsatz von Feldsonden mit mehreren Ausgängen in EMV-Nahfeldmessungen von Leiterplatten,” Ph. D. dissertation, Friedrich-Alexander-Universität Erlangen-Nürnberg, Erlangen, Germany, 2012.

[79] R. Jobava, D. Karkashadze, S. Frei, A. Gheonjian, E. Yavolovskaia, A. Grachev, “Equivalent circuit approach in solution of low frequency automotive EMC problems,” *DIPED Processing*, 2003.

[80] C. Fanning, “Improving monopole radiated emission measurement accuracy; RF chamber influences, antenna height and counterpoise grounding (CISPR 25 & MIL-STD-461E vs MIL-STD-461F),’’ *Proc. IEEE Int. Symp. Electromagn. Compat.*, pp. 103-118, 2009.

[81] D. Warkentin, A. Wang, W. Crunkhorn, “Shielded enclosure accuracy improvements for MIL-STD-461E radiated emissions measurements,” *Proc. IEEE Int. Symp. Electromagn. Compat.*, pp. 404-409, 2005.

[82] D. Swanson, “Analysis of MIL-STD-461E and MIL-STD-461F RE102 test setup configurations below 100 MHz,” *Proc. IEEE Int. Symp. Electromagn. Compat.*, pp. 1-11, 2008.

[83] L. Turnbull, “The ground plane resonance-problems with radiated emissions measurements below 30 MHz,” *16th Automot. EMC Conf. 2007*, pp. 1-13, Oct. 2007.

[84] D. Pozar, *Microwave Engineering*. 4th ed., New York, Wiley, 2012.

[85] I. Oganezova, R. Kado, B. Khvitia, A. Gheonjian, R. Jobava, “Simulation of conductive and radiated emissions from a wiper motor according to CISPR 25 standard,” *Proc. IEEE Int. Symp. Electromagn. Compat.*, pp. 963-968, 2015.

[86] P. Kay, “EMC test site validations for 1m Automotive and military emissions tests,” *EMC Symp. - Perth (EMCSA)*, 2011.

[87] Keysight Technologies, “E5071B ENA RF Network Analyzer, 300 kHz to 8.5 GHz,” [Online]. Available: https://www.keysight.com/en/pd-1000004587:epsg:pro/ena-rf-network-analyzer [Accessed Apr. 19, 2020].

[88] MathWorks, “Normally distributed random numbers,” [Online]. Available: https://de.mathworks.com/help/matlab/ref/randn.html [Accessed Apr. 19, 2020].

[89] Z. Chen, D. Rinas, S. Frei, “Vorhersage von CISPR 25 Antennenmessergebnissen unter 30 MHz auf Basis von Nahfeldmessdaten,” Elektromagnetische Verträglichkeit, Messe Düsseldorf, 2015.

[90] Z. Chen, S. Frei, “A near-field measurement based method for predicting field emissions below 30 MHz in a CISPR 25 test,” *Adv. Radio Sci.*, pp. 147-154, 2016.

[91] Z. Chen, S. Frei, “Near-field measurement based prediction of antenna test results below 30 MHz in CISPR 25 Setups,” *Proc. IEEE Int. Symp. Electromagn. Compat.*, pp. 17-22, Sept. 2016.

[92] C. d. Boor, *A practical guide to splines*. Springer-Verlag New York, 1978.

[93] M. Sorensen, O. Franek, G. Pedersen, A. Radchenko, K. Kam and D. Pommerenke, “Estimate on the uncertainty of predicting radiated emission from near-field scan caused by insufficient or inaccurate nearfield data: Evaluation of the needed step size, phase accuracy and the need for all surfaces in the huygens' box,” *Proc. IEEE Int. Symp. Electromagn. Compat.*, pp. 1-6, 2012.

[94] K. Gonschorek, R. Vick, *Electromagnetic compatibility for device design and system integration*. Springer-Verlag Berlin Heidelberg, 2009.

[95] Z. Li, “Electromagnetic Sensors for Measurements on Electric Power Transmission Lines,” Ph. D. dissertation, Washington States University, Washington, USA, Aug. 2011.

[96] M. Kanda, “Standard probes for electromagnetic field measurements,” *IEEE Trans. Antennas Propag.*, vol. 41, no. 10, Oct. 1993.

[97] Rohde & Schwarz, “R&S EZ-12 Antenna Impedance Converter,” [Online]. Available: https://www.rohde-schwarz.com/de/produkt/ez-12-produkt-startseite_63493-9796.html [Accessed Apr. 19, 2020].

[98] J. Karst, C. Groh, H. Garbe, “Calculable field generation using TEM cells applied to the calibration of a novel E-field probe,” *IEEE Trans. Electromagn. Compat.*, vol. 44, no. 1, pp. 59-71, 2002.

[99] Z. Ji, K. Kam, J. Min, V. Khilkevich, D. Pommerenke, F. Jun, “An effective method of probe calibration in phase-resolved near-field scanning for EMI application,” *IEEE Trans. Instrum. Meas.*, vol. 62, no. 3, pp. 648-658, 2013.

[100] Rohde & Schwarz, “R&S ESPI Test Receiver,” [Online]. Available: https://www.rohde-schwarz.com/de/produkt/espi-produkt-startseite_63493-8645.html [Accessed Apr. 19, 2020].

[101] M. N. O. Sadiku, *Numerical techniques in electromagnetics*. 2nd ed., New York, CRC press LLC, 2001.

List of own Publications

S. Marathe, Z. Chen, K. Ghosh, H. Kajbaf, S. Frei, M. Sorensen, D. Pommerenke, J. Min: **Spectrum analyzer-based phase measurement for near-field EMI scanning**, *IEEE Trans. Electromagn. Compat., 2019.*

Chen, Z.; Zeichner, A.; Frei, S.: **Grenzen des Stromscan basierten Dipolmodells und Erweiterung mit einem quasistatischen Ansatz**, *EMV Düsseldorf, Germany, 2018.*

Zeichner, A.; Chen, Z.; Frei, S.: **Theoretical maximum data rate estimations for PLC in automotive power distribution systems**, *EMC Europe, Angers, France, 2017.*

Chen, Z.; Frei, S.: ***Near-Field Measurement Based Prediction of Antenna Test Results Below 30 MHz in CISPR 25 Setups****, EMC Europe, Wroclaw, Poland, 2016.*

Chen, Z.; Huq, S.; Jia, J.; Frei, S.; Pommerenke, D.: **Minimal Detectable Signal during Current Measurement in a CISPR 25 Set-Up**, *APEMC, China, Shengzhen, 2016.*

Chen, Z.; Frei, S.: ***A near-field measurement based method for predicting field emissions below 30 MHz in a CISPR 25 test set-up****, Adv. Radio Sci., 14, pp.147-154. Sept. 2016.*

Chen, Z.; Rinas. D.; Frei, S.: **Vorhersage von CISPR 25 Antennenmessergebnissen unter 30 MHz auf Basis von Nahfeldmessdaten**, *EMV Düsseldorf, Germany, 2016.*

Chen, Z.; Marathe, S.; Kajbaf, H.; Frei, S.; Pommerenke, D.: **Broadband Phase Resolving Spectrum Analyzer Measurement for EMI Scanning Applications,** *EMC Europe, Dresden, 2015.*

Chen, Z.; Rinas, D.; Frei, S.: **Determination of Radiation Models Based on Measured Electromagnetic Field Distribution**, *ASIM Tagung, Stralsund, 2015.*

Eidesstattliche Versicherung

Ich versichere hiermit an Eides statt, dass ich die vorliegende Dissertation mit dem Titel „Low Frequency Field Prediction Applied to CISPR 25 Test Setups“ selbstständig und ohne unzulässige fremde Hilfe angefertigt habe. Ich habe keine anderen als die angegebenen Quellen und Hilfsmittel benutzt sowie wörtliche und sinngemäße Zitate kenntlich gemacht.

Die Arbeit hat in gegenwärtiger oder in einer anderen Fassung weder der TU Dortmund noch einer anderen Hochschule im Zusammenhang mit einer staatlichen oder akademischen Prüfung vorgelegen.

Dortmund, 22.03.2020

Zongyi Chen